

Experimental investigation of an oscillating compressor cascade in the case of aerodynamic mistuning

vorgelegt von
Leonie Malzacher (M.Sc.)

an der Fakultät V - Verkehrs- und Maschinensysteme
der Technischen Universität Berlin
zur Erlangung des akademischen Grades

Doktorin der Ingenieurwissenschaften
- Dr.-Ing. -

genehmigte Dissertation

Promotionsausschuss

Vorsitzender: Prof. Dr. Bardenhagen

Gutachter: Prof. Dr. Peitsch

Gutachter: Prof. Quaranta (Ph.D.)

Tag der wissenschaftlichen Aussprache: 26. November 2020

Berlin 2021

Acknowledgments

I would like to express my gratefulness to my supervisor Professor Peitsch, Chair for Aero Engines at the Technische Universität Berlin, for his guidance, support, and trust throughout the path towards this dissertation, as well as for sharing his genuine enthusiasm for turbomachines with me.

I would like to thank Professor Quaranta, who kindly reviewed this work, and Professor Bardenhagen, chairman of the examination committee.

Likewise, I would like to thank Dr. Hennings, from the German Aerospace Center (DLR) in Göttingen, for his valuable input and feedback from day one.

I would like to thank the members of the aeroelastic team for sharing their passion for aeroelasticity with me, along with the fruitful discussions that created a stimulating environment. Special thanks go to Valentina, Patrick, and Victor for the coconut sessions, reviews, discussions, and teamwork in many different projects - a true source of joy, inspiration, and motivation. Also thanks to Jan for being always available for discussions about measurement techniques and fluid mechanics and for turning our office into a small art gallery. It was indeed great fun to enjoy scenic beaches and landscapes even when the winter in Berlin was in full swing outside. I would like to thank Astrid for supporting me with the administrative processes, the nice morning coffee breaks, and encouraging and kind words. Thanks also to my colleagues at TU Berlin for creating a nice work environment, their support, helpful discussions, and just a good fun time.

Moreover, the installation of the test facility would have not been possible without such excellent technical support. I would like to thank Norbert, Horst, and Christian, as well as the team from the machine shop in our department.

I am thankful to InnoEnergy for taking me on board with the PhD-school and supporting my stay at the Massachusetts Institute of Technology (MIT) in the USA.

Special thanks go to my family and friends for their unconditional love and support. Especially to my sister for her boundless positivity from the very beginning, and for reminding me that everything is easier with a smile when facing challenging days at the test rig. I would also like to thank Carina and Nathalie for their friendship, who are by my side since day one when we started our engineering journey, for their support, and for sharing the excitement about technology, innovation, and materials science. To Christoph for sharing his enthusiasm for measuring techniques with me, his motivating thoughts, and his perpetual belief in my work, which over the years pushed me to improve as a researcher. Lastly, I would like to thank Kathi and Nadja for their true friendships over decades, their positive spirit, encouragement to pursue this work, and the nice memories about small and big adventures we experienced together.

Summary

An experimental investigation has been carried out at an oscillating compressor cascade at the chair for Aero Engines of the Technische Universität Berlin in Germany. The investigation focuses on the effect of aerodynamic mistuning on aeroelastic stability in a compressor cascade. Aerodynamic mistuning can occur due to manufacturing errors, blade mounting or repair and alters geometrical parameters of the flow passage. It influences the blade surface pressure distribution and can degrade the aeroelastic response of the system.

In order to investigate the flutter behavior in the case of aerodynamic mistuning, the aerodynamic response of a mistuned oscillating compressor cascade has been studied. In the measurement section of the test facility, the blades are forced to oscillate sinusoidally in a pitching mode for a wide range of interblade phase angles at different reduced frequencies. The aerodynamic mistuning is introduced by a blade stagger-to-stagger angle variation. Four different mistuning patterns are investigated: one-blade mis-staggering, alternating mis-staggering, random mis-staggering and cases in which all blades in the cascade feature a constant stagger angle alteration.

The test facility is equipped with steady and unsteady measurement devices. Firstly, the base flow characteristic is presented for different Mach and Reynolds numbers. The aerodynamic response is acquired by means of unsteady blade surface pressure and strain gauge measurements. The results suggest that aerodynamic mistuning stabilizes or destabilizes the system depending on the nature of the mistuning pattern. For a positive change in stagger angle for the one-blade and alternating pattern, the damping characteristic is maintained for the system. That is, the same unstable interblade phase angle remains unstable compared to the baseline case. For the negative stagger angle variations, the aerodynamic damping turns negative for one interblade phase angle, indicating instability compared to the baseline case. For large negative stagger angle variations of all blades of the cascade, the amplitude of the damping curve is especially affected and dictates the severity of these stability regions.

In the past, most of the mistuning research was dedicated to structural blade-to-blade alteration e.g. changes in mass, stiffness and damping, influencing the eigenfrequencies. Thus, the present work contributes to extend the physical understanding of aerodynamic mistuning in a traveling wave test setup and characterizes the underlying mechanisms.

Zusammenfassung

In der vorliegenden Arbeit wurde die Auswirkung von aerodynamischer Verstimmung auf die aeroelastische Stabilität eines Verdichtergitters untersucht. Die experimentellen Untersuchungen wurden an einem schwingenden Gitter am Fachgebiet Luftfahrtantriebe der Technischen Universität Berlin in Deutschland durchgeführt.

Um die Veränderung der aeroelastischen Stabilität aufgrund der Verstimmung zu untersuchen, wurde die aerodynamische Antwort des schwingenden Gitters gemessen. Die Schaufeln können in der Messstrecke zwangsbezwegt werden, verschiedene Phasendifferenzwinkel und reduzierte Frequenzen können untersucht werden. Die Verstimmung wurde mit einer Änderung des Staffelungswinkels realisiert. Vier verschiedene Verstimmungsmuster wurden untersucht, das erste ist eine Verstimmung der mittleren Schaufel der Kaskade, das zweite ein alternierendes Muster, das dritte ein zufälliges und das letzte Muster untersucht verschiedene Testfälle, in denen der Staffelungswinkel von allen Schaufeln manipuliert wurde.

Zuerst wurde die Basisströmung für verschiedene Mach- und Reynoldszahlen untersucht. Die aerodynamische Antwort des schwingenden Gitters wurde mit instationären Drucksensoren und Dehnmessstreifen gemessen. Die Ergebnisse zeigen, dass die Verstimmung stabilisierend oder destabilisierend auf das System wirken kann, abhängig vom Verstimmungsmuster. Für das erste und zweite Muster in Kombination mit einer positiven Änderung des Staffelungswinkels zeigt das System eine ähnliche Dämpfungscharakteristik im Vergleich zum Referenzfall d.h. das Vorzeichen der Dämpfung bleibt für die untersuchten Phasendifferenzwinkel erhalten. Eine negative Änderung des Staffelungswinkels für die gleichen Testfälle zeigt, dass das Vorzeichen der Dämpfung für einen untersuchten Phasendifferenzwinkel von einem stabilen zu einem instabilen Zustand wechselt. Der dritte Testfall zeigt kaum eine Auswirkung auf die aeroelastische Stabilität des Systems. Für große negative Änderungen des Staffelungswinkels von allen Schaufeln im Gitter, ändert sich die Amplitude der Dämpfungskurve und bestimmt die Schwere dieser Stabilitätsbereiche.

In der Vergangenheit konzentrierten sich die Forschungsvorhaben im Bereich Verstimmung auf die Manipulation von Masse, Steifigkeit und Dämpfung; Parameter, die die Eigenfrequenzen der Schaufeln ändern. Die vorliegende Arbeit soll zu einer Erweiterung des physikalischen Verständnisses einer aerodynamisch verstimmtten Kaskade beitragen, charakterisiert die zugrundeliegenden Mechanismen und gibt einen Ausblick, wie die Ergebnisse in Verdichterentwürfen berücksichtigt werden können.

Contents

Nomenclature	XIII
1 Aeroelasticity in Turbomachines	1
1.1 Introduction	1
1.2 Flutter	4
1.3 Thesis Motivation	5
2 State of the Art	7
2.1 Fundamental Concepts in Aeroelasticity	7
2.1.1 Aeroelastic Modeling	7
2.1.2 Aerodynamic Damping Parameter	8
2.1.3 Reduced Frequency	10
2.2 Flutter Testing Methods	11
2.3 Review of Oscillating Cascade Experiments	13
3 Objectives and Approach	20
4 Test Facility and Measurement Technique	22
4.1 Wind Tunnel for Aeroelastic Investigation	23
4.2 Oscillating Compressor Cascade	24
4.3 Measurement Setup	29
4.3.1 Surface Oil Flow Visualization Technique	29
4.3.2 Hot-wire Anemometry	30
4.3.3 Strain Gauges	31
4.3.4 Blade Surface Pressure Measurements	33
4.3.5 Data Acquisition	35
5 Data Reduction Procedure	39
5.1 Statistical Parameters	39
5.2 Aerodynamic Coefficients	40
5.3 Aerodynamic Damping Parameter	42

6	Experimental Investigation	43
6.1	Testing Strategy	43
6.2	Base Flow	45
6.3	Unsteady Performance and Stability Assessment	53
6.4	Aerodynamic Mistuning	64
6.4.1	Cluster I - Aerodynamic Response and Stability Assess- ment (one, alternating, random pattern)	64
6.4.2	Cluster II - Aerodynamic Response and Stability As- sessment (homogeneous pattern)	78
6.4.3	Comparison of one-blade, alternating, random and ho- mogeneous pattern	88
7	Summary and Conclusion	91
	Bibliography	94
	List of Figures	104
	List of Tables	109
A	Frequency plots	A-1
B	Measurement Uncertainty	B-1
B.1	Methodology	B-1
B.2	Total Uncertainty	B-1
B.3	Accuracy of Signal Conditioning and A/D-Conversion	B-3
B.4	Prandtl Tube	B-4
B.5	Hot Wire Anemometry	B-6
B.5.1	Calibration	B-6
B.5.2	Curve Fitting	B-6
B.5.3	Ambient Temperature	B-7
B.5.4	Ambient Pressure and Humidity	B-7
B.5.5	Anemometer Accuracy and Signal Conversion	B-8
B.5.6	Combined Accuracy	B-8
B.6	Strain Gauge	B-9
B.6.1	Calibration - Plunging mode	B-9
B.6.2	Pitching Mode	B-11
B.6.3	Strain Gauge - other influences	B-13
B.7	Pt100-Thermometer	B-13
B.8	Pressure Sensors Endevco 8510-B-1	B-14
B.9	Setra 264	B-15
B.10	Setra 270	B-16

Nomenclature

Roman

a	wire thermal coefficient
a_0	pressure amplitude
A	cross section
c	blade chord
C_m	unsteady moment coefficient
\hat{C}_m	amplitude of unsteady moment coefficient
$\hat{C}_{m(c/2),rel}$	relative change in amplitude of the unsteady moment coefficient with respect to the baseline configuration
	$\hat{C}_{m(c/2),rel} = \frac{\hat{C}_{m(c/2),case} - \hat{C}_{m(c/2),baseline}}{ \hat{C}_{m(c/2),baseline} } \cdot 100$
cp_0	steady pressure coefficient, $cp_0(x) = \frac{p(x) - p_\infty}{q}$
cp	unsteady pressure coefficient, $cp(x, t) = \frac{p(x, t)}{\hat{\alpha}q}$
$\hat{c}p$	amplitude of unsteady pressure coefficient
Δcp	unsteady pressure difference coefficient, $\Delta cp(x, t) = cp_P(x, t) - cp_S(x, t)$
d	lever arm, strain gauge calibration device
$d_{torsion}$	distance from torsional spring to rotation axis, strain gauge calibration device
f	frequency
F	calibration factor, force, strain gauge
h	plunging displacement
\hat{h}	plunging amplitude
H	heat
k	reduced frequency, $k = \frac{2\pi fc}{U}$
K	coverage factor, Kelvin
l	length
L	length
n	sample size
N	blade count
p	pressure
p_∞	inlet static pressure
q	dynamic pressure

r	resistivity constant
R	resistance
R_{spec}	specific gas constant
s	blade span
t	time
tp	cascade pitch
T	period of oscillation, temperature
T_U	turbulence intensity
u	longitudinal velocity component, plunging displacement (spring)
$u_{torsion}$	torsional displacement, spring
u'	fluctuating velocity
U	flow velocity
U_0	inlet freestream (outside boundary layer) velocity
V	voltage
W	work, power
x_c	blade center of rotation relative to chord, here $x_c = 0.5$
x, y, z	spatial coordinates

Greek

α_0	cascade mean angle of attack
α	pitch displacement, $\alpha(t) = \hat{\alpha}e^{i\omega t}$
$\hat{\alpha}$	pitching amplitude
β	angular displacement
γ	cascade stagger angle
δ	logarithmic decrement
ϵ	strain
ζ	spatial coordinate
η	loss factor
θ	phase angle between aerodynamic modal force/moment and blade displacement; the angle is defined positive when the force/moment is leading the blade motion
λ	wavelength
Ξ	aerodynamic damping parameter
ϕ	phase response angle of pressure signal relative to motion; the angle is defined positive when the pressure signal is leading the blade motion
ρ	density
σ	interblade phase angle, standard uncertainty
ω	angular frequency

Subscript

0	initial condition
1	first harmonic
amb	ambient
B	bridge
cal	calibration
F	flutter
P	pressure side
<i>ref</i>	reference
S	suction side
t	total quantity
w	wire
wv	water vapour

Mathematical formulations

\Im	imaginary part of complex number
\Re	real part of complex number
\bar{s}	mean component of Reynolds decomposition
s'	fluctuation component of Reynolds decomposition
s'_{rms}	root mean square
$\langle s \rangle$	ensemble average of flow quantity
\sum	summation

Abbreviation

A/D	analog, digital
ADC	analog digital converter
CAN	controller area network
DLR	Deutsches Institut für Luft- und Raumfahrt e.V. (German Aerospace Center)
FS	full span
GF	gauge factor
HW	hot wire
IBPA	interblade phase angle
LE	leading edge
Ma	Mach number
NACA	National Advisory Committee for Aeronautics
ppm	parts per million, 1 parts per million = $1 \cdot 10^{-6}$
PS	pressure side

RMS	root mean square
Re	Reynolds number
sys	system
SS	suction side
TE	trailing edge

Chapter 1

Aeroelasticity in Turbomachines

1.1 Introduction

The design requirements of an aircraft engine are extremely challenging and oftentimes conflicting. The whole system demands a high degree of operational effectiveness, reliability and safety. At the same time, the engine has to be affordable, light weighted and more environmental friendly in order to reduce fuel consumption, emission of green house gases and noise level. In this regard, the design of turbomachine components, such as the blading, needs to be optimized, leading to complex 3D blade geometries with aggressive loading. These elastic and heavily stressed structures enhanced aeroelastic phenomena and thus failure are likely to occur by cause of instability or fatigue. High cycle fatigue (HCF) is a critical issue during the development of a new engine, El-Aini et al. [1] stated that more than 90 % of possible HCF problems are unveiled while testing, whereas the remaining nearly 10 % are responsible for almost 30 % of the overall development cost. Beside economical aspects, it should be noted that blade failure due to HCF can lead to severe safety problems and in the worst case to an engine loss. In april 2018, an emergency landing of a civil aircraft was reported at the airport of Philadelphia. One engine was lost due to a fan blade detachment. The results of the first investigation assumed material fatigue as main cause [2]. Therefore, it is evident that an accurate aeroelastic vibration analysis is necessary in the design and operation of turbomachines.

Aeroelastic phenomena arise when aerodynamic (A), elastic (E) and inertial (I) forces interact [3]. It is therefore an interdisciplinary engineering field, studying basically all structures exposed to a fluid flow. In 1946, Collar [4] was the first to introduce a triangle, see figure 1.1, visualizing the different disciplines and forces related to aeroelasticity: i) static (A+E) , ii) structural

dynamics (E+I), iii) flight mechanics (I+A) and iv) dynamic aeroelasticity (A+E+I). In the last decades, the original triangle was expanded, including e.g. thermal forces and control system inputs. In turbomachine aeroelastic literature, see e.g. [5, 6, 7], it is common praxis to define and distinguish between two main problems that belong to the field of dynamic aeroelasticity:

- Flutter is a self-induced and self-sustained blading vibration due to aeroelastic interaction. This instability arises when the blading experiences a vibration due to a small initial disturbance that cannot be damped out. Then, energy is transported from the fluid into the vibrating structure and the magnitude of the self-induced aerodynamic forces increases exponentially by each oscillation cycle. The mutual influence of individual blades in a row - also known as aerodynamic coupling - is a crucial aspect when assessing flutter stability.
- Forced Response describes the vibration response, that appears, when a blading is excited by a nonuniform flow field.

The difference between flutter and forced response is illustrated in figure 1.2 by using the Campbell diagram. It displays frequencies against rotational speeds of the engine shaft. The engine order lines represent the periodic excitation forces when they coincident with an eigenfrequency a resonance condition occurs. A resonance condition is depicted with a filled circle in the diagram, whereas a flutter incident does not ride the engine order line, depicted with a half filled circle. Among aeroelastic phenomena, flutter might be the one which is the most serious with regard to blade failure. It occurs almost exclusively in the fan, the front part of a compressor and the low pressure turbine, where the heavily loaded and shape optimized blades are long and slender and therefore prone to vibrate [6]. Usually, forced response is associated with rotor-stator-interaction, or vice versa, that occurs when a periodic flow pattern of an upstream blade row excites the downstream one [7].

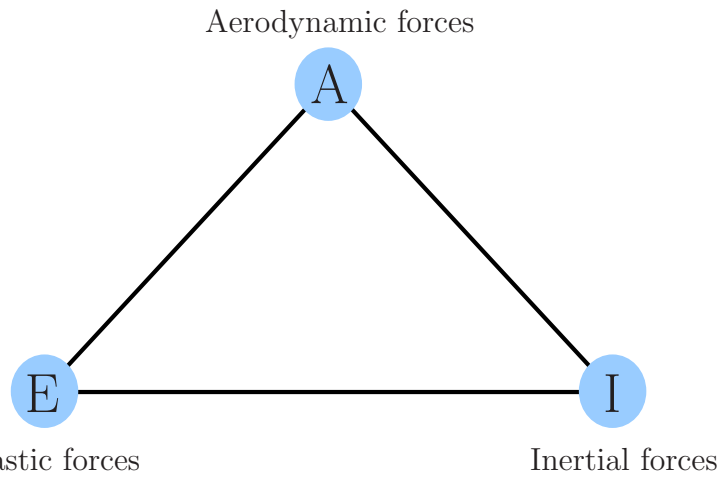


Figure 1.1: Collar's aeroelastic triangle, adapted from Ref. [8].

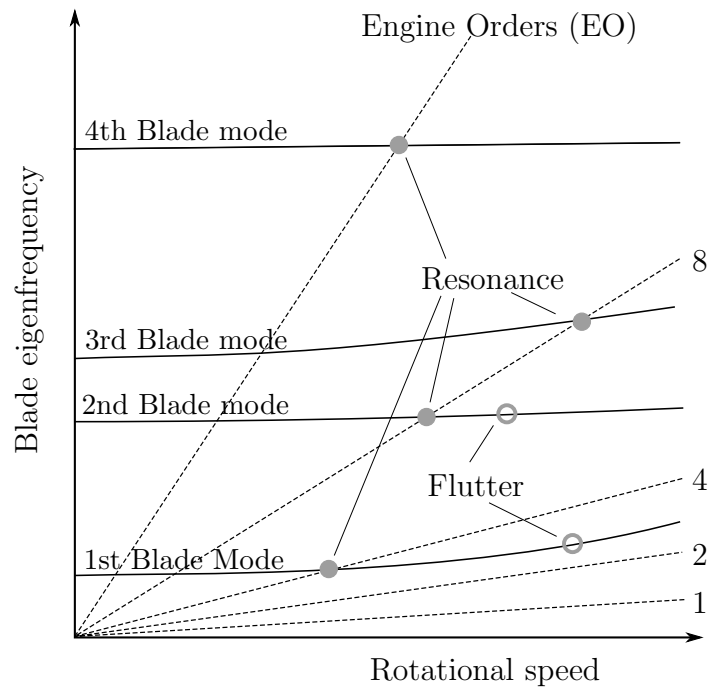


Figure 1.2: Campbell diagram, adapted from Ref. [9].

1.2 Flutter

Since the beginning of the early 20th century, flutter incidences were reported, but not fully understood and confound often with forced response [8]. Also, one of the most famous flutter incidence, the collapse of the Tacoma Narrows Bridge in 1940, was interpreted by several physics text books wrongly as externally forced mechanical resonance [10].

In figure 1.3, the main flutter types and their regions of occurrences are illustrated in a characteristic axial compressor or fan map. Stability maps and an in-depth discussion of flutter types are given in Refs. [11, 12, 38], hereinafter a short summary of the aforementioned references is presented. Flutter in a subsonic/transonic flow occurs in region I. In this regime, the blades are heavily loaded and flow separation is likely to be present. The separation is located on the pressure or suction side and governs the flutter mechanism. Region I is divided into a subregion, as flow separation is not considered the prime driver for system mode instabilities (region Ia). Alternatively, it has been hypothesized that oscillating shocks may help to describe the underlying mechanism of this flutter type [13].

Choke flutter (region II) appears commonly at part-speed operation and appears below the steady-state working line. At the moment, there are different understandings, among researchers, how choke flutter develops [14]. They agree that it involves the choking of the passage, oscillatory shocks, flow-separation at the leading edge, relatively low negative incidence and acoustic blockage [11, 14]. In some stability maps, the region is divided into two parts, and labeled as negative incidence flutter [15]. This region is associated by the authors with flutter occurrence at a greater negative incidence and decreased relative Mach number.

Supersonic flutter was detected in regions III, IV and V. In region III, flutter can occur along the working line in torsion or bending mode at low back pressure ratio and incidence. Regions IV and V are above the working line at higher incidence and back pressure ratio. In Region V, flutter has been almost exclusively observed in a bending mode with stalled flow and a detached shock at each passage entrance. On contrary in region IV, an oscillatory in-passage shock is assumed to be crucial for the development of flutter.

It is worth recalling that the map does not predict the flutter types and their occurrence with a very precise certainty, as the map does not include any information about structural dynamics.

In engine operation, flutter regions have to be avoided at any cost, if flutter is once initiated it cannot be stopped in most cases. To ensure the structural integrity of a turbomachines, the vibrations have to be reduced to

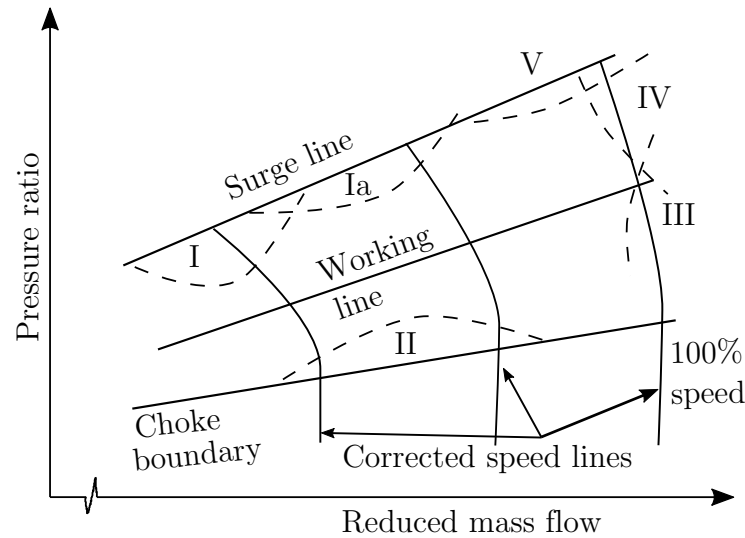


Figure 1.3: Axial compressor stability map illustrating main flutter types and their regions of occurrence, adapted from Ref. [12].

a minimum. A preventive measure is to increase the mechanical damping and/or to mistune individual blades in the row by increasing or reducing the blade mass. Mechanical damping can be added to the system by generating additional friction in the system. Snubbers, between neighboring blades, are used for this purpose [16]. Wires, connecting blades individually, are also applied at three-quarter span to increase the system stiffness [17]. These components modify the vibration modes of the system and thus the reduced frequency. A negative effect of these measures is that they disturb the flow and aerodynamic efficiency is degraded.

1.3 Thesis Motivation

In Ref. [18], Srinivasan published a list of parameters that influence blade vibrations due to aeroelastic phenomena. This list has been clustered and adopted into two main sections to account only for aeroelastic instability, see table 1.1.

As shown in the table, flutter depends on many parameters. Some of the aforementioned parameters have been proven to be more important than others.

Most of the mistuning research is carried out with regard to structural mistuning which was reported to increase the flutter boundary for a single-degree-of-freedom systems, see e.g. Refs. [19, 20, 21, 22, 23]. However, both structural

Table 1.1: Parameter list that influence the flutter mechanism.

Parameter	
aerodynamic	structural
incidence angle blade loading separation point pressure distribution on blade surface shock position and motion inlet/outlet conditions relative inlet Mach number velocity and pressure defects	gap/chord, number of blades blade geometry hub/tip ratio aspect ratio shroud location and shroud angle mode shape mistuning inter blade phase angle mechanical damping
coupling reduced frequency	

and aerodynamic mistuning influence the stability of the system. Aerodynamic mistuning is associated with geometrical changes in the flow passages such as stagger-angle, blade-to-blade spacing variation and blade blending, stemming from manufacturing errors or repairs. Those differences change the blade pressure distribution and thus the aeroelastic response. The few realized investigations with regard to aerodynamic mistuning were almost exclusively of numerical nature, see Refs. [24, 25, 26, 27]. Thus, the thesis motivation is:

1. to extent the physical understanding of the effect of aerodynamic mistuning on aeroelastic stability in compressor cascades,
2. to experimentally verify the trends in the aforementioned publications,
3. to create test cases for aerodynamic mistuning for aeroelastic stability assessment in a compressor cascade.

The experimental investigation is realised by studying the aerodynamic response of an aerodynamically mistuned oscillating compressor cascade. From the acquired data, stability parameters are computed in order to assess the cascade stability.

Chapter 2

State of the Art

2.1 Fundamental Concepts in Aeroelasticity

2.1.1 Aeroelastic Modeling

The modeling of aeroelastic behaviour in turbomachines considers in most cases blade rows as it is closer to real engine applications than an individual blade. The reason for that is the aerodynamic coupling: the vibration of each individual blade alters the flow field in its direct surrounding, causing a response on itself as well as on the adjacent blades [39]. The importance of coupling effects was verified by early experimental studies of Triebstein [28] and Carta and St. Hilaire [29] who observed that the aerodynamic response in an oscillating cascade was highly affected by aerodynamic coupling.

Lane [30] was the first to present an analytical formulation of the aeroelastic behaviour of a blade row. Aiming to create an efficient model of the complex system, he applied linearised theory and assumed cyclic symmetry. He characterized the system mode shapes as a traveling wave where all blades oscillate with the same amplitude, frequency and mode but at a certain constant phase lag. The phase lag between two neighbouring blades is called interblade phase angle (IBPA). For each mode family, a forward and backward wave, also referred to as positive and negative, can evolve. For rotor blades the wave that travels in the same sense of rotation is referred usually as positive. The IBPA has discrete values and is defined as

$$\sigma_n = \frac{2\pi n}{N}, n = 0, 1, 2, \dots, N - 1 \quad (2.1)$$

$$\sigma_{N-n} = \sigma_{-n}, \quad (2.2)$$

where n is the order of traveling wave, also known as nodal diameter, and N the blade count of the row.

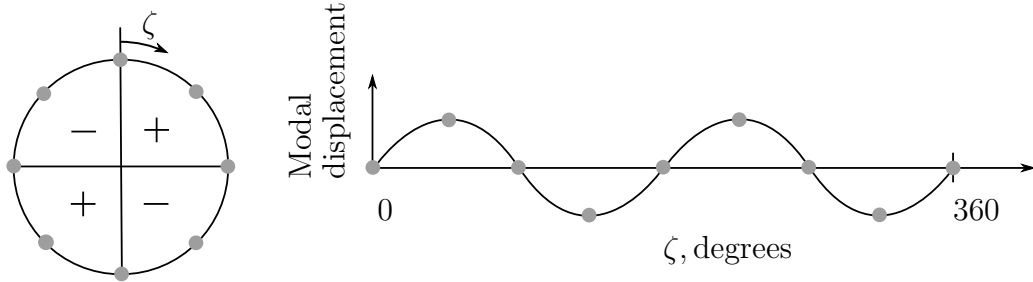


Figure 2.1: Modal displacement for a bladed disc with $N=8$ with nodal diameter 2. The grey filled circles indicate the blade positions.

The concept of IBPA can also be illustrated by disk modes that are called usually nodal diameters. The maximal nodal diameter count of a bladed disk is dependent on the number of possible diametrically opposite sections, yielding to $N/2$ for even blade count and $(N-1)/2$ for odd. As an example: the Lane criterion allows eight IBPAs ($\sigma_0 - \sigma_7$) for a rotor with eight blades, leading to maximally four nodal diameters. Zero nodal diameter is equivalent to $\sigma_0 = 0$ degrees, all blades oscillate harmonically without time lag between adjacent blades. Nodal diameter one is similar to $\sigma_1 = 45$ degrees, two to $\sigma_2 = 90$ degrees, three to $\sigma_3 = 135$ degrees and four to $\sigma_4 = 180$ degrees. For higher indices of σ see again equation 2.2, yielding to $\sigma_5 = -\sigma_3$, $\sigma_6 = -\sigma_2$ and $\sigma_7 = -\sigma_1$, those waves are considered to be negative or travel backwards. In figure 2.1, the nodal diameter two is depicted on the left side as an example, whereas the associated modal displacement is plotted versus an azimuthal coordinate ζ on the right. This nodal diameter yields to a periodic flow pattern with a wave number of two. The IBPA is, together with the aerodynamic damping and reduced frequency, one of the most important parameter in turbomachinery aeroelasticity and the underlying linearized theory is applied widely in experimental and numerical set-ups.

2.1.2 Aerodynamic Damping Parameter

Early works of Carta [31, 32] introduced an aerodynamic damping parameter. It is an essential measure in the aeromechanical design of turbomachinery blades as it is part of the overall system damping, beside the friction and material damping. It is a phenomenon resulting from the interplay of a vibrating blade and its surrounding flow, subjected to the specific flow condition, IBPA, blade mode shape and oscillation frequency [34]. For most definitions, a positive aerodynamic damping indicates a stable system. Thus, the flow damps the vibration. In case it becomes negative and is not balanced by the friction and material damping, vibration amplitudes will rise rapidly,

indicating flutter onset. In forced response analysis, an accurate aerodynamic damping prediction is also fundamental to control the maximum responding vibration amplitude in terms of a resonance condition.

The aerodynamic damping is computed with the help of the aerodynamic work that is the work done by the fluid on a blade during one oscillation period. If the work per cycle is negative, energy passes from the oscillating structure to the flow, having a stabilizing effect. For positive work, the energy flow reverses direction, destabilizing the system if not properly damped.

With the aerodynamic modal force F acting on the blade and the blade displacement h , the aerodynamic work can be computed as following:

$$W = \oint F(h)dh. \quad (2.3)$$

Equation 2.3 can be reformulated by assuming harmonic blade motion,

$$h = h(\omega t) = \hat{h}\cos(\omega t), \quad (2.4)$$

and substituting

$$dh(\omega t) = -\hat{h}\sin(\omega t)d(\omega t) \quad (2.5)$$

and the Fourier series representation of the unsteady modal force,

$$F(h(t)) = \sum_{n=1}^N \hat{F}_n \cos(n\omega t + \theta_n), \quad (2.6)$$

in equation 2.3, yields

$$W = \int_0^{2\pi} F(h(t))dh(\omega t) \quad (2.7)$$

$$= -\hat{h} \int_0^{2\pi} \sum_{n=1}^N \hat{F}_n \cos(n\omega t + \theta_n) \sin(\omega t) d(\omega t) \quad (2.8)$$

$$= \pi \hat{h} \hat{F}_1 \sin(\theta_1). \quad (2.9)$$

When solving the integral in equation 2.8 only the first harmonic term, $n=1$, remains whereas the other terms, $n=2\dots N$, are zero. θ_1 is the phase angle between the first harmonic of the modal force and the blade displacement. The phase is defined positive when the force is leading the motion. Thus, the aerodynamic work is positive if $\sin(\theta_1) > 0$ i.e. θ_1 ranges between $0\dots 180$ degrees.

To assess system stability, the aerodynamic work is normalized by the oscillation amplitude \hat{h} and π as reported e.g. by Carta [33]:

$$\Xi = -\frac{W}{\hat{h}\pi}. \quad (2.10)$$

Ξ is also known as aerodynamic damping. The presented computation of the aerodynamic damping parameter assumes a simple linear system and no influence of the unsteady aerodynamics forces on the mode shapes.

Compared to the properties of the structure, Mayorca [34] states that the aerodynamic damping can arrive at values in the order of magnitude of the friction damping. Especially for integrally bladed rotors, also known as Blade Integrated Disk (BLISK), that are manufactured from a single piece of material, an accurate aerodynamic damping prediction becomes inherently important. In the absence of friction damping, material and aerodynamic damping are the only sources of damping. Srinivasan [18] reported that material damping of titanium and nickel based alloys are negligible, for a fan blade made of titanium alloy (8-1-1), a loss factor (η) of 0.0003 in the first and second bending and 0.0001 in the torsion mode was measured. In the aforementioned publication, the loss factor is computed by dividing the logarithmic decrement δ by π , yielding to $\eta = \frac{\delta}{\pi}$. For a detailed description of the measurement set-up refer to the report of Srinivasan et al. [35]. A more recent study was published by Kielb et al. [36] who investigated multiple damping sources in a full-scale turbine rig. The experiments were carried out at engine conditions and actual hardware was used for the vane nozzles and rotor blades (Honeywell TFE 731-2). The authors reported that the aerodynamic damping is a large portion of the overall system damping. The determined aerodynamic damping for both investigated torsion and bending modes increased the critical damping ratio up to a factor of ten.

2.1.3 Reduced Frequency

Meldahl [37] introduced the reduced frequency as a further parameter, dominating the flutter behavior in cascades. It is a non-dimensional ratio, relating the time scale of the flow to the blade oscillation period. It is also understood as a measure for the unsteadiness of the problem and is defined as

$$k = \frac{2\pi fc}{U}, \quad (2.11)$$

where, f is the oscillation frequency, c the blade chord and U the upstream velocity. It means for small reduced frequencies that a fluid particle travels very fast across the blade chord compared to the oscillation period. Therefore, the

flow characteristic can be considered as quasi-steady and the flow unsteadiness increases by higher reduced frequencies. A more physical explanation is given by Cumpsty [38], summarized in the following, associated to the circulation around the blade: As it oscillates, the pressure distribution around the blade is altered and so is the lift it generates, which means that some vorticity has to be shed downstream at an approximate exit velocity of U_{exit} . Within one oscillation cycle, it is convected downstream in a distance of $\lambda = \frac{U_{exit}2\pi}{\omega}$ from the blade trailing edge. For a reduced frequency of $k = 1$, the shedded vortices will travel 2π chord lengths downstream in one oscillation period. This distance is reduced as k rises, and hence the effect of the vortices on the blade is increased, implying greater unsteadiness.

Every blade row has a characteristic reduced frequency by which the system becomes aeroelastically unstable. Srinivasan [18] reported values of k between 0.4,...,0.7 for fan rotor blades at which flutter has been noticed. It should be noted that in his publication, the reduced frequency is based on the semichord more commonly used in American literature. Vogt [39] states more generally that critical reduced frequencies for turbomachine blades have been observed in the range of 0.1,...,1. In Ref. [12], Jay and Fleeter present a table of reduced frequencies common for rotor flutter. For unstalled supersonic torsion flutter, they specify a range of $k = 0.7$ to $k = 1.3$, for supersonic bending flutter a $k = 0.2$ to $k = 0.5$, for subsonic/transonic torsional stall flutter a $k = 0.4$ to $k = 1.6$ and for choke bending flutter a $k = 0.3$ to $k = 0.5$. They defined the reduced frequency as $k = \frac{2\pi fc}{U}$. Manwaring et al. [40] investigated the response of a transonic fan due to an inlet distortion for $k = 1.8$ and 4.6, they computed k with the semichord.

2.2 Flutter Testing Methods

In flutter testing, two main methods can be distinguished [39]. The first one is a test set-up in which the blades in a cascade are mounted elastically and can vibrate freely. They are exposed to a fluid flow and the velocity is increased gradually. The objective of these tests is the detection of the flutter onset velocity, the aeroelastic eigenfrequency and the critical IBPA. In the past, experimental data of free flutter tests have been used mainly to validate numerical simulation in terms of flutter onset velocity. Especially, these flutter tests can be risky, to avoid a blade detachment and the destruction of the set-up, a well designed flutter brake is essential. In advanced set-ups, the elastic suspensions are designed in a way that balancing masses can be added to account for a frequency tuned or mistuned system. An example of a free flutter testing facility is presented in Ref. [7].

The second one is a controlled or forced vibration flutter test that has a different focus than free flutter tests; the objective is to investigate the unsteady aerodynamic response of an oscillating cascade. From the experimental data, the aerodynamic damping can be computed, and thus system stability can be assessed. Within the test set-up, the blades are forced harmonically to vibrate and exposed to a fluid flow. In most test facilities, the aerodynamic excitation is generated by the blade motion. Rather rare is a system excitation with an aerodynamic force.

Two methods for controlled flutter tests have been established: traveling wave mode (TW) and influence coefficient testing (IC). They apply linearized theory that has been outlined in subsection 2.1.1, for in depth reading refer to Refs. [30] and [41]. When using a traveling wave test set-up, the blades of the cascade vibrate at the same frequency and mode shape but at a certain constant phase angle between adjacent blades (IBPA). The experimental data is acquired on one blade. Depending on the blade oscillation device, different IBPAs can be studied. The oscillation device limits also the range of reduced frequencies that can be investigated. Mechanical, see Ref. [42], electromagnetic, see Ref. [43], and hydraulic, see Ref. [44], mechanisms have been used to force the blades to perform harmonic motions.

Hanamura et al. [45] presented, as one of the first, an experimental study of the validity of the influence coefficient technique in an oscillating compressor cascade. They forced one blade to oscillate, acquired the unsteady data on the oscillating blade itself and on its neighbors. Then, the data was superimposed to account for aerodynamic coupling between adjacent blades and for different IBPAs. Several studies investigated the aerodynamic coupling effects for cascade flutter in the influence coefficient domain, see e.g. Refs. [39, 44, 46]. For the studied test cases, they reported that the coupling effects are decaying rapidly after a distance of two pitches with regard to the reference blade.

Both testing methods can be carried out in linear, annular or sectional cascades. However, the most natural model to investigate flow in a turbomachinery environment is an annular cascade. The set-ups are equipped conventionally with measurement techniques to acquire the blade motion and frequency as well as the steady and unsteady blade surface pressure. Further, the measurement set-up includes devices to monitor the wind tunnel parameters.

Free and controlled flutter tests have both advantages and disadvantages. The disadvantage of free flutter experiments are that only the least stable

interblade phase angle can be measured in order to avoid a destruction of the test facility, or rather the very first flutter onset velocity. Further, it is not possible to acquire aerodynamic damping data for various IBPAs and the designed aeroelastic suspension may allow only certain blade mode shapes, see e.g. Ref. [7]. In contrary, the complexity of controlled flutter set-ups compared to the free flutter one is higher, due to the design requirements of the blade oscillation device and the control system. The control system has to ensure an accurate realization of multiple constant IBPAs between adjacent blades, whereas the blade device has to guarantee a harmonic sinusoidal blade motion that is as close as it can get, due to manufacturing tolerances, to its mathematical description. In low speed regimes, the influence coefficient testing can be challenging, if oscillation amplitudes are small, the signal-to-noise ratio for the pressure signal acquired on the non-oscillating blade surface can be very low. However, if a controlled flutter set-up has been commissioned successfully, wide ranges of parameters with regard to different reduced frequencies, oscillation amplitude and frequency and inflow condition can be studied.

2.3 Review of Oscillating Cascade Experiments

In the following section, experiments in which the system is excited by harmonic blade motion are reviewed, since they are the most relevant for this thesis. Oscillating cascade experiments apply either the influence coefficient method or a traveling wave set-up. The references are reviewed chronologically, but studies that were carried out at the same test facility are clustered together.

In 1977, some of the earliest work in this field was published by Fleeter et al. [47]. Working at the Detroit Diesel Allison facility, they compared their experimental results with two different analytical predictions. The work was carried out in a traveling wave set-up in combination with a linear cascade. Airfoil profiles pitching in a sinusoidal motion were studied, featuring flat suction sides and triangular pressure surfaces. At supersonic Mach numbers of 1.5 - 1.6 and for a reduced frequency range of $k = 0.18, \dots, 0.13$, they reported that their data agreed well with their predictions with regards to surface pressure distribution. However, shock location and shock-airfoil interaction could not be predicted so well, highlighting an issue in airfoil aerodynamics that remains problematic even today.

Much of the foundational work on oscillating cascaded airfoils was done by Carta and St. Hilaire [29, 31, 32, 48]. Utilizing a subsonic linear com-

pressor cascade in a traveling wave set-up, they investigated the unsteady aerodynamics of airfoils oscillating in pitch. The airfoil featured a NACA 65-series cross-section. In contrast to many other publications, they based their definition of k on the semi-chord. Carta and St. Hilaire [29] studied the effect of three large mean incidence angles (6, 8, 10 degrees) on the unsteady aerodynamic response. Reduced frequencies of up to 0.193 and an IBPA range from $\sigma = -60$ degrees to $\sigma = 60$ degrees were investigated. At the largest incidence angle, flow deterioration was observed, having a destabilizing effect on stability. Carta presented especially in Ref. [32] a very comprehensive study of the unsteady aerodynamics of an oscillating compressor cascade. In this investigation, test cases with three reduced frequencies ($k = 0.072, 0.122, 0.151$), two oscillation amplitudes of $\hat{\alpha} = 0.5$ degrees and $\hat{\alpha} = 2$ degrees, two different mean camber line incidence angles ($\alpha_0 = 2$ degrees, $\alpha_0 = 6$ degrees) and a IBPA range of $\sigma = 0 : 45 : 315$ degrees were studied. All possible parameter combinations were considered. A primary finding for $\alpha_0 = 2$ degrees is that all amplitudes of the pressure response are periodic for both pitching amplitudes. For the larger mean incidence angle, periodicity of the pressure amplitudes is not given at the leading edge regions. Pressure phase angles were also observed to be periodically for all test cases, except for IBPA $\sigma = 0$ degrees, for which a strong gapwise gradient was reported. This has been suggested to be related to a cascade acoustical resonance condition. Further, he reported that changes in reduced frequency did only marginally affect the chordwise pressure distribution. Carta compared also the real and imaginary parts of the unsteady pressure difference coefficient for $\alpha = 2 \pm 0.5$ degrees and a reduced frequency of $k = 0.122$ with the Verdon/Caspar "real blade theory" [49]. He reported an excellent agreement between theoretical and experimental data for the complete range of investigated IBPAs.

The finding that all mentioned studies of Carta et al. have in common is that the interblade phase angle affects most the stability of an oscillating compressor cascade.

In 1983, Bölcs [50, 51] introduced at the Swiss Federal Institute of Technology in Lausanne a non-rotating annular cascade capable of Mach numbers up to $Ma = 1.4$. His experiments focused on quantifying stability parameters and investigations on the influence of IBPA in combination with different inlet flow angles and exit Mach numbers. The experiments have been carried out in a traveling wave set-up, the rig can be equipped either with compressor or turbine blades. The blades are vibrating in a rigid-body torsion mode. The annular facility at Lausanne was used by Belz and Hennings [52], who reported on a series of flutter experiments with a compressor cascade comprising 20 NACA 3506 blades. They compared two transonic cases with inlet Mach numbers of $Ma = 0.87$ and $Ma = 0.9$. The first test case featured a reduced frequency of $k = 0.362$ and the second one of $k = 0.289$. At the lower reduced

frequency, the cascade was found to be aerodynamically unstable, with a channel shock near the trailing edge of the suction side that significantly impacted stability.

Rottmeier [9] investigated the effects of upstream gusts on the unsteady aerodynamics of a turbine cascade vibrating in a controlled traveling wave mode. Using a subsonic (outlet Mach number $Ma = 0.67$, $k = 0.281$) and a transonic ($Ma = 0.93$, $k = 0.205$) test case, he showed that the phase angle between gust excitation and cascade vibration is a key parameter in such systems: The interaction of cascade and gust excitation is strongly influenced by it, which implies that a well-chosen gust-vibration angle might be useful to control or diminish a given cascade excitation mode.

A more recent result from the Lausanne facility was presented by Vega et al. [53], who investigated the aeroelastic stability of blade pair packages. 20 blades typical of low pressure turbine stages were oscillated in a traveling wave form, while inlet Mach number and reduced frequency were set to $Ma = 0.34$ and $k = 0.7$, respectively. It was found that blade pairing has a stabilizing effect on the torsion mode due to suppression of unsteadiness on the suction side, but has only a marginal influence on stability of bending modes.

At the NASA Lewis oscillating cascade, Buffum and Fleeter [46] introduced an unsteady aerodynamic influence coefficient method, which requires only a single instrumented airfoil to oscillate at a time. The facility features a linear cascade. Uncambered biconvex airfoils oscillating in pitch were used in this work. They conducted subsonic ($Ma = 0.65$) measurements at reduced frequencies of $k = 0.223$ and $k = 0.390$, based on the semi-chord. Their results agreed well with previous experiments and predictions, thus demonstrating the validity of the influence coefficient technique. At the same test rig, Buffum et al. [54] studied the influence of a large mean incidence angle (10 degrees) on the cascade aerodynamics and compared it to a baseline case, featuring an incidence angle of 0 degrees. For this study, airfoils with a cross-section of a tip region of a low aspect ratio fan were used, oscillating all blades at the same frequency but a certain constant IBPA. With an inlet Mach number of $Ma = 0.5$ and reduced frequency values of $k = 0.4$, $k = 0.8$ and $k = 1.2$, they found that an increased incidence angle will significantly affect unsteady blade pressure distributions, in particular with regard to flow separation: At an incidence of $\alpha_0 = 10$ degrees, they showed that the suction surface will experience leading edge separation, with eventual reattachment around the 40 percent chord region. Furthermore, they established opposite trends for attached and separated flow near the leading edge: while attached flow had strongly stabilizing influences, detached flow would affect stability

negatively.

Sachs introduced an unique test facility, combining free and controlled flutter testing methods at the German Aerospace Center in Göttingen [7]. The outline of the setup is very similar to the one Carta used, in terms of flow regime, airfoil and blade count, see e.g. Ref. [33]. It is a linear cascade with nine elastically suspended blades allowing free and controlled blade oscillation in two degrees of freedoms, namely pitching and plunging. The research was aiming to broaden the physical understanding of the unsteady aerodynamics of an oscillating compressor cascade and to create a data base of aerodynamic coefficients and flutter parameters. Sachs studied a range of reduced frequencies of $k = 0.054, \dots, 0.539$, two pitching amplitudes ($\hat{\alpha} = \pm 0.5$ degrees, ± 2 degrees) and one plunging amplitude ($\hat{h} = \pm 3$ mm), two angle of attacks ($\alpha_0 = 2$ degrees, $\alpha_0 = 6$ degrees) and an IBPA range of $\sigma = 0, \dots, 315$ degrees in steps of 45 degrees or 90 degrees for pitching and plunging mode. All tests were carried out in a traveling wave set-up. For the pitching mode, Sachs reported a very small dependency of the reduced frequency on the unsteady moment coefficient (related to half chord) for the investigated interval ($k = 0.054, \dots, 0.539$), even a small reduction of the moment coefficient was noted with increasing k . The system was observed to be slightly more damped when k increased. If the blades undergo a plunging motion, the unsteady lift coefficient was reported to increase significantly from the minimum to the maximum investigated values of k . However, the damping trend was similar compared to the pitching mode, the system was more damped for high values of k . Hennings [5] used the same facility for his investigations, introducing blade suspensions equipped with strain gauges. He proofed that a traveling wave mode develops in a linear cascade for free flutter testing, and that the acquired data can be considered as a valid approximation of investigations in an annulus. The prediction and experimentally investigation of the flutter onset velocity and the associated interblade phase angle were also part of this study and were found to be in good agreement. Parts of the experimental set-up of Sachs and Hennings, including the blade suspensions, were used in the current work.

In 1993, Poensgen and Gallus applied also the influence coefficient method, the controlled flutter experiments were carried out at the RWTH Aachen's annular compressor cascade [55]. One blade can oscillate in bending or torsion mode. Covering a range of low subsonic Mach numbers ($0.186 < Ma < 0.27$) and relatively high reduced frequencies (based on the semi-chord) from $k = 0.37$ up to $k = 0.922$. They exposed the cascade to both steady and unsteady inlet flows, showing that the blade pressure distribution could be represented as a linear superposition of blade motion and incoming wakes.

Bell and He [56] investigated the three-dimensional unsteady aerodynamic response of an oscillating blade. They conducted experiments at the low-speed Durham two-passage linear turbine cascade, which is capable of realistic values for reduced frequency and Reynolds number, i.e. $Re = 4.5 \cdot 10^5$ and $k = 0.5$. A rigid blade with constant cross-section was forced to oscillate in a bending mode. In a later publication, see Ref. [57], they investigated the influence of tip leakage on an oscillating turbine blade and reported a significant impact on the unsteady pressure response: Even at a considerable distance from the tip, a change in tip gap resulted in a consistent variation in unsteady pressure response. The tip-clearance gap degraded the system stability for all interblade phase angle.

An influence coefficient method was used by Frey and Fleeter [58] at the Purdue Axial Flow Research Compressor, a low speed-compressor. This work quantified the unsteady aerodynamics of a rotor stage oscillating in a rigid-body torsion mode at a Reynolds number of $Re = 6.3 \cdot 10^5$ and two reduced frequencies of $k = 0.282$ and $k = 0.29$, finding a strong effect of oscillation amplitude and steady loading on surface pressures. Results indicate that at oscillation amplitudes greater than 5 degrees, the aerodynamic response of an oscillating blade row becomes non-linear, making analysis of just the first harmonic insufficient.

Vogt and Fransson [59] introduced a new facility for the investigation of turbomachine aeroelasticity via an influence coefficient method at KTH Stockholm. The rig is an annular-sector, non-rotating cascade consisting of 9 blade passages, with the blades exhibiting a low pressure turbine rotor profile. While the facility is designed for an engine-like inlet Mach number of $Ma = 0.31$, the blade actuation mechanism is capable of varying the reduced frequency from $k = 0.05$ to $k = 0.6$. The test rig is unique in the regard that it enables the investigation of blades oscillating in complex, but controlled three-dimensional mode shapes under realistic 3D flow conditions. Vogt utilised this facility to conduct a thorough investigation of various three-dimensional effects in turbine flutter, presented in [39]. He established the presence of significant three-dimensional effects, mainly in the form of a radial gradient in unsteady response magnitude. He thus surmised that the accuracy of flutter stability prediction might be improved by switching from a two-dimensional plane model to a fully three-dimensional one that also takes tip clearance into account.

Glodic et al. [60] used the same test rig at KTH to research the relationship of aerodynamic mistuning and aeroelastic stability in low-pressure turbines. They compared a nominal and a mistuned case, investigating reduced frequencies from $k = 0.1$ to $k = 0.4$ and keeping the outlet Mach number at $Ma = 0.4$. Mistuning was realised by varying the stagger angle of the cascade's central

measurement blade from -2.5 to 2.5 degrees. They employed both an experimental influence coefficient technique and a numerical model, which in general were found to be in good agreement. They concluded that mistuning can have a moderate influence on aerodynamic stability, with the direction of the effect depending on the exact nature of the mistuning. The majority of randomly mistuned configurations were however found to exhibit higher stability.

Keerthi et al. [61] presented results from an unstaggered, low-speed linear compressor cascade that shed light on how localized flow accelerations can affect the global flow field. The cascade consists of five blades, the central blade is fixed and the upper and lower neighboring blades can be forced to oscillate in pitch. These measurements were performed at a reduced frequency of $k = 0.3$ and an inlet velocity of $Ma = 0.085$. The motivation of the study was to establish a relationship between the central blade surface pressure and the phase shift between the adjacent blades. From their findings, the authors suggested that the airfoil shape not only directly influences aerodynamic behavior by directing the flow, but also through causing localized phenomena such as steep pressure gradients or even separation regions.

More recently, Keerthi and Kushari presented results from an annular compressor cascade, quantifying the aerodynamic damping at three relatively large mean incidences, namely 3.6, 9.2, 23.3 degrees (measured at % 50 span). The motivation of the study was to deepen the understanding of unsteady aerodynamics in a stalled turbomachine environment. Within the cascade, five blades can oscillate pitch-wise about the mid-chord. Airfoils with a prismatic double circular arc profile were applied. They conducted their experiments at a low subsonic inlet velocity of $Ma = 0.1$, varying the reduced frequency in a range from $k = 0.06$ to $k = 0.3$. The motivation of this work was to broaden the understanding of stall flutter. Flow separation at the leading edge region for the test cases was reported. They found that incidence not only affected pressure magnitudes, but also had a significant effect on pressure phase that altered blade stability [62].

A two passage linear turbine cascade for flutter investigations in heavy-duty gas turbines was presented by Seeley et al. [63]. This facility was accordingly designed to match a typical last stage of such turbines both geometrically and with regard to the flow regime. The blade rotates about the pitch axis. Working over a wide range of exit Mach numbers from $M = 0.1$ to $M = 1.2$, they investigated the effect of vibration amplitudes on aerodynamic forces and damping. While the forces were found to be linear with respect to vibration amplitude, aerodynamic damping was constant outside of a flutter region for high Mach numbers $M = 0.8 - 1.2$.

In 2018, a traveling wave study of controlled flutter was done by Slama

et al. [64] at the subsonic wind tunnel at the University of Western Bohemia. They arranged 8 turbine blades, 4 of which are instrumented, in a linear cascade to investigate the stability of both torsion and bending modes at $M = 0.34$. The blades vibrate with a frequency of $f = 82.2$ Hz. Stability in terms of an aerodynamic work coefficient was demonstrated to depend on the interblade phase angle and agrees with CFD results varying from case to case.

Standard configurations and AGARD Manual on Aeroelasticity

Due to the great diversity in methods, nomenclature, test facilities and set-ups in turbomachinery aerolasticity research, a big effort was undertaken by Bölcs and Fransson [43] to compile a set of guidelines, containing specifications for nine different cascade geometries as well as accompanied numerical results. They are called "Standard Configurations", and became over time true standards in turbomachinery aeroelasticity research. These configurations were based on facilities existing at the time at various research centres, which (like the cascade at NASA Lewis) have been mentioned in the previous section.

Of greatest relevance for the present work is certainly the first standard configuration, which specifies a compressor cascade in low subsonic flow based on Carta's UTRC facility. In an update to the standard configurations [65], Fransson and Verdon noted that although pressure distributions in such cascades could be predicted fairly accurately under certain conditions, agreement between theory and experiment was not as good as one might wish, and that further research on this configuration was needed.

In addition, also due to the complexity of the observed phenomena, the Advisory Group for Aerospace Research and Development published the AGARD Manual on Aeroelasticity to distinguish clearly between the reported aeroelastic phenomena encountered in turbomachines, to standardize important parameters, to give an overview of the current research situation and to identify trends and challenging research topics. Two volumes were published in 1988 [12] and 1989 [66], respectively. They are known as the 'AGARD Manuals' and still referenced widely.

Chapter 3

Objectives and Approach

Aerodynamic mistuning that might be caused from manufacturing error or repairs lead to small changes, e.g. in stagger angle, influencing the unsteady aerodynamics of an oscillating cascade. As discussed in the literature review, systematic experimental investigations focusing on aerodynamic mistuning are limited. Within this framework, the overall objective of the present work is to describe the underlying mechanism of aerodynamic mistuning on aeroelastic stability. Sub-goals of the thesis are:

- to study the effect of different mistuning pattern on the cascade's steady and unsteady aerodynamics;
- to examine the effect of the aerodynamic mistuning on the aerodynamic damping;
- to identify driving parameters of the cascade stability in the case of aerodynamic mistuning.

The experimental study has been realized by measuring the aerodynamic response of an aerodynamically mistuned oscillating compressor cascade. At a constant reduced frequency, measurements have been taken for a wide range of different IBPA for a variety of mistuning patterns. The aerodynamic mistuning is introduced by a blade-to-blade stagger angle variation. To make the blades oscillate in a traveling wave mode, a drive system in combination with a control software was developed. Measurement blades were developed, designed and manufactured to acquire the blade surface pressures. Actions were taken to improve the base flow of the test rig by designing a new diffuser incorporating screens with different porosities.

After the installation of the test rig at the Technische Universität Berlin, the facility has been thoroughly commissioned in terms of base flow characteristics such as the velocity profiles and the turbulence intensity in the inlet section, as

well as the steady blade pressure distribution. The unsteady performance has been checked by comparisons against data from literature. These measures have been undertaken to give a substantial background to the presented study.

Experimental data have been analyzed in terms of steady and unsteady blade pressure distributions for different reduced frequencies and mistuning patterns. The aerodynamic damping parameter has been computed to assess cascade stability, and the Fourier Transform Technique has been used to assess the pressure frequency spectrum. Conclusions were drawn in regards to which extent mistuning influences the cascade stability and how the stability characteristics of the system change.

Chapter 4

Test Facility and Measurement Technique

The experimental investigations were carried out at the aeroelastic test facility at the Chair for Aero Engines of the Technische Universität Berlin. The test rig consists of a wind tunnel and a measurement section. The latter contains an oscillating compressor cascade, a mechanism to generate a periodic inlet flow and various traverse systems.

The original set-up of the test facility was developed and operated at the Institute of Aeroelasticity of the German Aerospace Center in Göttingen (Germany), see section 2.3.

The test rig components were moved to the chair of Aero Engines at the Technische Universität Berlin. Some components of the rig have been adapted and several modifications were introduced. In the framework of the current thesis, a new diffuser was installed, comprised of two parts, allowing the integration of meshes to optimize the inflow. A new blade excitation system was set up, the cascade configurations was changed and measurement blades were developed and manufactured to acquire the unsteady pressure distribution on the blade surface. The sidewalls of the measurement section were replaced by longer ones to improve flow smoothness and a mechanism to generate a periodic inlet flow was installed.

In the following, the wind tunnel set-up is described in section 4.1, the measurement section including the oscillating compressor cascade and the related drive system in section 4.2 and the applied measurement techniques in section 4.3.

4.1 Wind Tunnel for Aeroelastic Investigation

The wind tunnel has a classical set-up consisting of a blower, compensator, diffuser, settling chamber, nozzle and measurement section including a mechanism to generate a periodic inlet flow. It is depicted in its current state in figure 4.1 . The dimensions of the individual components are summarized in table 4.1. It is an open-circuit test facility, which means that lab air is sucked in by a radial compressor and also blown into the lab after the outlet of the measurement section. The inlet air velocity of the test section attains a Mach number of $Ma \sim 0.1$.

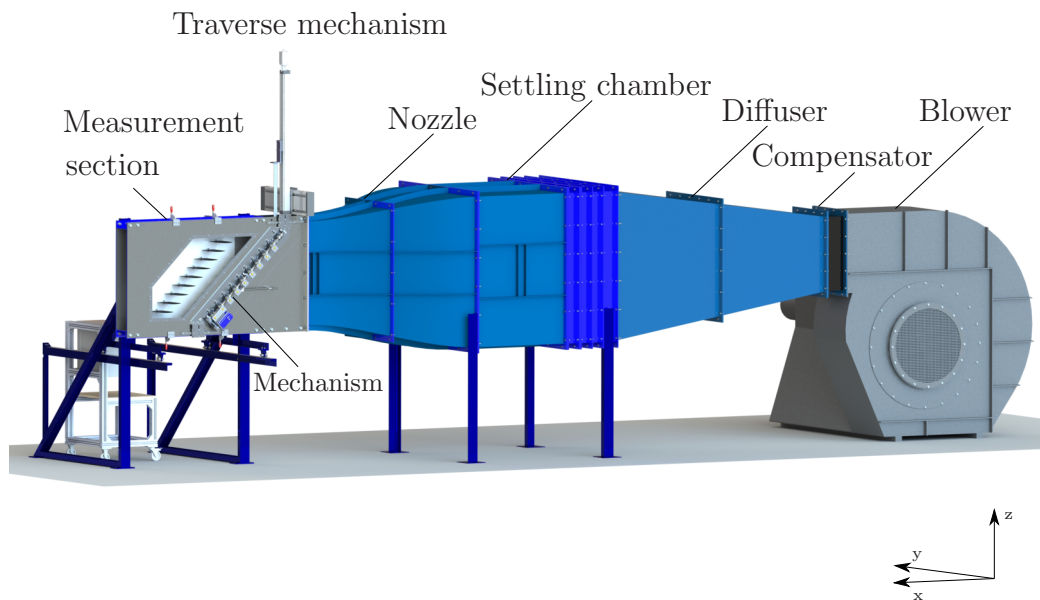


Figure 4.1: Wind tunnel with a linear oscillating compressor cascade for aeroelastic investigation at the Chair for Aero Engines at TU Berlin.

Table 4.1: Geometrical parameters of the wind tunnel.

	cross section mm ²	length mm
Compensator	550x700	210
Diffuser		
Inlet	550x700	
Outlet	1400x1400	2500
Settling chamber	1400x1400	1495
Nozzle		
Inlet	1400x1400	
Outlet	200x955	1500
Measurement section	200x955	1920

4.2 Oscillating Compressor Cascade

The linear oscillating compressor cascade features eleven blades. A close-up view of the test section is displayed in figure 4.2. The cascade parameters are outlined in table 4.2 and illustrated in figure 4.3. The airfoil represents a profile of the NACA-65-Series with a circular arc camber of 10 degrees and a thickness of 6 percent. The blades with indexes 0 and 10 are fixed rigidly at the sidewall, the remaining ones are suspended elastically. The blades are manufactured from carbon fibers to make them lighter and more prone to flutter compared to steel or aluminum blades.

The elastic suspension allows free and controlled flutter tests. With the suspension the classical aeroelastic typical section model can be realized, allowing a pitching and a plunging mode as degrees of freedom. The free

Table 4.2: Cascade parameters.

Profile	-	NACA-65-series
Chord	c	150 mm
Span	s	197 mm
Pitch	tp	112.5 mm
Pitch-to-chord ratio	tp/c	0.75
Stagger angle	γ	43 degrees at $\alpha_0 = 2$ degrees
Mean angle of attack	α_0	0...6 degrees
Pitching amplitude	$\hat{\alpha}$	± 4 degrees (max.)
Plunging amplitude	\hat{h}	± 4 mm (max.)
Oscillation frequency	f	30 Hz (max.)

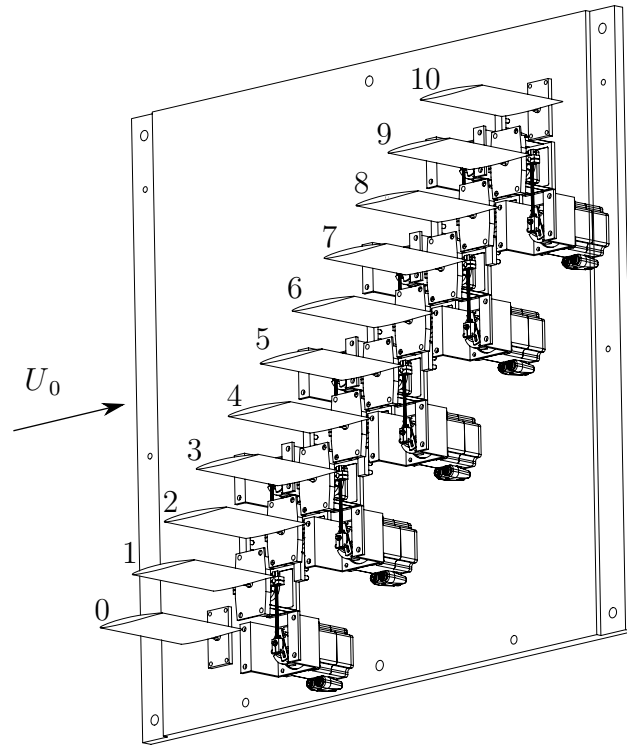


Figure 4.2: Outline of the measurement section.

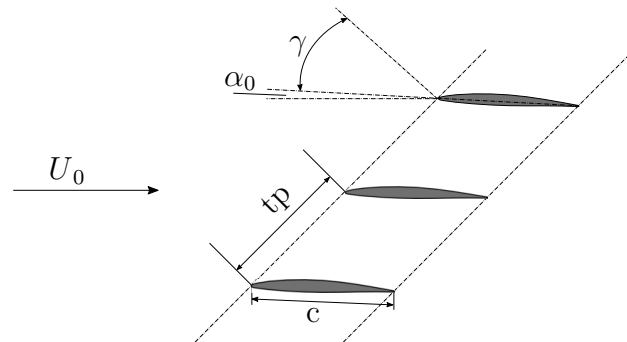


Figure 4.3: Cascade geometrical parameters.

flutter configuration is depicted in figure 4.4 (a) and the set-up for controlled flutter tests is shown in figure 4.4 (b). A close-up view of the degrees of freedom is shown in figure 4.5. From the latter figure, it can be observed that the plunging motion is carried out parallel to the mounting plate. The suspension is manufactured mainly from leaf springs in different widths and milling parts. For the pitching motion, six leaf springs are electro-welded to the support ring, rotary disk and plunging plate. Six leaf springs are also used for the plunging mode that are electro-welded to the support frame, the plunging and mounting plate, see figure 4.5. The elasticity of the suspension

is given by the leaf springs, functioning as two-sided fixed bending springs. The blade is clamped to the suspension with a tapered steel connection at mid-chord. Thus, the center of rotation is at mid-chord. The structural properties of the system, namely the suspension including blade, were determined by Hennings, see e.g. Ref. [5]. Due to the suspension design, each blade section undergoes the same motion without spanwise components. The suspension is installed via the mounting plate to the back sidewall outside the test section. Each degree of freedom can be controlled individually. For the free flutter set-up, the blades can vibrate in a single mode, or both modes can be allowed. Further, this set-up can be frequency tuned by adding two balancing masses to each suspension. The actual blade suspension hardware, in free flutter configuration, is shown in figure 4.6.

For the present work, each of the nine suspensions is equipped with an individual stepper motor (Nanotec PD6-N8918S6404-S), see figure 4.2 and 4.4 (b). The stepper motors have a built-in closed-loop control system to ensure a constant reduced frequency during wind tunnel operation. Beside the stepper motor, the oscillatory drive system includes a crank gear mechanism. A crank shaft is connected to the suspension, driven by the stepper motor. Thus a sinusoidal blade pitching or plunging motion can be realized. The oscillation amplitude is set by the excenter of the crank mechanism and the blades can oscillate up to a frequency of $f = 30$ Hz. Each stepper motor can be controlled separately. The control software of the motors is written such, that all blades oscillate at the same frequency but at a constant IBPA, allowing traveling wave mode tests. For this purpose a control program in CSharp was developed. Further, a controller area network (CAN bus) is used to realize the synchronization of the motors. The IBPA can be regulated with an increment of 0.18 degrees for each motor.

The blade oscillation amplitude is reviewed by means of strain gauges that are placed at the leaf springs of the suspension, see figure 4.4. The blade oscillates at a frequency of $f = 9$ Hz. All mistuning cases were measured with this frequency. The raw signal, at quiescent air condition, is displayed in figure 4.7 (a) in the time domain, and the frequency spectrum is shown in figure 4.7 (b). In 4.7 (a), the blade oscillation amplitude in degrees is plotted versus the time normalized by the oscillations period. In figure 4.7 (b), the normalized magnitude is displayed against the frequency. In the frequency spectrum, a sharp peak at $f = 9$ Hz can be observed, indicating that no significant higher harmonic content is present.

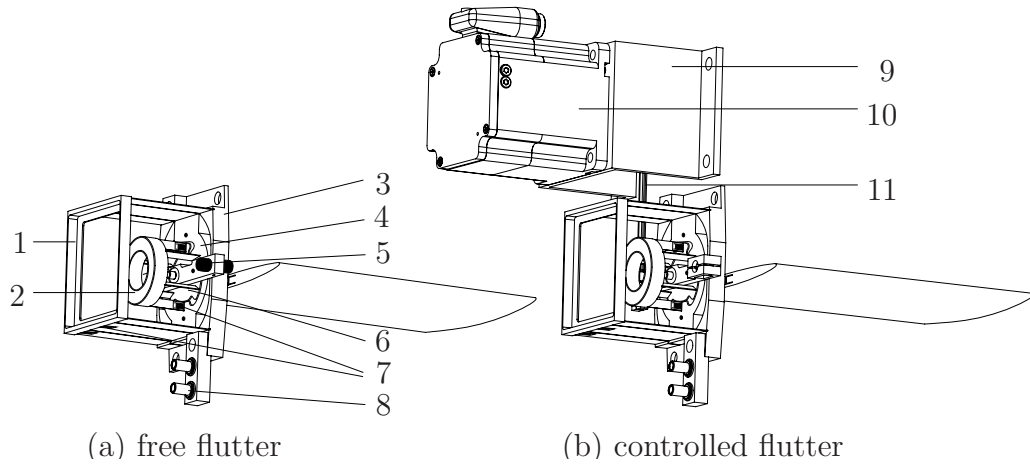


Figure 4.4: Elastic blade suspension with blade. 1 Support frame; 2 Support ring; 3 Mounting plate; 4 Plunging plate; 5 Balancing mass; 6 Rotary disk; 7 Strain gauges; 8 Lemo connector; 9 Motor support; 10 Stepper motor; 11 Crank shaft.

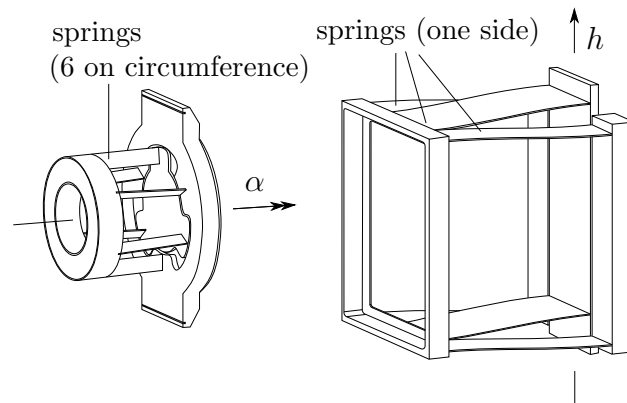
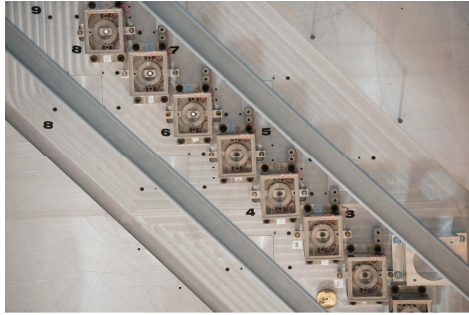
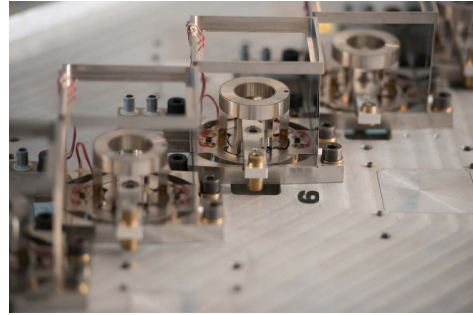


Figure 4.5: Degrees of freedom of the blade suspension (adapted from Ref.[5]).

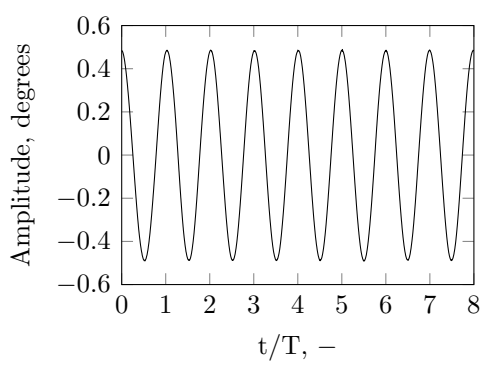


(a) Blade suspensions at the test facility sidewall (back view).

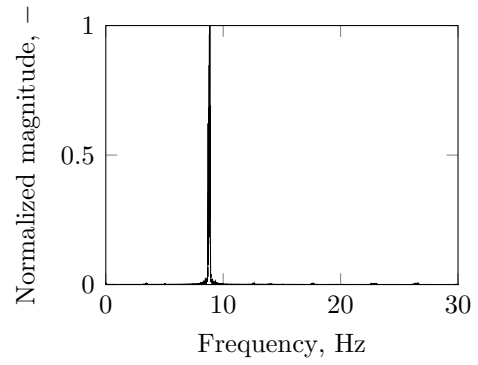


(b) Close-up view of the suspensions.

Figure 4.6: Pictures of the blade suspensions in the free flutter configuration (without measurement equipment).



(a) Time domain.



(b) Frequency domain.

Figure 4.7: Strain gauge signal of cascade central suspension; blade oscillates at 9 Hz in pitch in quiescent air.

4.3 Measurement Setup

The test facility is equipped with steady and unsteady measurement devices.

To monitor the wind tunnel parameters such as temperature, static, dynamic and absolute pressure, several sensors are used. In the settling chamber temperature is measured with a Pt100 resistance thermometer and the absolute pressure with a sensor ¹ for barometric pressure measurements. In the test section, the dynamic pressure is measured with a Prandtl tube in combination with a differential pressure sensor ², from which velocity is computed. The static pressure in the inlet section is measured as well with a differential sensor³. The pressure taps and the traverse mechanism in the inlet section are located at a distance of eight times the chord length upstream of the central cascade blade.

For the determination of the base flow condition, the longitudinal velocity component u of the inflow in the measurement section was acquired by hot-wire anemometry. The steady and unsteady blade surface pressures were measured with 20 recessed mounted sensors per measurement blade. Blade vibrations amplitude and frequency were acquired with means of strain gauges. To verify the assumed 2D flow topology on the blade surface, oil flow visualization was applied at different Reynolds numbers.

4.3.1 Surface Oil Flow Visualization Technique

To provide an indication of the flow structure on the blade surface, the oil flow visualization technique was used. For this technique, an oil mixture, consisting of paraffin oil and color pigments, is sprayed on the blade in the wind tunnel. Streak lines formations can be made visible because the shear force is working on discrete oil dots. With these surface streak lines, complex flow features close to the surface, such as flow separation and reattachment, can be revealed [67].

The general procedure of oil flow visualization is as following: i) preparation of oil flow mixture, ii) spraying of the oil blend on the component(s) in the wind tunnel, iii) installation of the component(s) in the wind tunnel (if not yet fixed), iv) wind tunnel operation, an air flow passes the component(s), v) dehydration of the surface oil film on the component(s). The last step is to take pictures of the parts, for blades the pictures are usually shot normal to the blade chord. Commonly, a high resolution digital camera is used for this purpose. For the application in the present thesis, pressure and suction side

¹Setra Model 270, pressure range: 80000 - 110000 Pa

²KAL 84 halstrup-walcher GmbH, pressure range: 0 - 1000 Pa

³Setra Model 264, pressure range: ± 500 Pa

were sprayed with an oil mixture, containing yellow color pigments.

4.3.2 Hot-wire Anemometry

For the hot-wire measurements, an one-wire probe was used together with a TSI Ifa-300 (Typ 1210 - 20) hot-wire anemometer. It is a widely used measurement method for the determination of flow velocities in low and high speed flows due to its high frequency-response and temporal resolution when compared to other measurement techniques [68]. Therefore, it is employed especially for the investigation of boundary layer flow and detailed investigation of turbulent flows [69].

The underlying measuring concept of hot-wire anemometers is convective heat transfer from a heated wire exposed to a fluid flow [68]. The sensors are thin metal wires, soldered to prongs. Tungsten, platinum or platinum alloys are used as wire material. The wire diameter ranges from 1 to 10 μm and the length from 0.5 to 2 mm [70]. The wire is heated by an electric current to a much higher temperature than the flow and cooled when a fluid passes the wire. Depending on the flow regime, heat losses in the wire occur due to convection, conduction and radiation. A heat balance of the electrically heated and convective cooled wire is used to relate the flow velocity and electric heating voltage. The assumptions for the application of this technique are that radiation and conduction to wire support are small, the temperature distribution over the wire is uniform, the velocity impinges normally on the wire, fluid temperature and density are constant [69].

In the following section, the summary of the governing equations and measurement setup description is based on the work of Nitsche [69] and Bruun [68]. The heat balance is expressed by the equation

$$C_w \frac{dT_w}{dt} = W - H. \quad (4.1)$$

$C_w \frac{dT_w}{dt}$ is the stored (remaining) thermal energy in the wire, H the heat transferred to surroundings and W the power generated by Joule heating. The wire temperature is changing with time $\frac{dT_w}{dt}$ when W and H are unbalanced. The wire temperature can be approximated to behave linearly with the resistance R_w . Thus R_w is a function of the temperature

$$R_w = R_{Ref}[1 + a(T_w - T_{Ref})], \quad (4.2)$$

where a is the thermal coefficient of the wire and R_{Ref} , the wire resistance at reference temperature T_{Ref} . To realize a measurement set-up, one approach

is to control R_w so that it is constant. This concept is known commonly as "Constant Temperature Anemometry (CTA)", since T_w stays constant as well, due to its relation to R_w . The measurement formation includes conventionally beside the hot wire anemometers a Wheatstone bridge. A simplified constant temperature circuit is displayed in figure 4.8. R1 and R2 are fixed resistors whereas R3 is a variable resistor. The voltage difference between point D and B is zero if the following condition is true: $R1/R_w = R2/R3$. If the resistance of the wire changes e.g, due to an air flow passing the wire, R3 is adjusted by an amplifier with a feedback control loop, to keep the wire temperature constant. The bridge voltage is linked linearly to the hot wire voltage [69]. Therefore, with the measured change of bridge voltage V_B , the flow velocity over the wire can be computed [68].

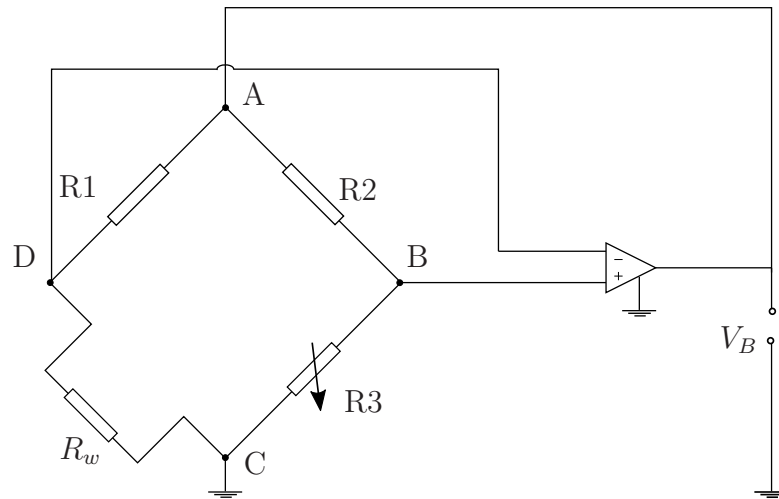


Figure 4.8: Constant Temperature Circuit Diagram, adapted from Ref. [69].

4.3.3 Strain Gauges

A strain gauge is a sensor used for surface strain measurements. It is glued rigidly to the object's surface. As the object is stretched, the electrical resistance of the sensor changes. Commonly, a Wheatstone bridge is applied to measure the variation of the voltage due to a resistance change which is proportional to the amount of stretching.

Strain gauges work uniaxial, thus one gauge measures strain only in one direction. In figure 4.9, a simplified scheme of a foil strain gauge is displayed, applied for measurements in horizontal direction. The major components of an individual gauge are a grid, a solder tabs and a carrier. The grid consists of a sequential wire filament which resistance changes when the gauge experiences

a stretch. Nowadays, foil strain gauges are used as standard sensors. They are very thin, about $40\ \mu\text{m}$, and can be manufactured in great quantities by etching or cutting almost any specific grid pattern into a metal foil sheet of a suitable alloy [71, 72]. The active length is between 0.2...150 mm and the nominal resistance, being independent of the active grid length, lies in the range from $100\ \Omega$ to $1000\ \Omega$ [71]. For electrically conductive materials, a

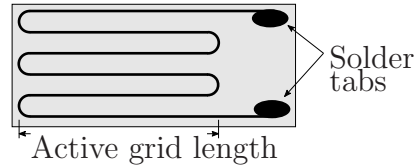


Figure 4.9: Foil strain gauge, adapted from Ref. [71].

strain sensitivity factor, describing the relative change in electrical resistance of a conductor to its relative variation in length, can be represented as

$$GF = \frac{\Delta R/R_0}{\Delta L/L_0} = \frac{\Delta R/R_0}{\epsilon}, \quad (4.3)$$

where R_0 is the unstrained conductor resistance, ΔR the resistance variation, L_0 the initial conductor length and ΔL the length variation, see e.g. [72]. $\Delta L/L_0$ is Cauchy or engineering strain, ϵ . This ratio is termed also Gauge factor. The electrical resistance of a conductor, a very thin wire in terms of a strain gauge, is related to its length, L , and area A , by

$$R = \frac{rL}{A}, \quad (4.4)$$

[71]. This definition holds for a uniform cross section. r is a property of the conductor material and named resistivity constant. If the wire is stretched elastically, the wire cross section A is reduced according to the Poisson effect and thus the resistance is increased. Similarly, if the wire is compressed the resistance is reduced. With an electric circuit, the resistance changes can be measured as voltage variation and used to compute the present strain.

As explained in detail in Ref. [73], Wheatstone bridge circuits are used commonly to relate the variation of bridge voltage to a strain level. This circuit consists of four resistances. Three basic configurations exist, namely quarter-bridge, half-bridge and full-bridge circuit. The names indicate how many gauges themselves are one of the four circuit resistances. If the resistor is not a gauge then they are fixed resistors incorporated in the instrumentation. In figure 4.10, a basic bridge strain circuit is shown for strain gauges measurements. The set-up is designed so that the bridge is balanced when

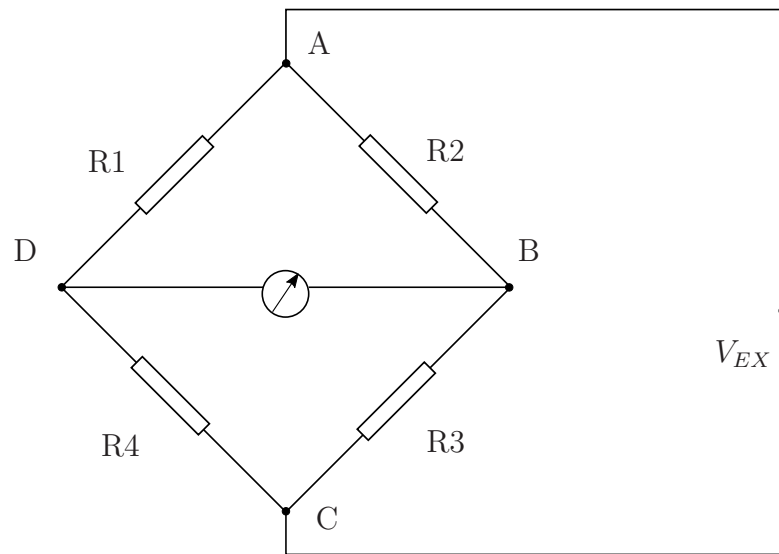


Figure 4.10: Wheatstone bridge circuit, adapted from Ref. [73].

the strain gauge are unstrained, thus the voltmeter between point D and B registers zero volts. If a force is applied to a gauge, the bridge will become unbalanced and the voltage changes are measurable, being proportional to the strain applied to the gauge. This relationship holds true only for the range of material elasticity. Full-bridge configurations are the most sensitive, accounting for temperature compensation of the bridge circuit. Thus, if four strain gauges are bonded on the same specimen in a full-bridge circuit and temperature changes, the four resistances will vary by the same percentage and the bridge balance will stay unaltered.

The blade oscillation and frequency is measured by means of strain gauges, located on the leaf springs. Each suspension is equipped with eight strain gauges, four for each degree of freedom to form a full Wheatstone bridge that fully compensates temperature drift.

4.3.4 Blade Surface Pressure Measurements

To acquire the steady and unsteady blade surface pressure, measurement blades were developed, designed and manufactured. The blades are designed in a way that ten pressure taps are located on the pressure (PS) and suction side (SS), respectively. The taps on each side have been drilled with an angle of 15 degrees to the blade's chord to minimize the influence of the taps among themselves. A scheme of the taps distribution is depicted in figure 4.11. The tap positions are displayed in table 4.3 and a complementary sketch to the table in figure 4.12. On the pressure and suction side, the taps

have the same axial locations. The pressure is acquired with 20 Endevco 8510B -1 sensors, featuring a pressure range of 0, ..., 1 PSI corresponding to 0, ..., 6895 Pa. Inside the blade, each tap is connected to a steel tube, outside the measurement blade the pressure is guided with a silicon tube to the sensor. The sensors are recessed mounted at the back of the test section wall. The diameter of the pressure taps is 0.5 mm as well as for the tubes. Each of the 20 tubes system has an individual length, but in average the length of the steel tube is 0.1 m and 0.4 m for the silicon tube.

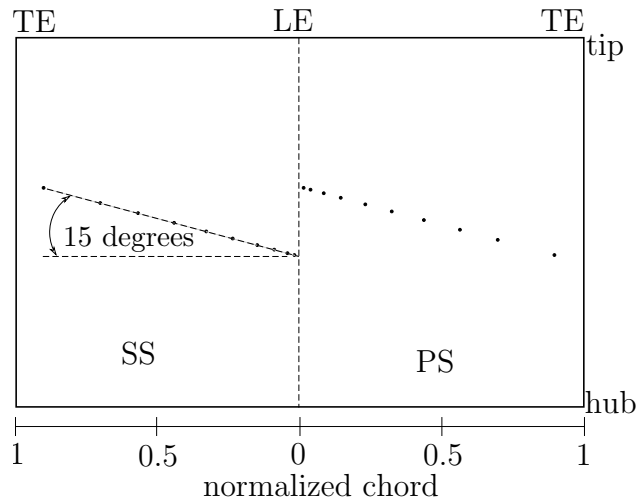


Figure 4.11: Pressure tap distribution on the blade surface.

x/c
0.0157
0.0400
0.0867
0.1467
0.2333
0.3267
0.4400
0.5667
0.7000
0.9000

Table 4.3: Pressure tap locations.

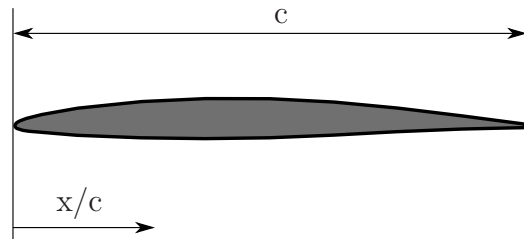


Figure 4.12: Profile geometry.

To reconstruct the pressure at the tap location, each tube system was calibrated dynamically to account for the time shift of the pressure signal between tap and measurement location as well as for the damping characteristic in

pressure amplitude. The calibration was conducted in a calibration chamber, which is operated by the Institute of Aerodynamics of the German Aerospace Center in Göttingen, e.g. Ref. [74]. The technical details can also be looked up under the patent *DE102005047623*. For the present work, the tube systems are calibrated for a frequency range of 1, ..., 120 Hz. A sinusoidal pressure signal with an amplitude of $a_0 = 250$ Pa was applied to each of the twenty tube system for one measurement blade. A characteristic calibration curve for one tube system is depicted in figure 4.13. In the present experimental investigations, a frequency range of 5, ..., 9 Hz is applied, therefore the amplitude is not significantly damped by the tubing system, see figure 4.13. The time lag between measurement and pressure tap location on the blade surface increases considerably with higher frequencies and has to be accounted for in the data post processing. The steady calibration of the pressure sensors is performed before each measurement campaign with three different pressure sensors. Pressure sensors of type Setra 264 with pressure ranges of 0, ..., 25 Pa and 0, ..., 100 Pa are used as well as a calibration system, namely KAL 84 halstrup-walcher, with a pressure range of 0, ..., 1000 Pa.

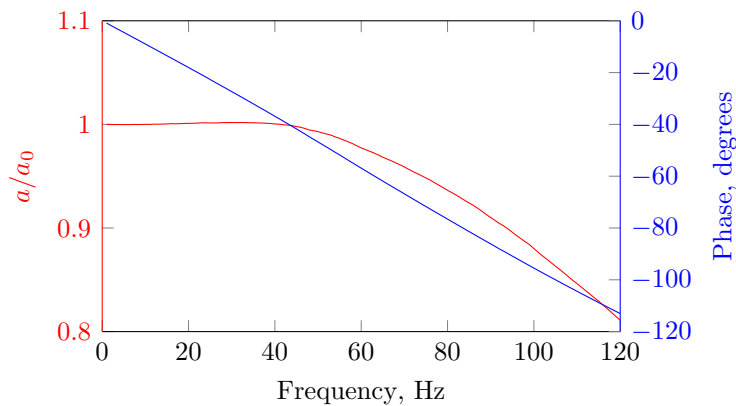


Figure 4.13: Characteristic calibration curves of a tube system in a measurement blade for the first pressure tap location counting from the leading edge on the suction side.

4.3.5 Data Acquisition

All measurement signals were acquired as time-varying voltage and sampled at time-wise equidistantly distributed sampling points. Then, they were quantized with an analog-to-digital converter. After the quantization, each sample was related via a calibration function to a physical quantity.

Hot wire measurement chain

In figure 4.14, the measurement set-up for the hot wire measurements is depicted. The hot wire sensor is connected to the constant temperature anemometer (ifa-300). Then, the relative change in voltage of the measuring bridge of the hot wire system is converted from an analogue to a digital signal to make it processable at the computer. A 16-bit National Instruments-PCI 6229 board is used for this purpose. The IFA and the traverse mechanism are controlled with an in-house software, written with the software MATLAB®. A Prandtl tube, in combination with a pressure sensor, is used to calibrate the hot wire sensor, linking the dynamic pressure of the tube set-up to the bridge voltage, from which flow velocity can be computed. The sensor and the Prandtl tube were placed in the inlet section in the mean flow field, but positioned in a way that they could not influence each other. The dynamic pressure was measured with a KAL 84 halstrup-walcher system with a pressure range of 0, ..., 1000 Pa.

Measurement chain for blade surface pressure and strain gauge measurements

The measurement chain of the blade surface pressure and strain measurements for a sinusoidal blade pitching motion is shown in figure 4.15. The aforementioned figure shows only four of twenty pressure taps for a clearer illustration of the set-up. The silicon tubes are connected to a transducer array, where the transducers are screwed in an aluminum block and connected to the data acquisition system. For the measurements two commercial data acquisition systems, namely DEWE-50-PCI with 32 channels each, were cascaded and used to acquire the analogue signal of the pressure transducers, strain gauges and sensors to monitor wind tunnel parameters. This system includes an analogue-digital-converter, an ORION-1624-200 board with a 24-bit resolution. 18 bits are considered to be effective. The smallest processable input voltage to the acquisition system is $\pm 500 \mu\text{V}$.

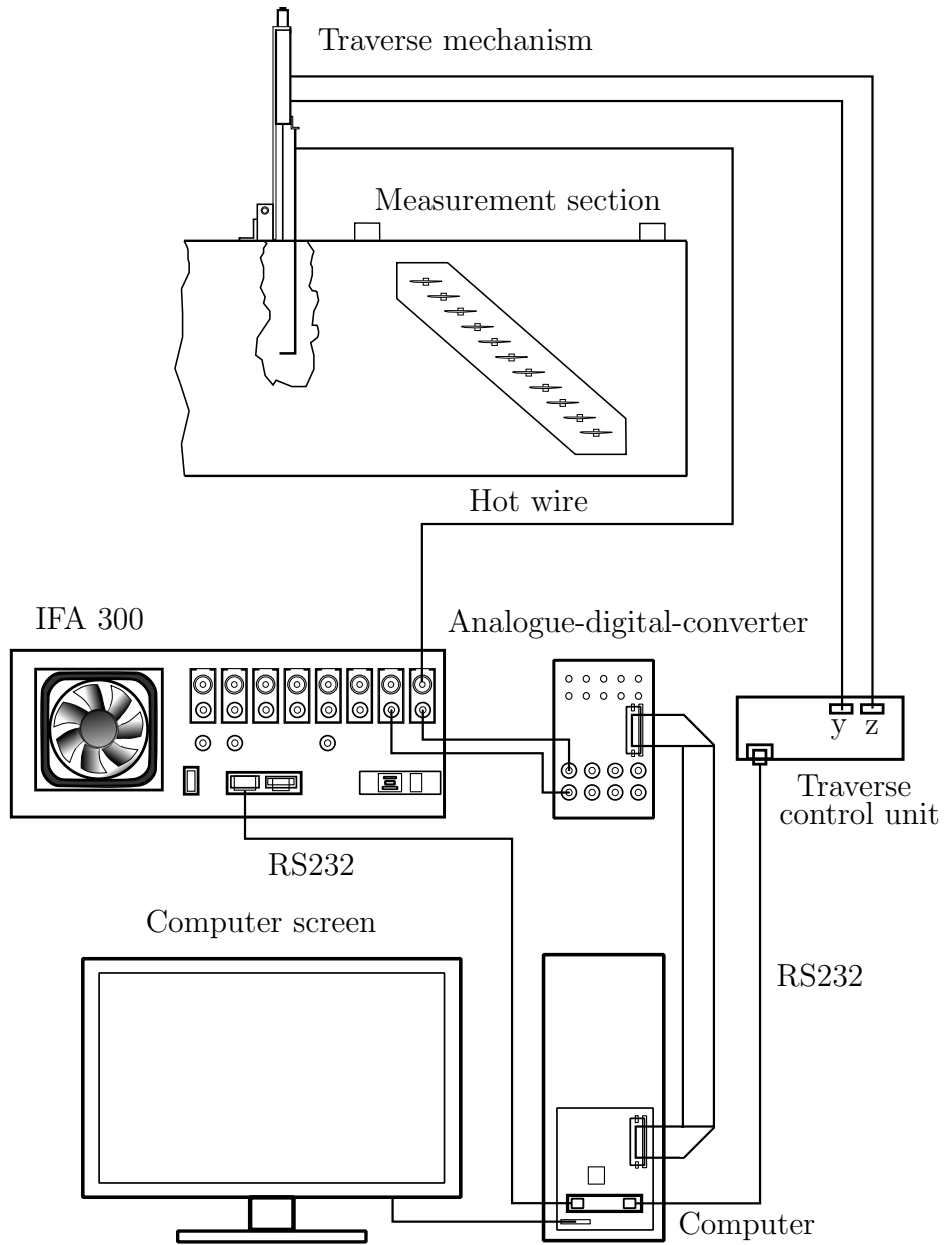


Figure 4.14: Hot wire measurement chain.

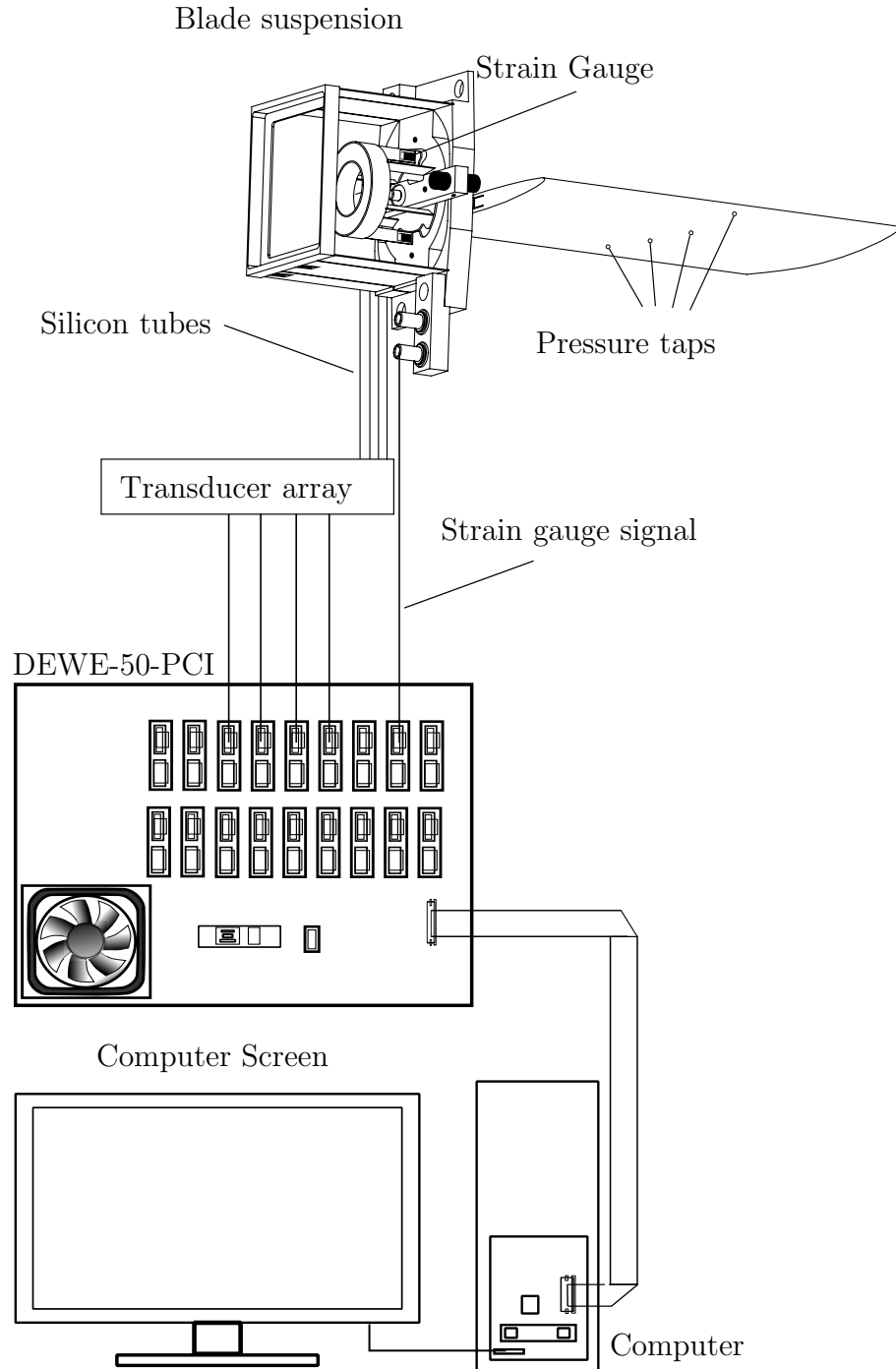


Figure 4.15: Blade surface pressure and strain gauge measurement chain.

Chapter 5

Data Reduction Procedure

In this chapter, the statistical parameters that have been applied to the measurement data are presented. Depending on the choice of measurement technique and testing strategy, different averaging techniques are needed. Three different formations of the mean were used, namely the mean, an ensemble averaging technique and the Root-Mean-Square. Further, the aerodynamic coefficients and damping parameter that were used to investigate the underlying physics of the flutter phenomena are summarized. The software MATLAB[®] was used for the data reduction process.

5.1 Statistical Parameters

Mean

In statistics, the mean is often used to describe the central trend of a data set, being also the first statistical moment [75]. There are various quantities termed mean and it is also called mathematical expectation or average. The unweighted mean, \bar{s} , of a data set, containing values from s_1, s_2, \dots, s_n , is defined as

$$\bar{s} = \lim_{n \rightarrow \infty} \frac{1}{n} \sum_{i=1}^n s_i, \quad (5.1)$$

where n is the total sample count of the data set [76].

Generally, a statistical presentation of a turbulent flow is based on the Reynolds averaging, see e.g. [77], decomposing the flow into a mean, $\bar{s}(t)$, and fluctuating component, $s'(t)$,

$$s(t) = \bar{s}(t) + s'(t). \quad (5.2)$$

This mathematical method allows the description of a temporal average of a statistical steady flow as:

$$\bar{s} = \bar{s}(t) = \lim_{T \rightarrow \infty} \frac{1}{T} \int_{t_0}^{t_0+T} s(t) dt \hat{=} \lim_{n \rightarrow \infty} \frac{1}{n} \sum_{i=1}^n s_i. \quad (5.3)$$

Ensemble Average

The ensemble average represents the temporal mean of each sample value, s_i , within an ensemble. According to the ergodic hypothesis, the temporal mean and the phase average are equal within an ergodic system and is,

$$\langle s \rangle = \lim_{n \rightarrow \infty} \frac{1}{n} \sum_{i=0}^n s(t + iT), \quad (5.4)$$

where n is the amount of periods and iT the instantaneous period that is used for the averaging [78]. This technique is used to analyze the quasi-periodic flow. Thus the unsteady data was phase averaged based on an ensemble average technique with respect to the oscillation period (typically 1000 periods). The non-periodic components are removed from the signal within this procedure, if a sufficient large amount of periods is considered. A time marker is needed, which is generated commonly by a trigger signal. For the unsteady surface blade pressure, the strain gauge signal is used for this purpose.

Standard Deviation

In fluid dynamics, the sample standard deviation is used to characterize the amount of fluctuation in a data set, e.g. to compute the turbulence intensity [79]. According to statistical theory, see e.g. [75], the Root-Mean-Square (RMS) is defined as

$$s'_{rms} = \sqrt{\frac{1}{n} \sum_{i=1}^n (s_i - \bar{s})^2}. \quad (5.5)$$

5.2 Aerodynamic Coefficients

In the following, the steady and unsteady pressure coefficient are presented for an airfoil section. For the derivation of unsteady quantities simple harmonic motion in a single-degree-of-freedom of an airfoil section is assumed.

Steady Pressure Coefficient

The pressure measurements were reduced to a steady pressure coefficient, yielding

$$cp_0(x) = \frac{p(x) - p_\infty}{q}, \quad (5.6)$$

where $p(x)$ is the static pressure at a specific location on the blade surface, p_∞ the static pressure in the inlet and q the upstream dynamic pressure.

Unsteady Pressure Coefficient

The post-processing of the unsteady data is based on the fundamental work of Carta, a detailed description is given in Refs. [48, 33]. All unsteady pressure data are normalized with regard to the blade pitching amplitude $\hat{\alpha}$ (in rad) and the dynamic pressure q , as follows

$$cp(x, t) = \frac{p(x, t)}{\hat{\alpha}q}. \quad (5.7)$$

The unsteady pressure coefficient can be presented in component or according to Euler's formula in a complex exponential form, yielding

$$cp(x, t) = \hat{c}p(x)e^{i(\omega t + \phi(x))} \quad (5.8)$$

$$= (\Re(cp(x)) + i\Im(cp(x)))e^{i(\omega t)}, \quad (5.9)$$

where $\hat{c}p(x)$ is the amplitude, ω the angular frequency and $\phi(x)$ the phase angle relative to the blade motion.

The unsteady pressure difference coefficient is computed from the difference between the surface pressure of the blade pressure and suction side, given by

$$\Delta cp(x, t) = cp_P(x, t) - cp_S(x, t) \quad (5.10)$$

$$= (\Re(\Delta cp(x)) + i\Im(\Delta cp(x)))e^{i(\omega t)}. \quad (5.11)$$

The subscripts P and S denote pressure and suction side, respectively. $\Im(\Delta cp(x))$ is obtained by

$$\Im(\Delta cp(x)) = \Im(cp_P(x)) - \Im(cp_S(x)). \quad (5.12)$$

This computation can be carried out analogously for $\Re(\Delta cp(x))$.

Unsteady Moment Coefficient

The definition of the unsteady pitching moment coefficient is

$$C_m(t) = \int_0^1 (x_C - x)\Delta cp(x, t)dx, \quad (5.13)$$

where x_C designates the location of the center of rotation. In the present context, $C_m(t)$ was calculated with respect to the blade mid-chord; x_C and x were normalized with the blade chord.

5.3 Aerodynamic Damping Parameter

System stability can be assessed by evaluating the normalized aerodynamic work per oscillation cycle, see subsection 2.1.2.

Carta [33] defined an aerodynamic damping parameter, assuming small blade oscillation amplitudes and simple harmonic pitching motion of a two-dimensional airfoil section in a single-degree-of-freedom system,

$$\alpha(t) = \hat{\alpha}e^{i\omega t}. \quad (5.14)$$

By the application of elementary theory, see Ref. [80], he introduced the aerodynamic damping parameter as

$$\Xi(\sigma) = -\hat{C}_{m1}\sin\theta_1. \quad (5.15)$$

Here, θ_1 is the phase angle between the first harmonic of the unsteady moment coefficient and the blade displacement. The angle is defined positive when the moment is leading the blade motion. Thus, the convention is that when Ξ is negative, the system is unstable. The aerodynamic damping parameter is also derived in a more general form in subsection 2.1.2.

Chapter 6

Experimental Investigation

In the following chapter, the experimental investigations are presented that were carried out to meet the objectives, outlined in chapter 3. First, the testing approach is discussed, then the results are presented. They are structured in three main parts: i) base flow assessment (section 6.2); ii) unsteady performance and stability assessment of the oscillating cascade (section 6.3); iii) investigation of an aerodynamically mistuned oscillating compressor cascade (section 6.4). In total, 96 (12x8) experimental test cases were investigated in part ii) and iii).

6.1 Testing Strategy

After the commissioning of the test rig, hot wire measurements for different Reynolds and Mach numbers were carried out to assess the quality of the inlet base flow. The base flow assessment includes steady cp_0 distributions at various blade positions in the cascade, to examine the flow periodicity. Further, the steady state data are helpful to understand the unsteady response, as regions with high pressure magnitudes are expected to exhibit a similar behavior when the airfoil oscillates. Oil flow visualization was performed to study the flow topology on the blade surfaces.

A traveling wave set-up is used in this work. At quiescent air condition, the blade oscillation amplitude and frequency were measured by means of strain gauge measurements, to check if any significant higher harmonic frequency content is present. The unsteady performance of the test rig was validated by comparing the measurements to data from literature. This has been carried out for a range of IBPAs of $\sigma = -180 : 45 : 180$ degrees, at one reduced frequency.

Further, detailed unsteady data at different chordwise positions are presented, to discuss how stability is assessed and how the aerodynamic damping

parameter is computed within the present work.

The amount of detuning is in the same order of magnitude as presented in a numerical study and reported to affect aeroelastic stability, see Ref. [25]. The aerodynamic mistuning was introduced by blade-to-blade stagger angle variations and consist of two investigation clusters.

The dataset referred to as cluster I includes five different mistuning configurations, investigating stagger angle variations of $\gamma = \pm 1$ degrees and $\gamma = \pm 2$ degrees, see table 6.1. Configuration I and II are referred to as one-blade mis-staggering pattern, whereby the stagger angle of the central blade was altered by $\gamma = \pm 2$ degrees. A positive stagger angle variation is defined as nose-up, vice versa for a negative variation. Configurations III and IV study the affect of an alternating stagger angle variation on stability in the range of $\gamma = \pm 2$ degrees. For configuration III, a positive stagger angle variation was imposed to every second blade, and for configuration IV a negative one. Configuration V is called random mis-staggering. Random indicates that the pattern features stagger angle variations of $\gamma = \pm 1$ degrees and $\gamma = \pm 2$ degrees which have been distributed arbitrarily.

Cluster II focuses on the effect of the same stagger angle variation for all blades in the cascade within one configuration. Configurations VI to X investigate negative stagger angle variations in the range of $\gamma = -1 : 1 : -5$ degrees. For this configurations, the stagger angle of all blades within the cascade was changed simultaneously.

For the experimental investigations presented hereinafter, a mean angle of attack of $\alpha_0 = 2$ degrees is associated with the baseline configuration. All experiments were carried out with an oscillation amplitude of $\hat{\alpha} = 0.5$ degrees. The parameters were chosen to be consistent with works of Sachs [7] and Carta [33] that have been used also to validate the unsteady performance of the test rig.

Table 6.1: Test matrix (cluster I and II) for a blade in sinusoidal motion with an oscillation amplitude of $\hat{\alpha} = 0.5$ and a reduced frequency of $k = 0.244$.

		blade number								
Configuration		1	2	3	4	5	6	7	8	9
Cluster I, $\Delta\gamma$, deg.	I	-	-	-	-	+2	-	-	-	-
	II	-	-	-	-	-2	-	-	-	-
	III	+2	-	+2	-	+2	-	+2	-	+2
	IV	-2	-	-2	-	-2	-	-2	-	-2
	V	+2	-	-1	+1	+2	-2	+1	-	+2
Cluster II, $\Delta\gamma$, deg.	VI	-1	-1	-1	-1	-1	-1	-1	-1	-1
	VII	-2	-2	-2	-2	-2	-2	-2	-2	-2
	VIII	-3	-3	-3	-3	-3	-3	-3	-3	-3
	IX	-4	-4	-4	-4	-4	-4	-4	-4	-4
	X	-5	-5	-5	-5	-5	-5	-5	-5	-5

6.2 Base Flow

The hot wire results, including velocity profiles and turbulence intensity in the inlet section, are presented hereinafter. The data were acquired with a biaxial traverse mechanism, for the set-up see again figure 4.1. The measurement consists of 555 points and is displayed in figure 6.1. The investigated parameters of the hot wire campaign are summarized in table 6.2.

In figure 6.2, velocity profiles in the inlet section are depicted alongside the z -axis (parallel to the inlet section and perpendicular to the main flow) for five different Reynolds numbers. In each subfigure, three profiles normalized by the mean inlet velocity (outside boundary layers) \bar{U}_0 , are featured, covering the pressure tap locations of the measurement blades. The location $y = 0$ mm corresponds to blade midspan, whereas $y = -50$ mm and $y = 50$ mm are minimum and maximum span positions of the pressure tap distribution on the blade surface. All velocity profiles follow similar trends, characterized by a bump between $z = -400$ mm and $z = 0$ mm. The discrepancy from the mean inlet velocity is decreasing when moving towards positive value of z . The maximum deviation is detected for the smallest Reynolds number, namely $Re = 140000$, and is 3.3% at $y = 50$ mm. For the remaining studied Reynolds numbers, the maximum deviation is below 3%. The minimum value is obtained for $Re = 350000$ being slightly below 1.5%. These deviations are regarded as acceptable and in line with other test rigs. In Ref. [81],

Hernández et al. state generally that for most applications a flow turbulence and non-uniformities level of up to 2% is acceptable. It holds true for the current test facility disregarding the deviations at the bump position. Having a similar flow regime as the current test rig, the NASA Lewis Research Center 9-by-15 feet low speed wind tunnel features spanwise Mach number variations in the order of 1% [82].

The observed bump results from the non-uniform outlet velocity profile from the blower. A conventional blower outlet velocity profile has a S-shape, featuring maximum velocity e.g. at the top of an outlet duct and a minimum velocity at the bottom [83]. To increase flow uniformity a long straight duct can be placed after the blower outlet. For the current test rig, there was not enough space available to install a long duct. Therefore, meshes were placed in the diffuser inlet, middle and outlet sections in order to improve the inlet flow quality.

In figure 6.3, the root mean square (RMS) of the fluctuating velocity u' is displayed at three y locations, which are the same as in figure 6.2. Each subfigure presents the turbulence intensity for different Reynolds and Mach numbers in the inlet section. Each measurement point is normalized with the mean inlet velocity. The mean values of the turbulence profiles are summarized in table 6.2 for each investigated case. $Re = 140000$ features the highest level of turbulence, namely 0.27%. For $Re = 200000$, $Re = 250000$ and $Re = 350000$ the turbulence decreases to 0.22%, 0.21% and 0.18%, respectively. 0.18% is achieved also for a $Re = 300000$. In the NASA Lewis wind tunnel the turbulence level is below 0.4 percent for all components (axial, horizontal and vertical), see Ref. [82]. Additionally, a comprehensive overview of wind tunnel flow quality of several facilities is given in Ref. [84], in which the turbulence level is ranging from 0.007, ..., 4%. Thus, the current wind tunnel falls within a common span of turbulence intensities.

The flow topology on the central blade was studied by the visualization of shear stress lines with oil flow. It has been carried out for Reynolds numbers of $Re = 140000$ and $Re = 200000$. The mean angle of attack was set to $\alpha_0 = 2$ degrees. In figure 6.4 (a), the pressure side for the two investigated Reynolds numbers is displayed, and in figure 6.4 (b) the suction side. From the leading edge pressure side to the rear part of the blade, streak lines form that are almost parallel to each other. At the blade hub and tip the leakage flow, that restricts the blade area where a 2D flow topology can be assumed, can be clearly observed. On the suction side, a laminar boundary layer develops from the leading edge to the aft part of the blade. Before the trailing edge, a separation bubble is detected. The separation positions are illustrated with a continuous line, see figure 6.4 (b). It is also observed that

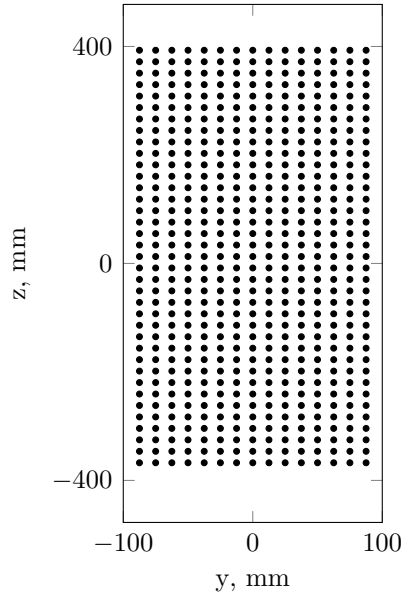


Figure 6.1: Measurement grid, for hot wire measurements, in the inlet of the test section.

the corner vortices, at the blade hub and tip, interact with the separation bubble and prevent it from moving towards the section sidewalls. To trigger the transition process and minimize the risk of flow separation, a transition strip was stuck on the blade surface, see figure 6.4 (c). With the strip, the shear lines are formed almost parallel to the main flow. All experiments were carried out with transition strips on the suction side of all eleven blades in the cascade. All strips were placed after the fourth pressure tap to minimize the influence on the pressure measurements in the leading edge region. The steady c_p distribution with strips on the suction surface, presented in figure 6.5, did not show any sign of a pressure plateau in the distribution which

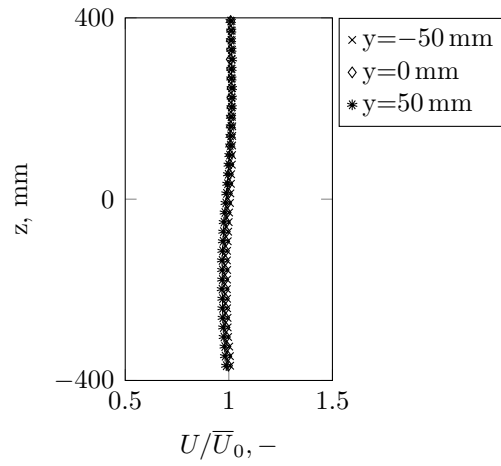
Table 6.2: Measured turbulence intensity levels at the different Mach and associated Reynolds numbers.

Mach number	Reynolds number	$T_U, \%$
0.041	140000	0.27
0.058	200000	0.22
0.073	250000	0.21
0.087	300000	0.18
0.1	350000	0.18

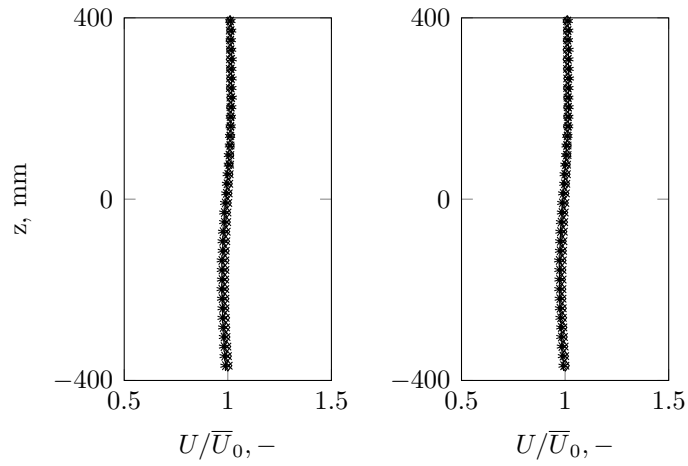
would be characteristic for a separation bubble, see e.g. Ref. [85]. Further, the acquired unsteady pressure data show a good agreement with data from literature for similar test cases, see section 6.3, and therefore the influence of the strips on the pressure data is considered to be negligible.

To prove the flow periodicity in the test section, the steady pressure coefficient, cp_0 , is plotted against the pressure tap locations for the three cascade central blades for the baseline configuration ($\alpha_0 = 2$ degrees), see figure 6.5. Positive values of x/c correspond to locations on the pressure side and negatives ones to the suction side. $x/c = 0$ refers to the leading edge and $x/c = +/- 1$ to the trailing edge. For pressure and suction side, the steady data of the three blades are found to be in good agreement.

Additionally, Malzacher et al. [86] developed an aeroelastic model to predict the flutter velocity and critical IBPA based on a typical section model. The model computed a critical interblade phase angle of $\sigma = 51.42$ degrees at a flutter onset velocity, $U_F = \frac{1}{k}$, of 0.91. In comparison, Hennings [5] reported an averaged constant interblade phase angle of $\sigma = 54$ degrees at a flutter velocity of 1.1 in a free flutter experiment. Also, chordwise pressure distributions, obtained in a traveling wave set-up, are compared with numerical data computed with the influence coefficient method for a reduced frequency of $k = 0.144$, a mean angle of $\alpha_0 = 2$ degrees and an oscillation amplitude of $\hat{\alpha} = 0.5$ degrees. The data has been found in good agreement with the experiment.

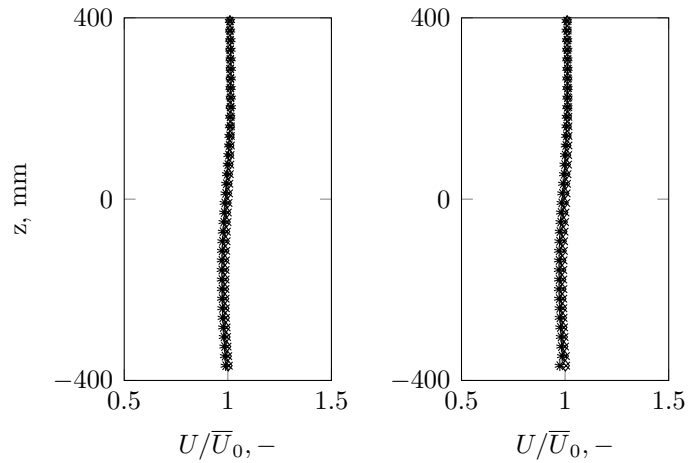


(a) Re number = 14000



(b) Re number = 200000

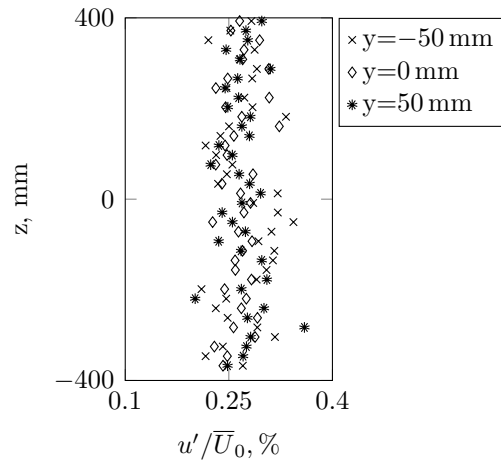
(c) Re number = 250000



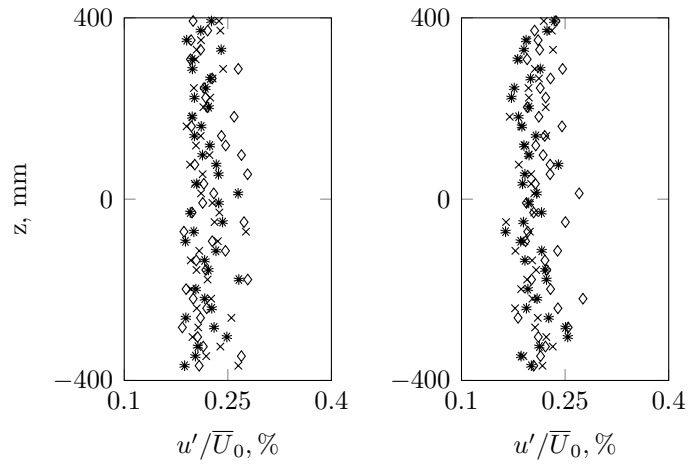
(d) Re number = 300000

(e) Re number = 350000

Figure 6.2: Normalized velocity profiles at three different y-locations for several Reynolds (Re) numbers in the inlet of the test section.

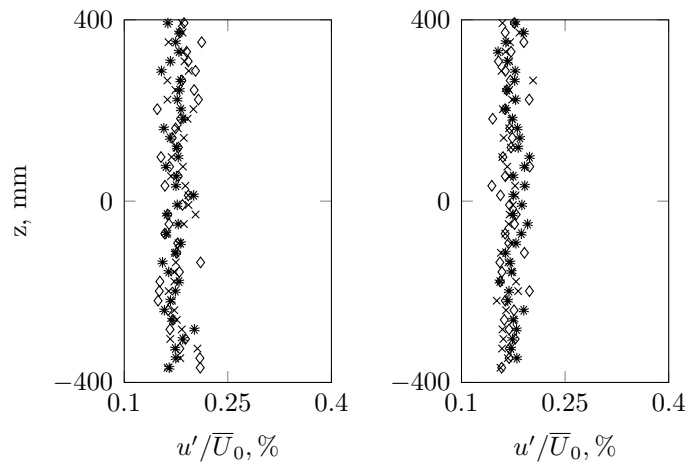


(a) Re number = 140000



(b) Re number = 200000

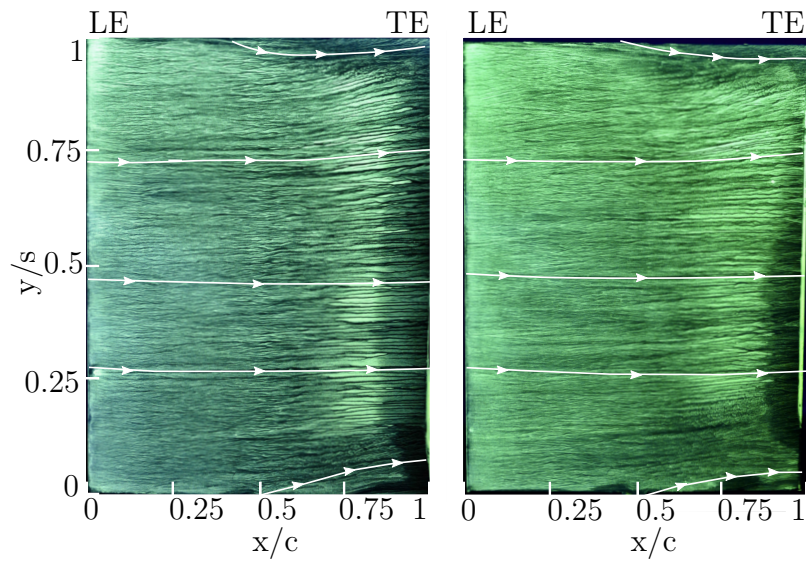
(c) Re number = 250000



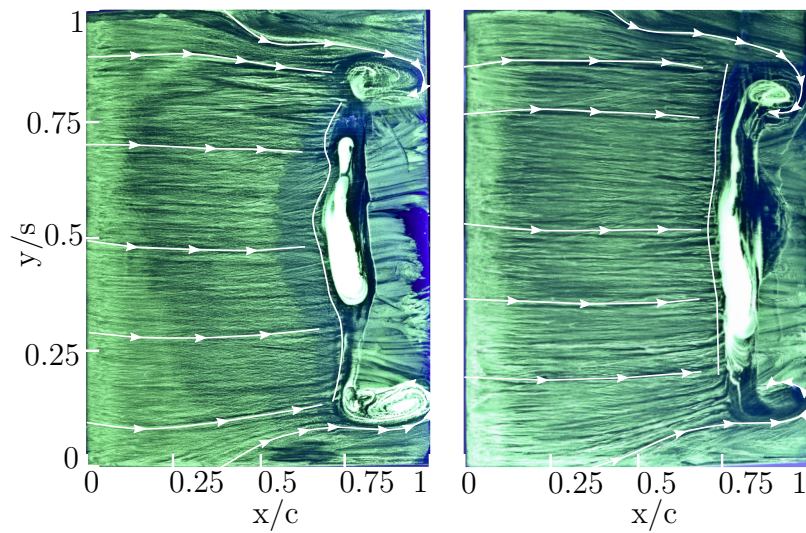
(d) Re number = 300000

(e) Re number = 350000

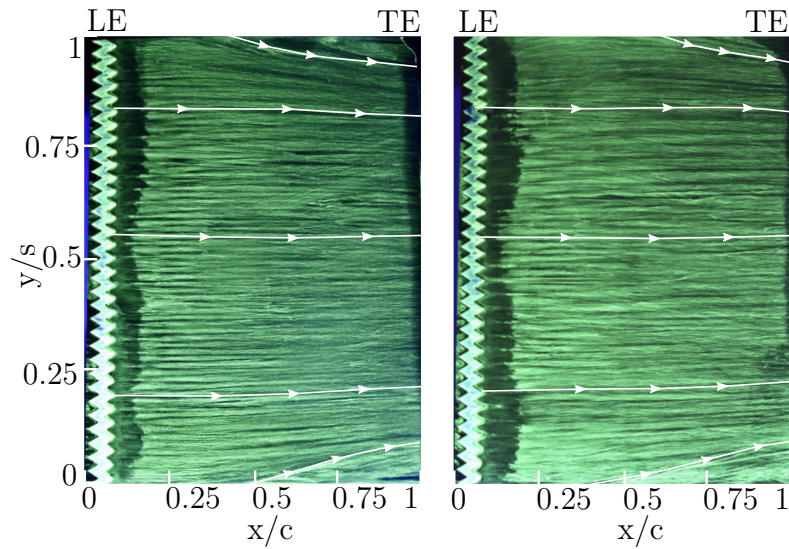
Figure 6.3: Turbulence intensity at three different y -locations for several Reynolds (Re) numbers in the inlet of the test section.



(a) Pressure side. $Re = 140000$ on the left side and for $Re = 200000$ on the right side.



(b) Suction side. $Re = 140000$ on the left side and for $Re = 200000$ on the right side.



(c) Suction side. $Re = 140000$ on the left side and for $Re = 200000$ on the right side.

Figure 6.4: Oil flow visualization for different Reynolds numbers at a mean angle of attack of $\alpha_0 = 2$ degrees.

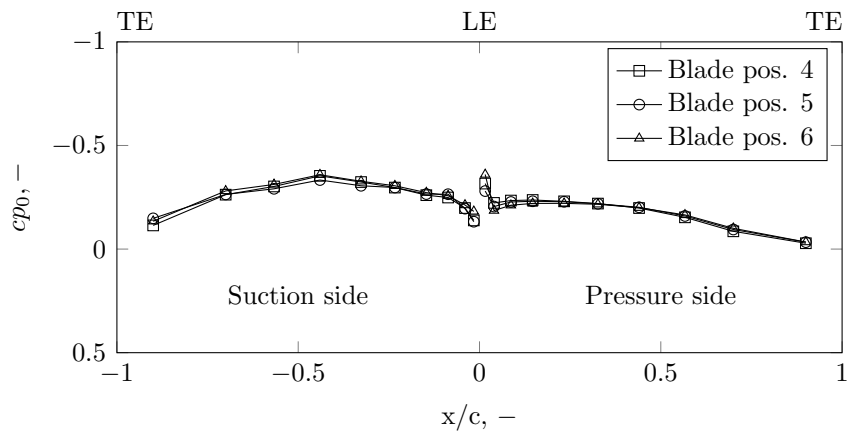


Figure 6.5: Steady pressure coefficient chordwise distribution at a mean angle of attack of $\alpha_0 = 2$ degrees.

6.3 Unsteady Performance and Stability Assessment

The unsteady performance of the test rig was checked by comparing the unsteady measurements to data of Carta [33] and Sachs [7]. They carried out experiments at a linear oscillating cascade. However, the cascade's geometrical parameters vary partially from the current set-up. A comparison of the main cascade features is given in table 6.3.

The data are presented in terms of real and imaginary parts of the unsteady pressure difference coefficient and shown in figure 6.6. The Real and imaginary parts are computed from the measured time-variant pressure and blade displacement signal. The coefficients are plotted against the normalized chord for each investigated IBPA. Eight IBPAs in the range of $\sigma = -180 : 45 : 180$ degrees, were studied, $\sigma = \pm 180$ degrees being one measurement. The convention of a positive IBPA is, that blade 9 is ahead its adjacent neighbour blade 8 and so on. The data of the cascade central blade are presented at a mean angle of attack of $\alpha_0 = 2$ degrees and a reduced frequency of $k = 0.144$ consistently with Carta and Sachs. All unsteady pressure data is referenced to the blade pitching motion. The real and imaginary part of the pressure response can be interpreted physically as the components that are in and out of phase relative to the blade motion, respectively. Thus, when the pressure is leading the blade motion and the phase is then defined positive - as it is the case for the present work - the imaginary part will be positive as well, see equation 5.9. The data display a good agreement with the measurements of Carta and Sachs, especially if taking into account the slightly different cascade geometry. The data confirm also the findings from Carta, reporting that the IBPA is one of the driving parameters regarding aeroelastic stability, see e.g. Ref. [33]. In figure 6.6, this is pinpointed by the fact, that the chordwise pressure distributions look different for each studied IBPA, attaining peak values at $\sigma = 180$ degrees and a minimum for IBPA $\sigma = 0$ degrees. An explanation is that the passage area of the cascade changes with IBPA. When the airfoils oscillate at a constant IBPA, the blade walls

Table 6.3: Comparison of cascade parameters.

	Carta	Sachs	TU Berlin
Chord, mm	152.4	150	150
Span, mm	254	200	197
Pitch, mm	114.3	115.5	112.5
Blade count	11	11	11
Side wall stagger angle (at $\alpha_0 = 0$), deg.	30	45	45
Airfoil, NACA-65-series	✓	✓	✓

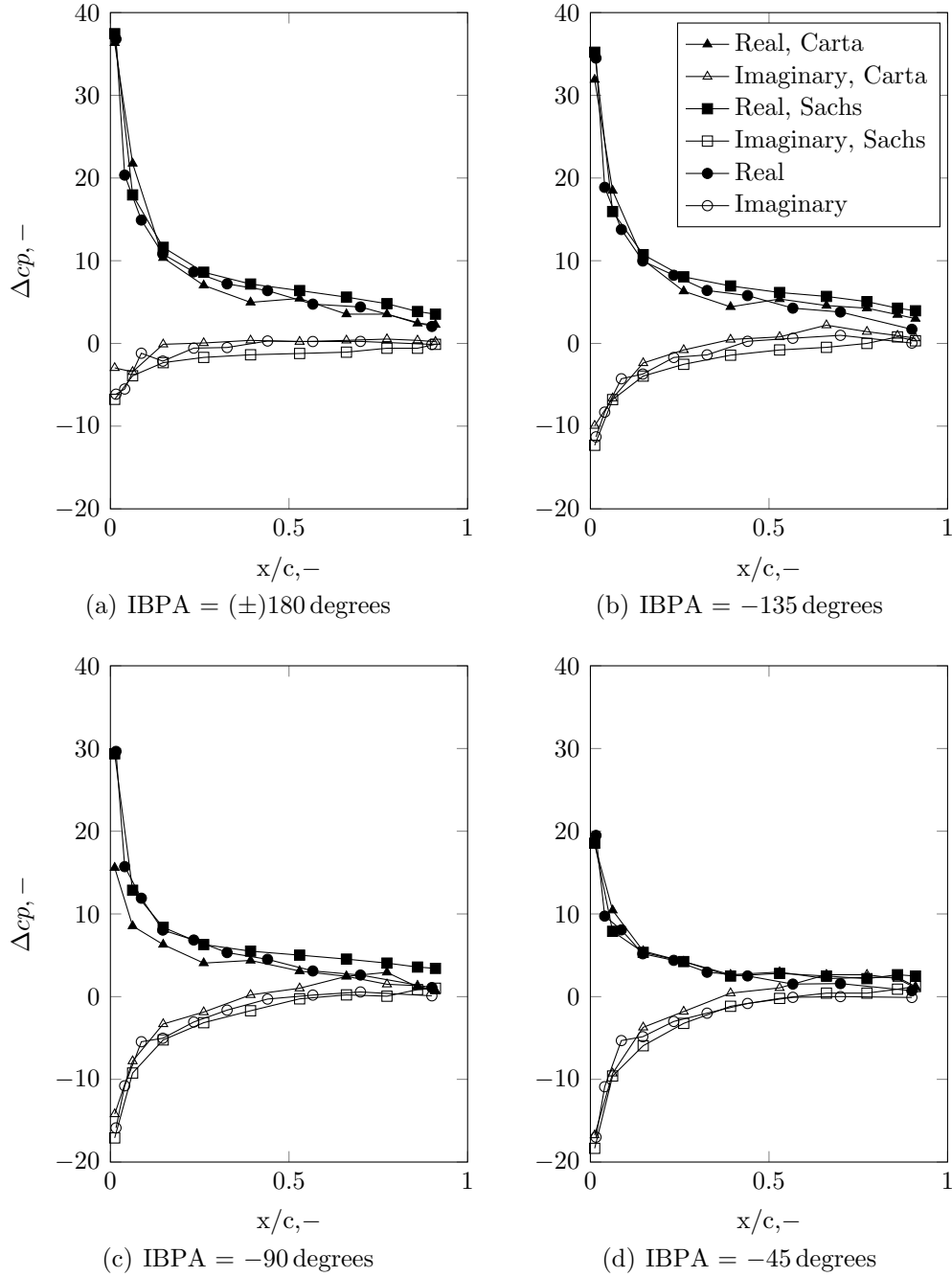


Figure 6.6: Variation of Real and Imaginary parts of unsteady pressure difference coefficient for a mean angle of attack of $\alpha_0 = 2$ degrees and an oscillation amplitude of $\hat{\alpha} = 0.5$ degrees at a reduced frequency of $k = 0.144$ (continued on the next page).

act as diffusers or nozzles, changing the axial pressure gradient relative to the steady set-up.

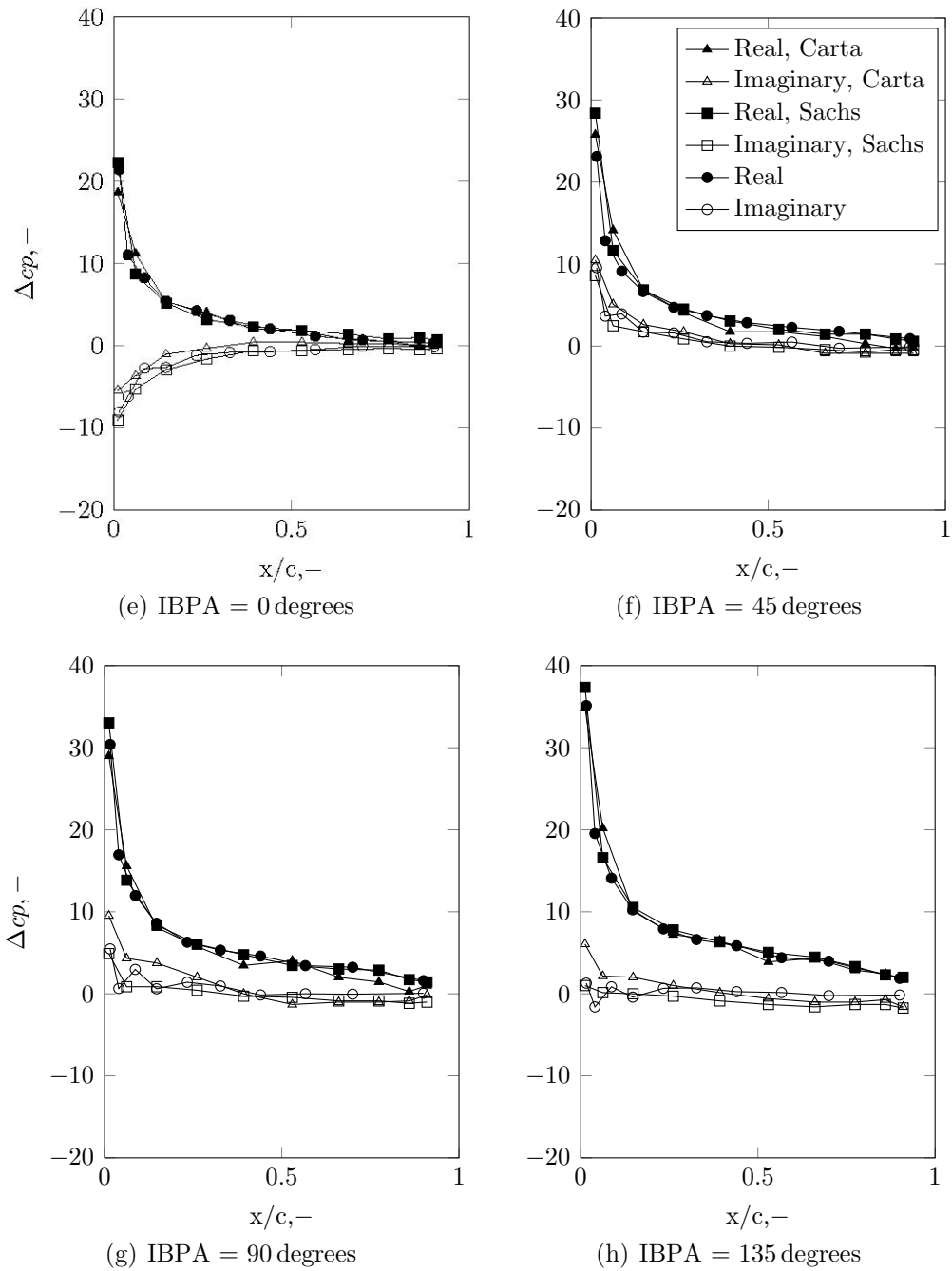


Figure 6.6: Variation of Real and Imaginary parts of unsteady pressure difference coefficient for a mean angle of attack of $\alpha_0 = 2$ degrees and an oscillation amplitude of $\hat{\alpha} = 0.5$ degrees at a reduced frequency of $k = 0.144$ (continued from the previous page).

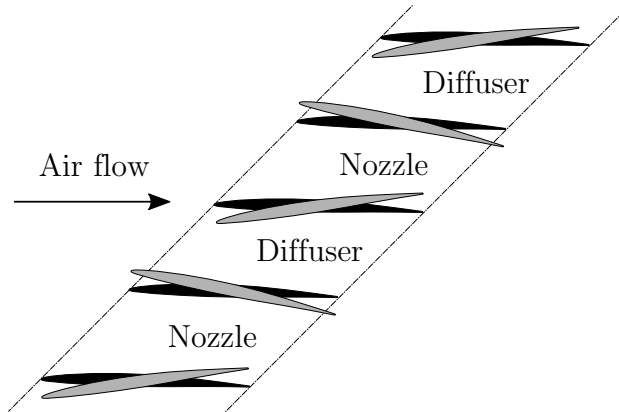


Figure 6.7: Change in flow passage area for an interblade phase angle of $\sigma = 180$ degrees - only the five central blades of the cascade are illustrated. Black blades illustrate the baseline configuration, grey ones, the blades oscillating out of phase.

Thus, the enlargement of the passage area is at maximum when adjacent blades oscillate out of phase to each others, as it is the case for $\sigma = 180$ degrees. The (unsteady) change of the flow passage is increasing from 0 degrees to $\sigma = 180$ degrees and decreases from $\sigma = 180$ degrees to $\sigma = 360$ degrees. In figure 6.7, the change in flow passage is illustrated for an IBPA of $\sigma = 180$ degrees, the black blades illustrated the baseline case and the grey ones when the blades are oscillate out of phase. The depicted amplitude is enlarged for a better visibility. The change in passage area is an almost symmetrical characteristic with regard to $\sigma = 180$ degrees if the blade camber is relatively small. That means the passage area of $\sigma = 45$ degrees is similar to the one of $\sigma = -45$ degrees. Consistently, it is also true for the passage area of $\sigma = 90$ degrees and $\sigma = -90$ degrees, and for $\sigma = 135$ degrees and $\sigma = -135$ degrees, respectively. This behavior can be observed by visiting figure 6.8, where the real part, $\Re(\Delta c_p)$, is plotted for all IBPA along the normalized chord. It increases from $\sigma = 0$ degrees to $\sigma = 180$ degrees and decreases towards $\sigma = -135$ degrees. For completeness, the imaginary part is plotted as well. In this figure, the IBPA with a positive $\Im(\Delta c_p)$ at the leading edge region can be clearly identified.

The results of the computation of the unsteady pressure difference depend also on the phasing of the pressure signal between the pressure and the suction side, reaching maximum values, when it is out of phase. Complementary to figure 6.6, data for values of c_p for $\sigma = 0$ degrees, $\sigma = 90$ degrees and $\sigma = 180$ degrees are discussed, and presented in figure 6.9. The figure displays

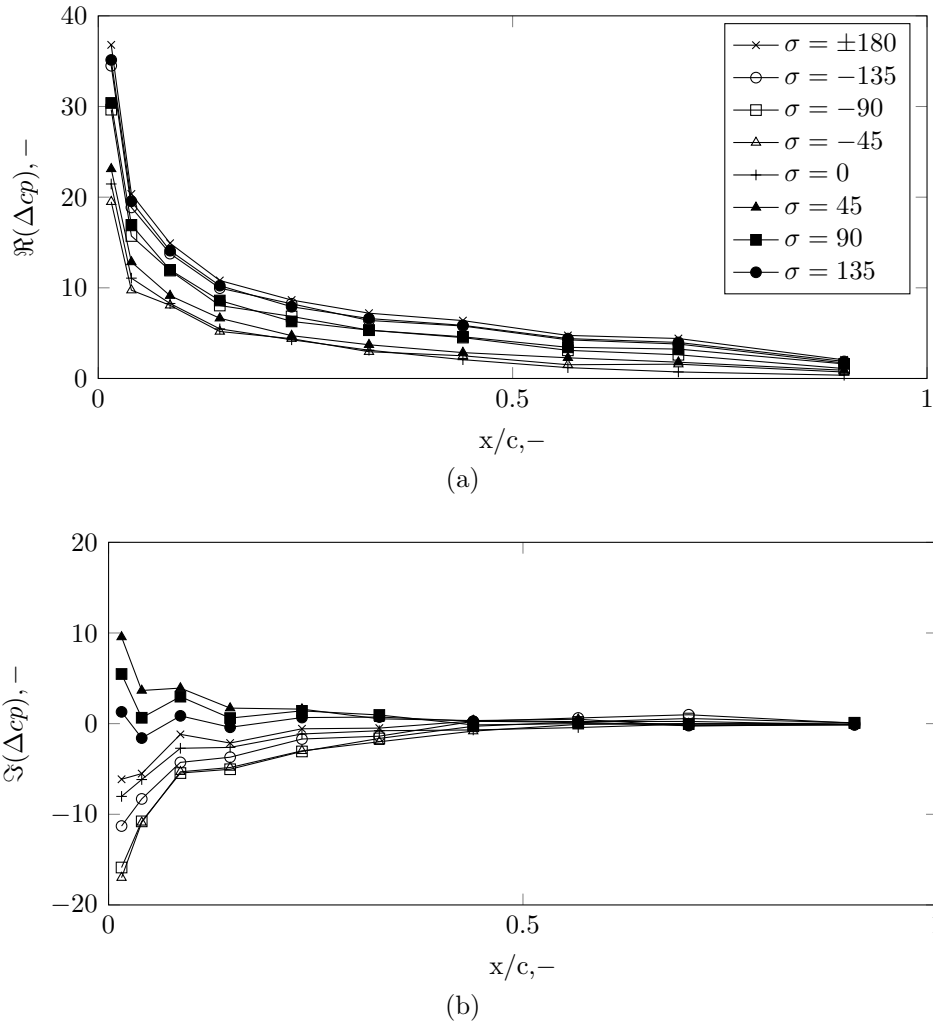


Figure 6.8: Variation of Real and Imaginary parts of unsteady pressure difference coefficient for a mean angle of attack of $\alpha_0 = 2$ degrees and an oscillation amplitude of $\hat{\alpha} = 0.5$ degrees at a reduced frequency of $k = 0.144$.

the unsteady phase averaged surface blade pressure on the suction and pressure side, as well as their difference plotted against one blade oscillation cycle. The first two pressure tap locations, namely, $x/c = 0.0157$ and $x/c = 0.04$, and two at the blade aft part are presented. For each presented tap location, the amplitude of cp is larger for $\sigma = 180$ degrees than for $\sigma = 90$ degrees and $\sigma = 0$ degrees that is in line with the data presented in figure 6.6. Due to the highest blade curvature at the leading edge, the unsteady pressure attains maximum values in this region. The phase of the pressure signal between the suction and pressure side is governed by the IBPA. For $\sigma = 0$ degrees, the phase angle decreases when moving aft the chord. It is inferred that the phase between pressure side and suction side is larger for the other two cases

due to the higher spatial frequency of the periodic flow pattern across the cascade blades.

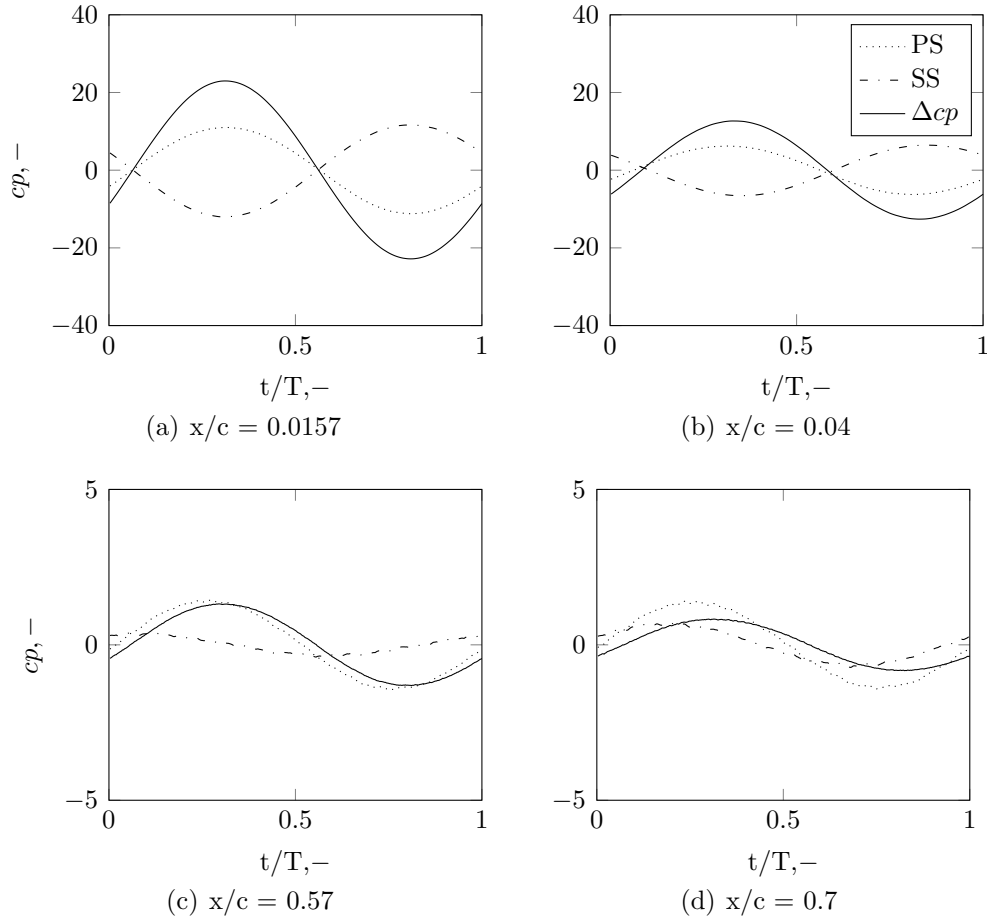


Figure 6.9: Ensemble phase averaged unsteady pressure coefficient on pressure and suction side, cp , and its difference, Δcp , for different chordwise position; at a mean angle of attack of $\alpha_0 = 2$ degrees, an oscillation amplitude of $\hat{\alpha} = 0.5$ degrees and an IBPA of $\sigma = 0$ degrees at a reduced frequency of $k = 0.144$ (continued on the next page).

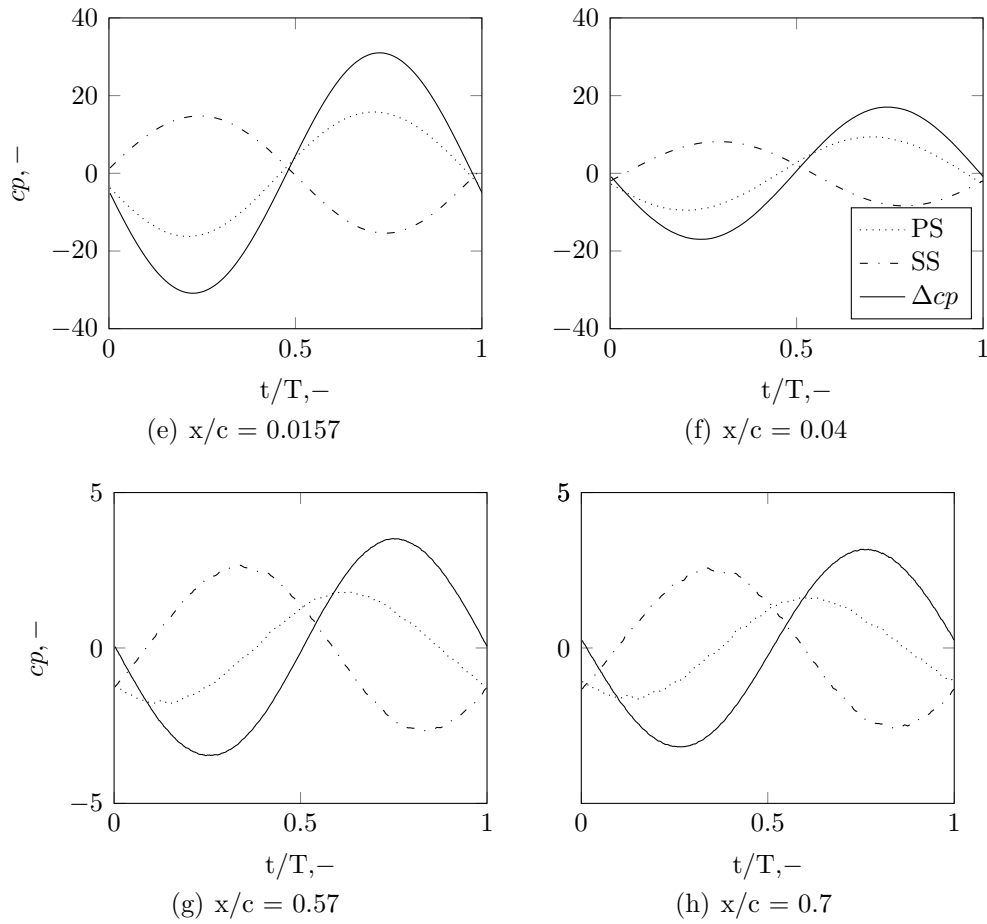


Figure 6.9: Ensemble phase averaged unsteady pressure coefficient on pressure and suction side, cp , and its difference, Δcp , for different chordwise positions; at a mean angle of attack of $\alpha_0 = 2$ degrees, an oscillation amplitude of $\hat{\alpha} = 0.5$ degrees and an IBPA of $\sigma = 90$ degrees at a reduced frequency of $k = 0.144$ (continued from the previous page).

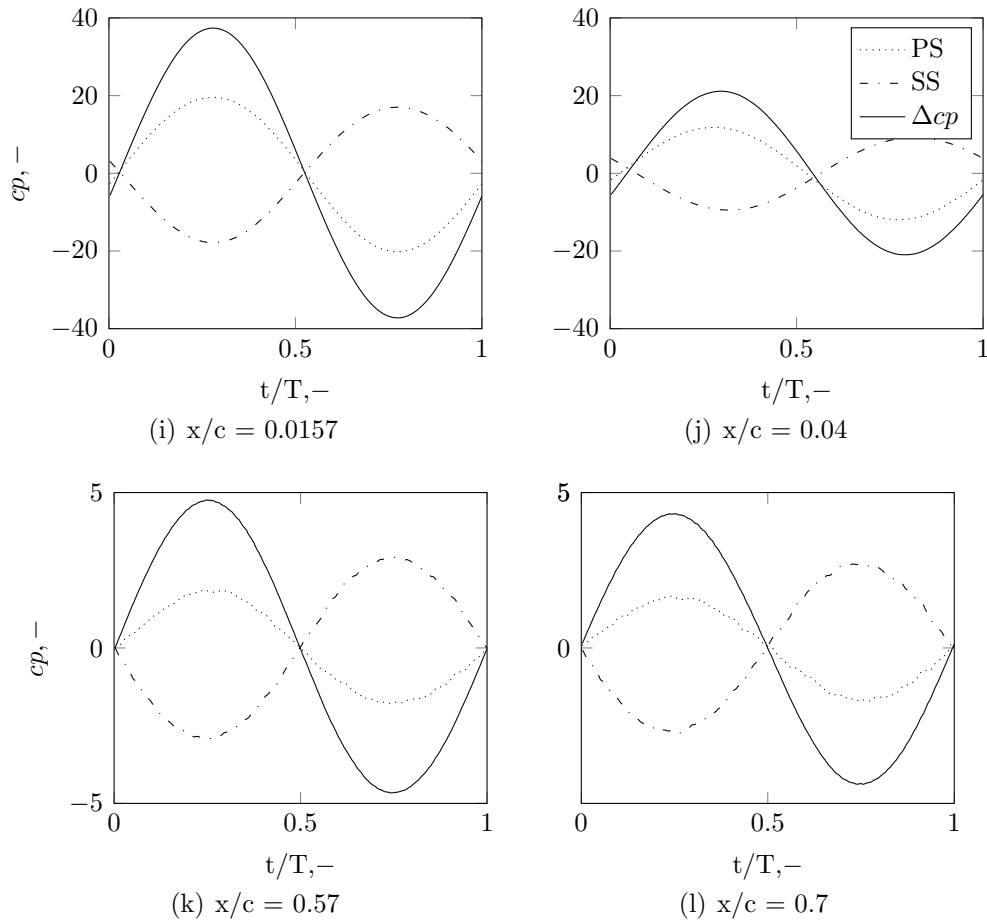


Figure 6.9: Ensemble phase averaged unsteady pressure coefficient on pressure and suction side, cp , and its difference, Δcp , for different chordwise positions; at a mean angle of attack of $\alpha_0 = 2$ degrees and an oscillation amplitude of $\hat{\alpha} = 0.5$ degrees and an IBPA of $\sigma = 180$ degrees at a reduced frequency of $k = 0.144$ (continued from the previous page).

Only one reduced frequency was investigated because the unsteady aerodynamic response is expected to experience very small changes when k is changing. Experimental studies [7], in a linear oscillating compressor cascade, reported that increasing the reduced frequencies of blades oscillating in pitch of up to $k = 0.539$ with the same profile cross section, angle of attack and oscillation amplitude, affects minimally the unsteady response.

For the current configurations, the pressure differences are much greater at the leading edge region than elsewhere on the blade and the variation of local phasing is more intense. This suggests a simplistic stability analysis based on the measurement data of the aerodynamic response at the blade front part. It is worth recalling that, when the pressure is in lead with respect to the blade motion, the imaginary part is positive. For IBPA $\sigma = 45$, $\sigma = 90$ and $\sigma = 135$ degrees the imaginary part of the unsteady pressure difference coefficient at the leading edge is greater than zero, as opposed to the remaining IBPAs, see again figure 6.6. Therefore, the cascade is presumably unstable.

However, in general, the only adequate measure to judge cascade stability is by computing integral stability parameters, such as the aerodynamic damping. The aerodynamic damping for the investigated IBPA is presented in figure 6.10 and displayed against the IBPA. The depicted data for IBPA $\sigma = \pm 180$ degrees correspond to one measurement. The aerodynamic damping is obtained by computing the imaginary part of the unsteady moment coefficient at the blade mid-chord according to equation 5.15. The sign of the aerodynamic damping is ruled by the phase angle between the first harmonic of the unsteady moment coefficient and the blade displacement, depicted in figure 6.11. If the phase is positive the aerodynamic damping parameter is negative, thus the cascade is unstable. For IBPA $\sigma = 45$, $\sigma = 90$ and $\sigma = 135$ degrees, the phase between unsteady moment coefficient and blade displacement is positive indicating instability. The remaining investigated IBPA are stable.

The unsteady moment coefficient, $C_{m(c/2)}$, is plotted exemplary for one blade oscillation cycle at IBPA $\sigma = 0$ degrees, $\sigma = 90$ degrees and $\sigma = 180$ degrees in figure 6.12. The magnitude of the moment coefficient follows approximately a parabolic shape, when plotted from $\sigma = 0$ degrees to $\sigma = 360$ degrees. The amplitude is maximum for $\sigma = 180$ degrees and minimum for $\sigma = 0$ degrees. This is consistent with the amplitudes of the unsteady pressure difference coefficient for $\sigma = 0$ degrees, $\sigma = 90$ degrees and $\sigma = 180$ degrees, see again figure 6.9.

The stability assessment, applying the aerodynamic damping, is consistent with the results obtained in terms of real and imaginary part of Δcp . Further,

all damping curves resemble an S-Shape, which is typical for an aerodynamic damping curve in turbomachines. The trend of the S-Curves is in agreement with the results of the experimental investigation presented by Carta [33] and in line with engine experience [39, 62].

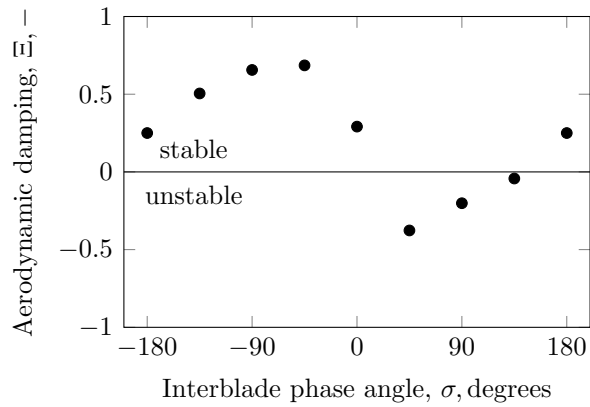


Figure 6.10: Aerodynamic damping at a mean angle of attack of $\alpha_0 = 2$ degrees and an oscillation amplitude of $\hat{\alpha} = 0.5$ degrees at a reduced frequency of $k = 0.144$.

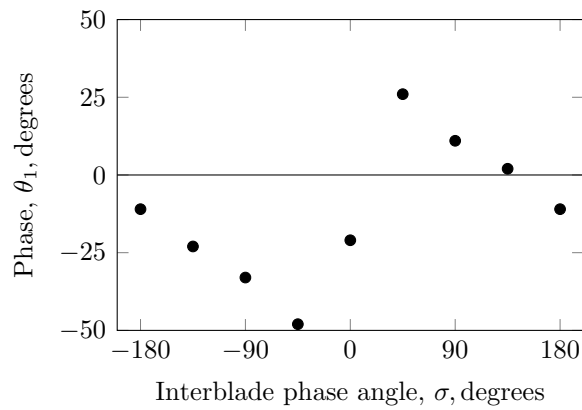


Figure 6.11: Phase angle between unsteady moment coefficient, $C_{m1(c/2)}$, and blade displacement at a mean angle of attack of $\alpha_0 = 2$ degrees and an oscillation amplitude of $\hat{\alpha} = 0.5$ degrees at a reduced frequency of $k = 0.144$.

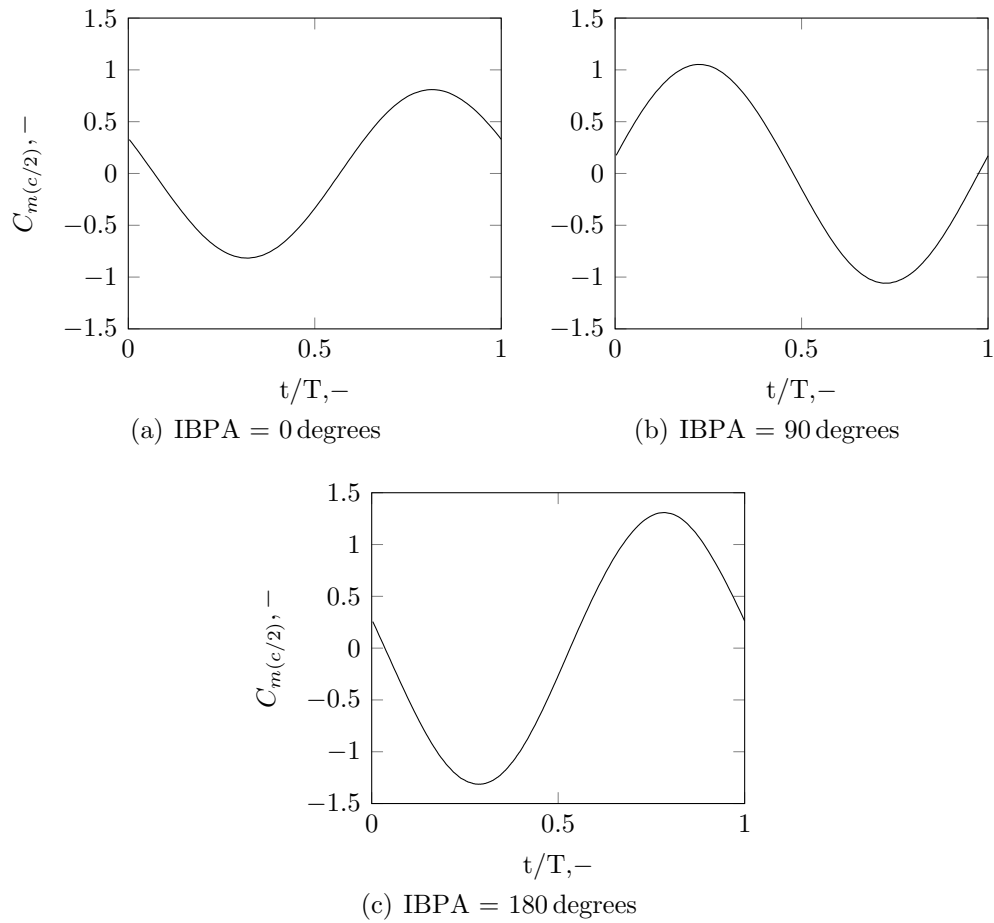


Figure 6.12: Unsteady moment coefficient, $C_{m(c/2)}$, computed from ensemble phase averaged pressure data, at a mean angle of attack of $\alpha_0 = 2$ degrees for different IBPAs and an oscillation amplitude of $\hat{\alpha} = 0.5$ degrees at a reduced frequency of $k = 0.144$.

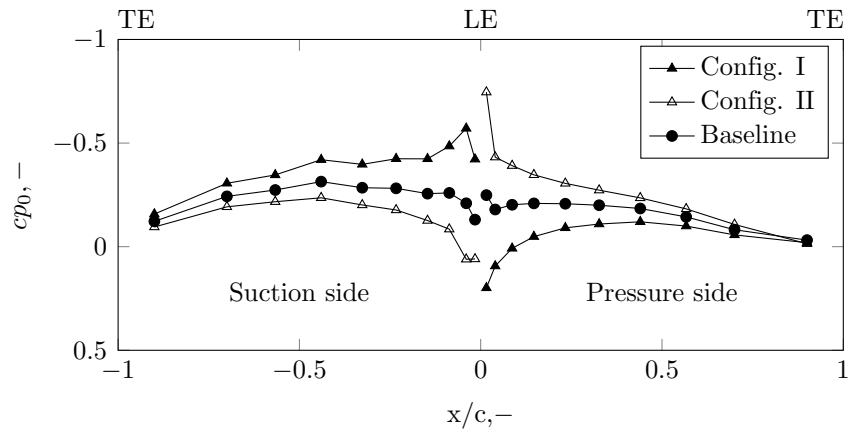
6.4 Aerodynamic Mistuning

For cluster I and II, see table 6.1, all experimental investigations were carried out at a reduced frequency of $k = 0.244$ with a blade oscillation frequency of $f = 9\text{ Hz}$. The reduced frequency has been chosen to be realistic for real engine configurations, see again 2.1.3. The experimental data presented hereinafter were acquired at the cascade central blade, namely blade 5. First, the steady-state results are discussed. Then, the analyses of the phase averaged data of the time-variant blade surface pressure and strain gauges are presented. Finally, the stability is assessed by computing the aerodynamic damping.

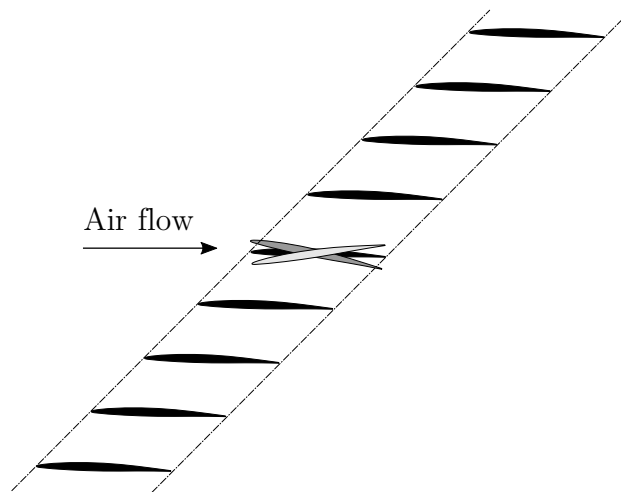
6.4.1 Cluster I - Aerodynamic Response and Stability Assessment (one, alternating, random pattern)

Steady-state aerodynamics The steady data are presented in form of the steady pressure coefficient, depicted in figure 6.13. The steady pressure coefficient, cp_0 , is plotted along the normalized chord for the investigated cases and the baseline configuration. Figure 6.13 (a) shows the pressure coefficients for the mistuned cases, i.e. those which the stagger angle of the cascade central blade was varied, see figure 6.13 (b) for the patterns. Figure 6.13 (c) shows the pressure coefficients for the cases with an alternating pattern, a corresponding scheme is displayed in figure 6.13 (d). For the random case, the distribution of the steady pressure coefficient and its matching pattern are depicted in 6.13 (e) and (f), respectively.

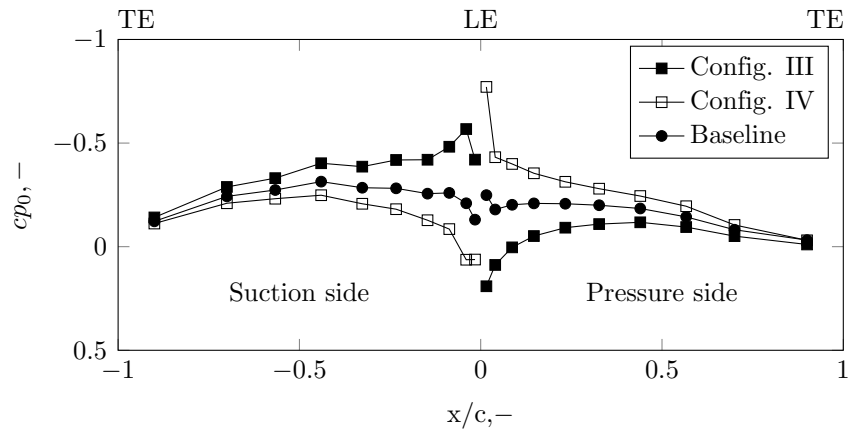
Configurations I, III and V feature an increase in stagger angle of $\Delta\gamma = +2$ degrees, and a decrease of $\Delta\gamma = -2$ degrees for configuration II and IV. For the latter cases, starting from the leading edge region on the suction side, cp_0 decreases up to the minimum-pressure chordwise station and rises in the meantime on the pressure side. Compared to the configurations with positive stagger angle variation, pressure and suction side are swapped. Those configurations attain minimum values on the suction side in the blade front part and maximum values on the pressure side. For the configurations II and IV, the trend is the opposite. The effect of negative and positive incidence is clearly noticeable. Thus, the blade loading for configurations I, III and V is higher compared to the baseline case and lower for the configurations II and IV.



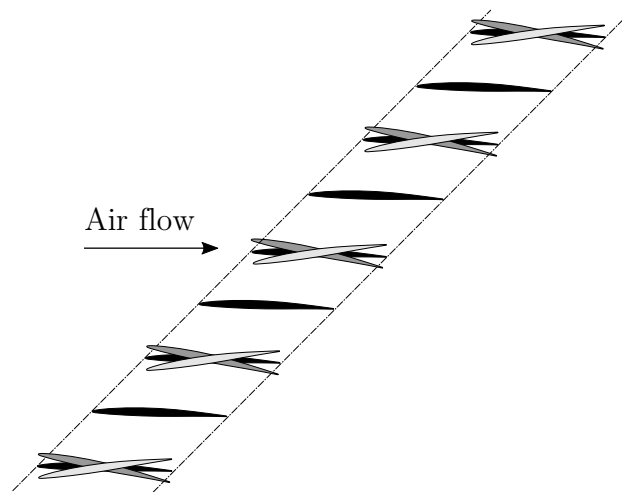
(a) Steady pressure coefficient chordwise distribution.



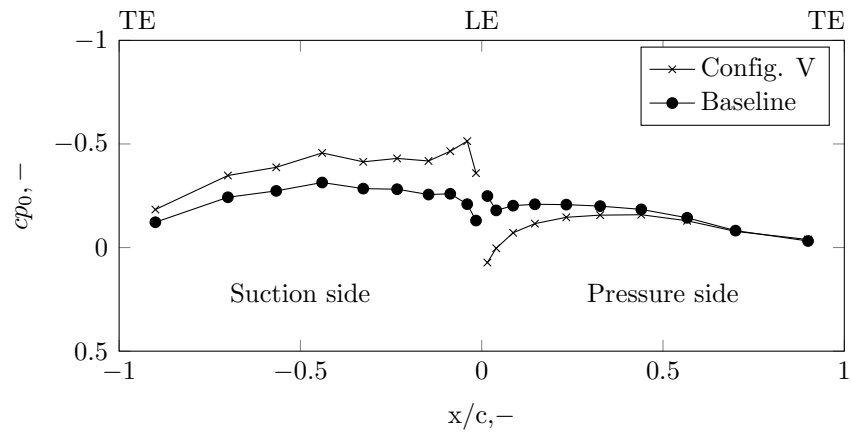
(b) One-blade mis-staggering pattern - configuration I (dark grey) and configuration II (light grey).



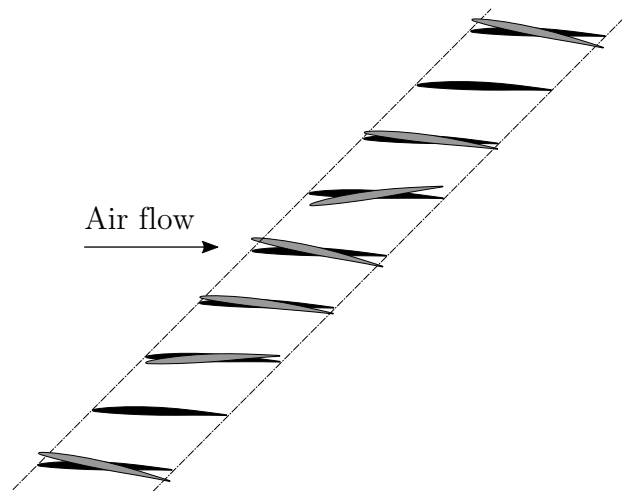
(c) Steady pressure coefficient chordwise distribution.



(d) Alternating mis-staggering pattern - configuration III (dark grey) and configuration IV (light grey).



(e) Steady pressure coefficient chordwise distribution.



(f) Random mis-staggering pattern - configuration V.

Figure 6.13: Cluster I - steady pressure coefficient chordwise distribution on the cascade central blade for baseline and mistuned configurations.

Unsteady aerodynamics The experimental data are presented as real and imaginary parts of the unsteady pressure difference coefficient. In the left column of figure 6.14, the real parts are plotted against the x-coordinate normalized by the blade chord for all investigated IBPAs, and in the right one, the imaginary parts are displayed. The data are computed by phase referencing the pressure data to the sinusoidal pitching motion of the blade. As discussed in section 6.3, the passage area is changed by the IBPA, resulting in an increase or decrease of the axial pressure gradient in the flow passage compared to the steady set-up, affecting the unsteady blade pressure distribution. For the mistuned cases, the flow passage is further altered. However, the configurations with a positive stagger angle variations, namely config. I, III, V, develop a similar trend at the blade leading and trailing edge region compared to the baseline case with respect to the real and imaginary part of Δcp . Thus, the one-blade (config. I), the alternating blade-to-blade (config. III) and the random (config. V) mis-staggering patterns feature similar unsteady aerodynamic responses.

For the configurations II and IV that are subjected to a negative change in stagger angle, an increase in the real part, $\Re(\Delta cp)$, at the first pressure tap position and a drop at the second pressure tap are observed, whereas for the remaining ones the trend is similar to the baseline case. In figure 6.15, the results of the analysis of the time-variant pressure with the Fourier transform technique are presented; the normalized magnitude of cp is plotted versus the frequency for the two pressure taps closest to the leading edge, namely $x/c = 0.0157$ and $x/c = 0.04$. The left column of figure 6.15 contains the results for the pressure side and the right column is related to the suction side. For the suction side, the pressure signals of the baseline and for the mistuned cases show a distinguished peak at the blade oscillation frequency, being $f = 9$ Hz, for both pressure tap locations. On the pressure side, for configuration II and IV, the maximum normalized magnitude is observed at the second-harmonic frequency, being twice the blade pitching frequency, namely about $f = 18$ Hz. Apart from these incidences no higher frequency content was revealed, the results of the analysis of the pressure signal at the remaining taps are displayed in the appendix A - Frequency plot in figure A.1. Vortical structures or separation bubbles are not unusual to occur at the leading edge of oscillating airfoils in pitching motion and could be the cause of the 18 Hz peak observed in the configurations II and IV. In Ref. [87], the pitching of an airfoil was studied experimentally and it was reported that the pressure distribution was altered considerable in time due to an growing vortex at the leading edge. In the aforementioned references, this observation was related to the dynamic stall behaviour, present for large pitching amplitudes. Experiments conducted at an oscillating compressor cascade, see Ref. [61], reported a small region of separated flow on the suction

side in the leading edge region. The Mach number in Ref. [61] is comparable to the one applied in the present thesis. However a pitching amplitude of 2 degrees and an incidence of 2.5 degrees at a stagger angle of 2.5 degrees were used. The separation occurred not for all IBPAs and was periodically in its nature of appearance. To exclude the possibility of the occurrence of a vortex shedding phenomena, a shedding frequency associated with the Von Kármán Strouhal number was calculated -- often causing oscillations at twice the motion frequency due to the alternate shedding of counter-rotating vortical structures, see Ref. [88]. Based on the experimental study of Huang et al. [89], in which the Strouhal number was studied in the dependence of the Reynolds number and angle of attack, the Strouhal number is estimated to be 0.25, using as characteristic length the crossflow projection of the airfoil. For the computation of the shedding frequency the free flow velocity was taken into account, yielding in a frequency of 972.2 Hz. The computed frequency diverges significantly from the frequencies observed at the second pressure tap for configurations II and IV in figure 6.15. There might be additional flow phenomena such as a local separation at the leading edge due to i) the low turbulence level in the test rig ; ii) the influence of the IBPA on the blade surface pressure; iii) the stagger angle alteration. To draw a complete picture of this phenomenon, additional measurement techniques such as particle image velocimetry and hot wire anemometer would be needed. These investigations target the study of higher order flow modes and are not among the objectives of this work and considered as an outlook of the present investigations. Further, the influence of high order flow modes on the computation of the aerodynamic damping is negligible in the current context, see equation 2.8.

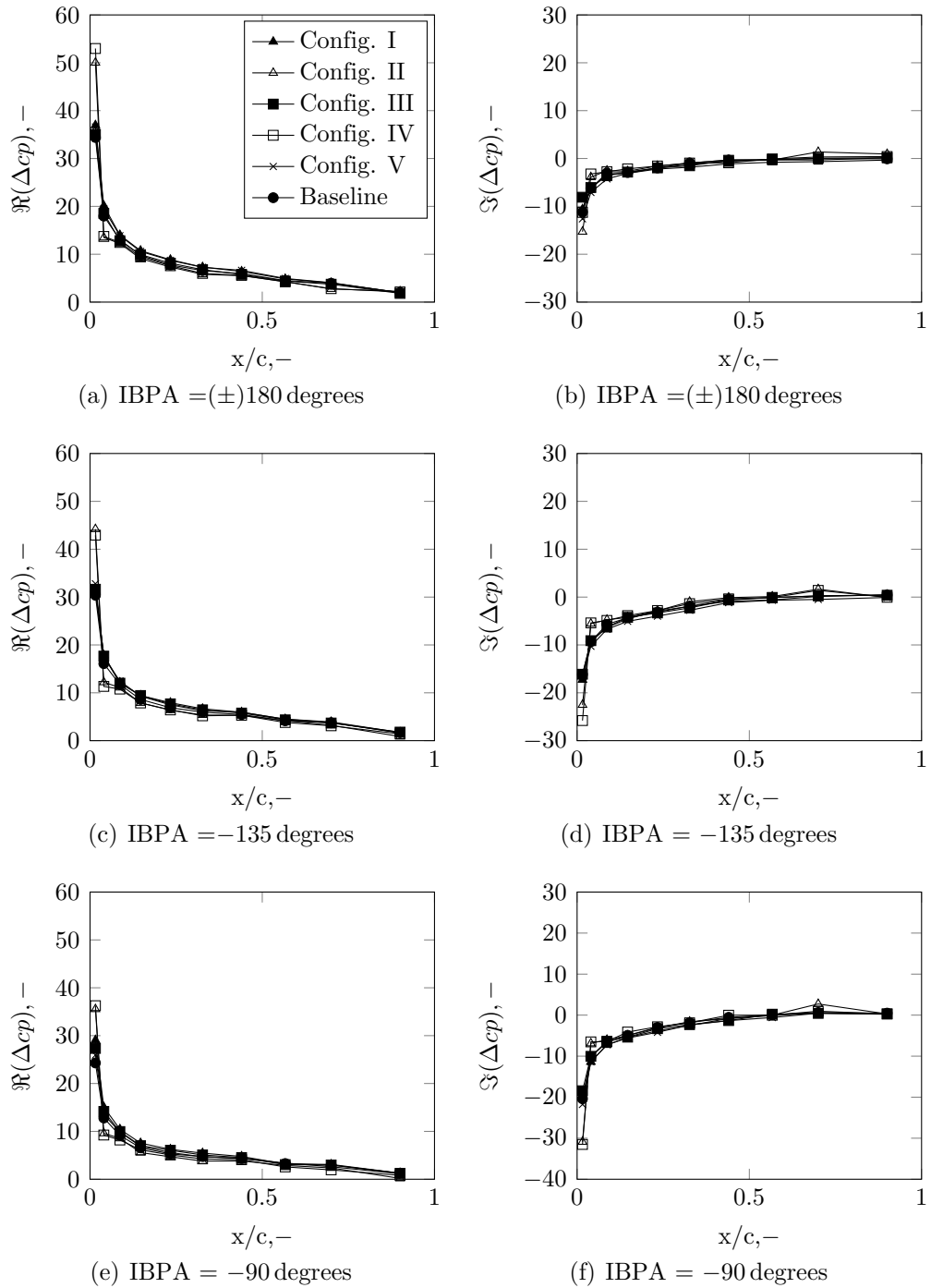


Figure 6.14: Variation of real and imaginary parts of unsteady pressure difference coefficient for an oscillation amplitude of $\hat{\alpha} = 0.5$ degrees at a reduced frequency of $k = 0.244$ (continued on the next page).

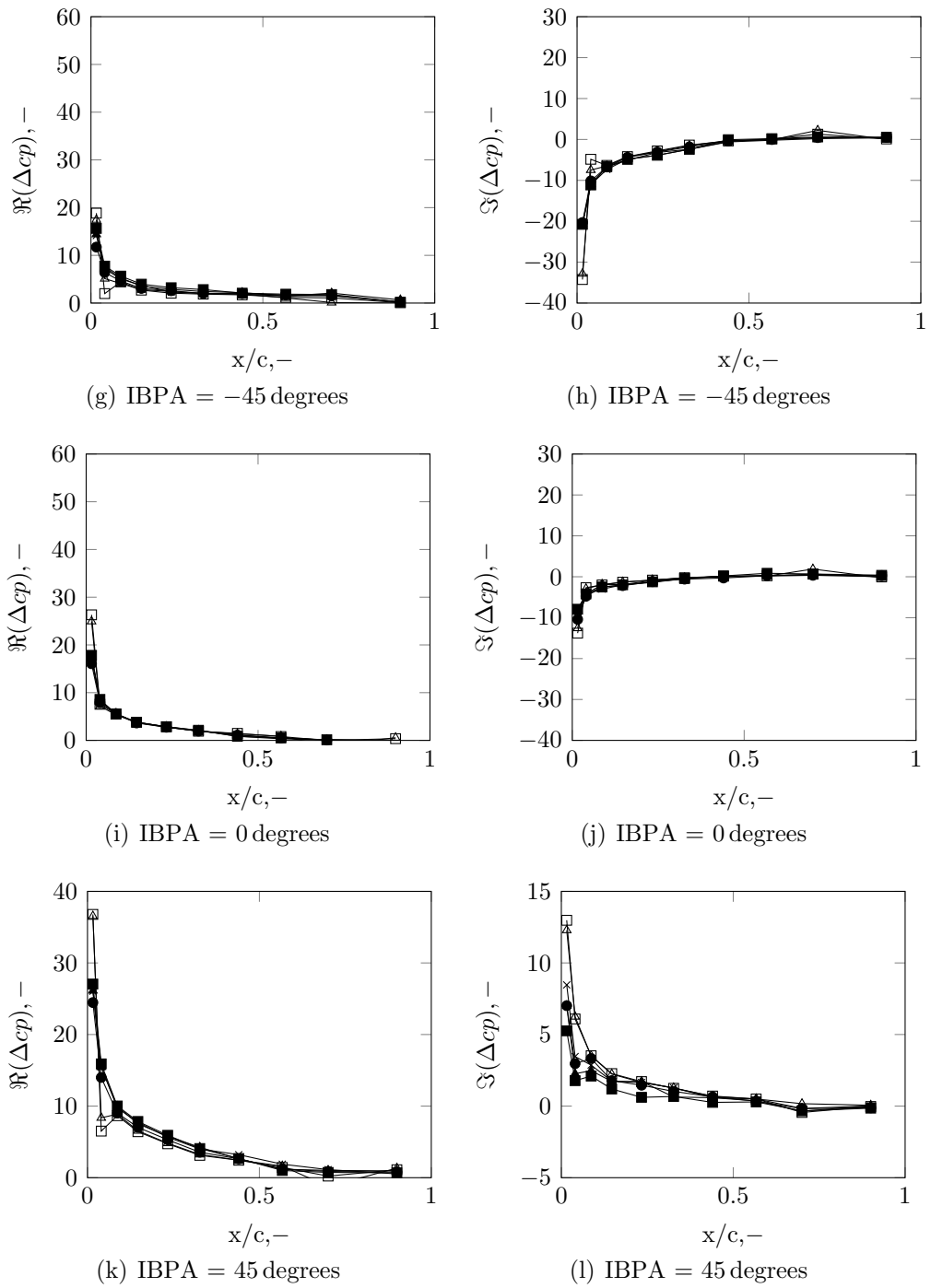


Figure 6.14: Variation of real and imaginary parts of unsteady pressure difference coefficient for an oscillation amplitude of $\hat{\alpha} = 0.5$ degrees at a reduced frequency of $k = 0.244$ (continued from the previous page).

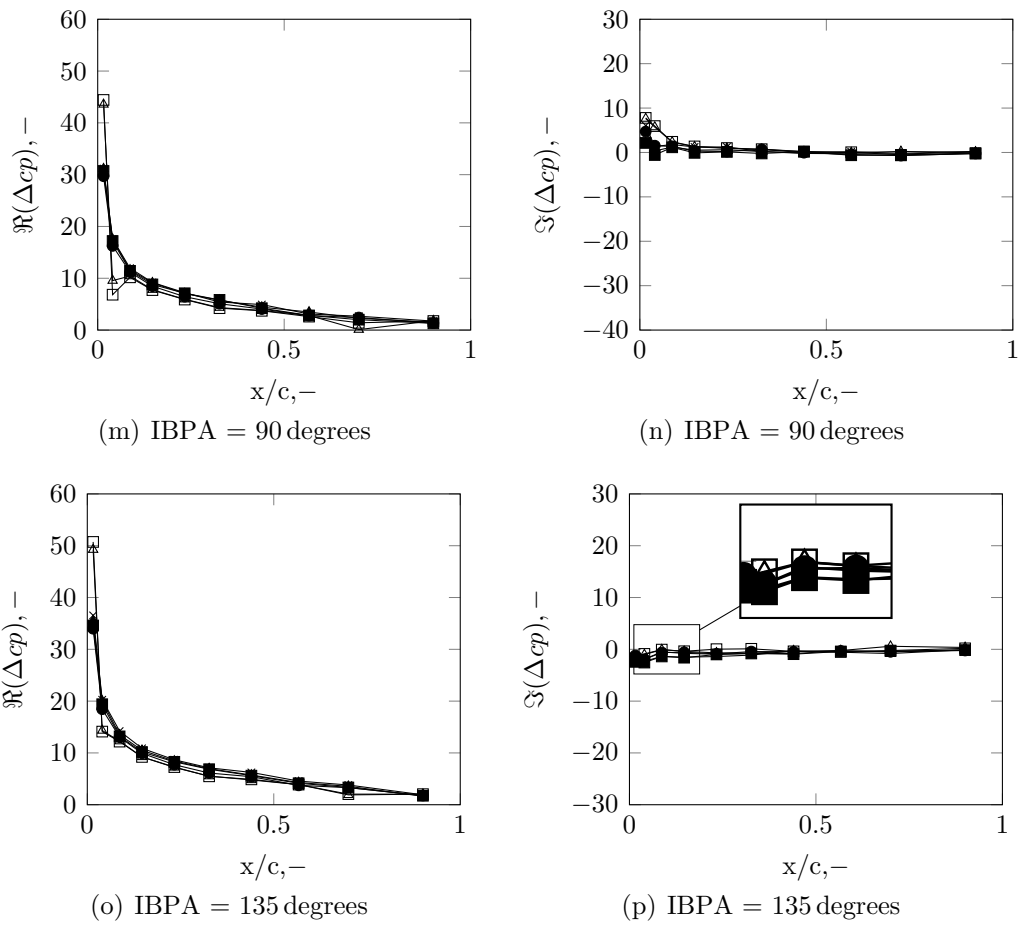


Figure 6.14: Variation of real and imaginary parts of unsteady pressure difference coefficient for an oscillation amplitude of $\hat{\alpha} = 0.5$ degrees at a reduced frequency of $k = 0.244$ (continued from the previous page).

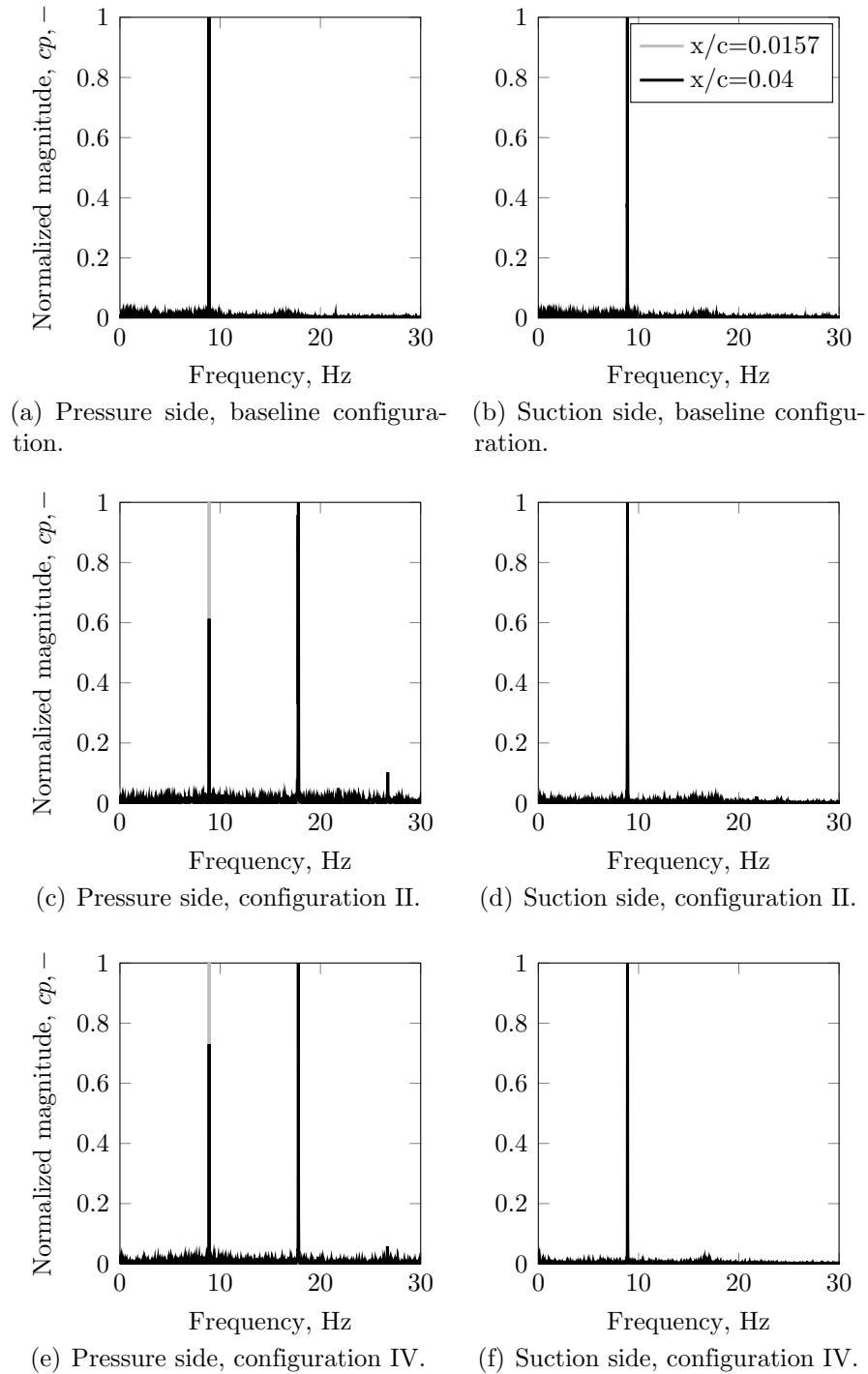


Figure 6.15: Normalized Fourier transform magnitudes of surface-pressure at $IBPA = 135$ degrees at a reduced frequency of $k = 0.244$.

Stability assessment

Baseline configuration The sign of the imaginary part of Δcp , indicates region of instability, as explained in section 6.3. For the baseline configuration, the imaginary part at the leading edge region is positive for two IBPAs, namely $\sigma = 45$ degrees and $\sigma = 90$ degrees, thus the pressure response is in lead with respect to the blade motion, destabilizing locally the blade front area. Therefore, the cascade is presumably unstable for these two IBPAs, see again figure 6.14. The mistuned cases with a positive stagger angle variation at the cascade central blade or for various blades, namely configurations I, III and V, have a similar trend with respect to the sign of the imaginary part compared to the baseline configuration. On the contrary the configurations featuring a negative stagger angle variation at the cascade central blade or at every second one -- configurations II and IV -- follow the same trend as the baseline case with respect to the sign of $\Im(\Delta cp)$, beside for the $\sigma = 135$ degrees. Thus an unstable cascade is expected for the aforementioned IBPA. However, to judge cascade stability, the only appropriate measure is to compute integral values such as the aerodynamic damping.

In figure 6.16, the aerodynamic damping is plotted versus the investigated range of IBPAs for all cases of the experimental study of cluster I. The aerodynamic damping is calculated based on equation 5.15. For the baseline case, only IBPA $\sigma = 45$ degrees and $\sigma = 90$ degrees indicate an unstable system. $\sigma = 45$ degrees attains the minimum damping. The aerodynamic damping appears, when plotted against the IBPA, in a S-Shape, that is in agreement with the conclusion drawn in Ref. [33].

One-blade mis-staggering For the one-blade positive stagger angle variation i.e. configuration I, the characteristic of the shape of the damping curve is maintained in the sense that the cascade is stable for the same investigated IBPAs compared to the baseline case. The curve is moved slightly upwards and the cascade is therefore more stable compared to the baseline case, apart from $\sigma = 0$ degrees. For IBPA $\sigma = 45$ degrees and $\sigma = 90$ degrees, the aerodynamic damping increases by 17% and 46%, respectively. An opposite trend is noticed for the configuration II which experiences negative stagger angle variations - the damping curve is moved downwards compared to the baseline case and as a result the IBPA $\sigma = 135$ degrees becomes unstable. The observations are in accordance with the previous discussion of the assessment of stability based on the distribution of Δcp , see figure 6.14; for example, the imaginary part of Δcp is positive in the leading edge region for $\sigma = 45$ degrees and $\sigma = 90$ degrees, indicating an unstable system as

confirmed by the negative damping displayed in figure 6.16.

Alternating mis-staggering The alternating mis-staggering patterns - configurations III and IV - show an analogous damping behaviour as the single-blade pattern in terms of the direction of the stagger angle alteration. That is, for configurations I and III, featuring a positive change of stagger angle, the same IBPAs are unstable. For configuration III, the aerodynamic damping increases by 28 % and 58 % for IBPA $\sigma = 45$ degrees and $\sigma = 90$ degrees, respectively. The same holds true for configuration IV, following the trend of the damping curve of configuration II.

Random mis-staggering For the random mistuning pattern, only a weak influence on the cascade stability can be reported. For positive IBPAs no significant shift is noticed compared to the baseline case. However, for negative IBPAs, the system becomes slightly more stable, with an upward shift of the curve. By revisiting figure 6.14, it can also be noted that the chordwise pressure distribution does not change significantly, as expected, in comparison to the baseline configuration.

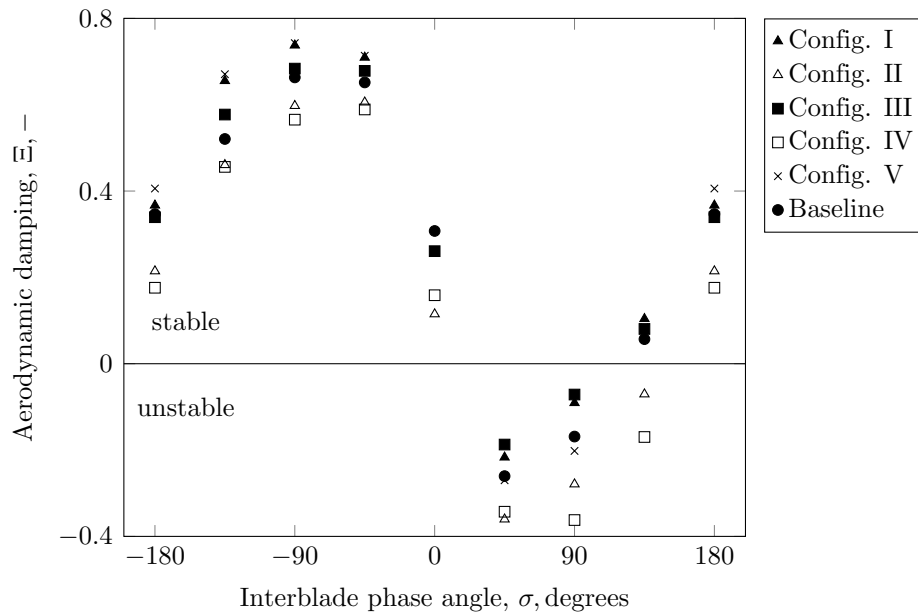


Figure 6.16: Aerodynamic damping for an oscillation amplitude of $\hat{\alpha} = 0.5$ degrees at a reduced frequency of $k = 0.244$.

Complementary to figure 6.16, the phase between the unsteady moment coefficient and the blade displacement is displayed in figure 6.17. The phase is illustrated as absolute values, as the sign of the phase is decisive. The maximum relative change of the phase with respect to the baseline for negative IBPA is noticeable for IBPA $\sigma = -180$ degrees. Specifically for configurations II and IV the percent differences with respect to the baseline are 33% and 44%, respectively, highlighting a huge effect of the mis-staggering on the cascade aeroelastic stability. For the remaining negative IBPA angles, the variation is below 13%.

The phase becomes more positive for the configurations with negative stagger angle variations (configuration II and IV) compared to the baseline case for positive interblade phase angles. A large value is attained also for an IBPA $\sigma = 135$ degrees for case IV with a relative change of 433%. That makes the system more unstable and is consistent with the computed damping curve, see again figure 6.16, in which the lowest values are obtained for the configurations II and IV.

The relative change in amplitude in percent of the unsteady moment coefficient with respect to the baseline configuration is depicted in figure 6.18. The amplitude of the moment coefficient experiences a maximum change of 16% at an IBPA $\sigma = -90$ degrees for configuration I. A peak value is also reached for configuration IV with a relative difference of -15% . The drop of amplitude of the configurations II and IV, compared to the other cases, results from the decrease in unsteady pressure difference coefficient at the second pressure tap, see figure 6.14.

The changes in phase, for configurations II and IV, are many times larger than compared to the change in amplitude of the unsteady moment coefficient, especially for positive interblade phase angle, influencing stability remarkably. The two cases thus represent the critical configuration for the design.

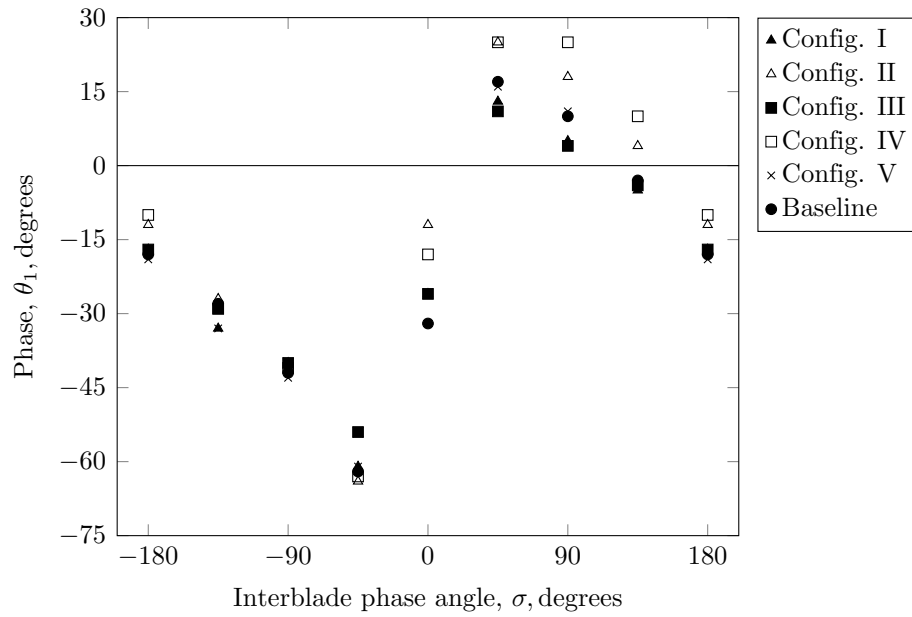


Figure 6.17: Phase angle between unsteady moment coefficient, $C_{m1(c/2)}$, and blade displacement for an oscillation amplitude of $\hat{\alpha} = 0.5$ degrees at a reduced frequency of $k = 0.244$.

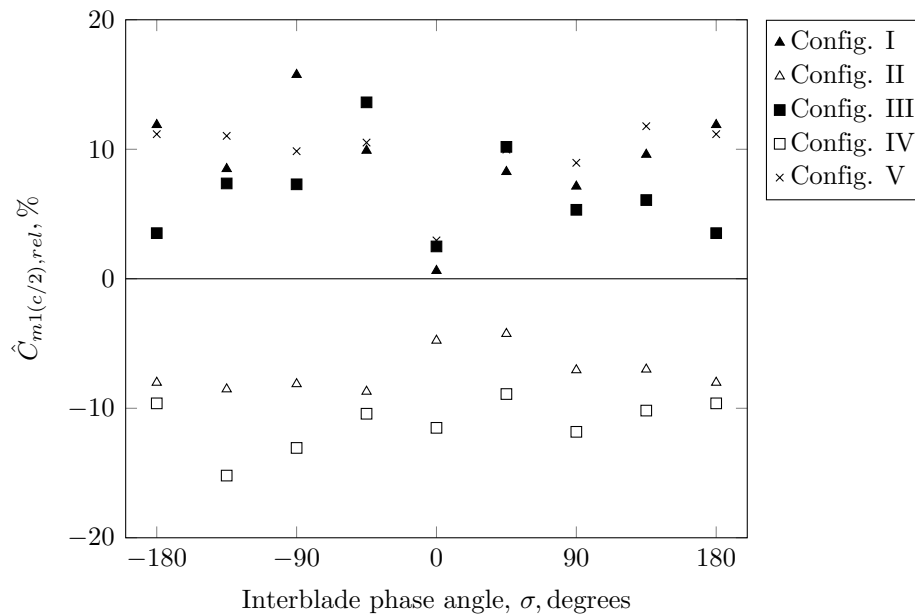


Figure 6.18: Relative change in amplitude of unsteady moment coefficient, $\hat{C}_{m1(c/2),rel}$, for an oscillation amplitude of $\hat{\alpha} = 0.5$ degrees at a reduced frequency of $k = 0.244$.

6.4.2 Cluster II - Aerodynamic Response and Stability Assessment (homogeneous pattern)

Steady-state aerodynamics Steady pressure coefficient distributions are shown in figure 6.19 for the experimental part of the study in which the stagger angles of all blades in the cascade were altered within one configuration. The steady pressure coefficient is plotted along the normalized chord for pressure and suction side for the five investigated cases and the baseline configuration. For all cases, the pressure coefficient increases gradually along the pressure side and reaches the smallest cp_0 at the first pressure tap location. On the suction side, the pressure reaches a maximum at the leading edge region. Then, it decreases towards a minimum at $\sim 0.75c$. For the baseline case, after the first pressure tap on the pressure side, the pressure coefficient experiences first an increase and then a decrease. On the suction side, for configurations VII to X, the pressure is above the static pressure in the inlet and then decreasing along the rear part of the blade. For the remaining cases, the pressure is below the static pressure in the inflow at the leading edge region and increases along the chord on the suction side. To summarize, the blade loading is in general decreasing from configuration VI to X.

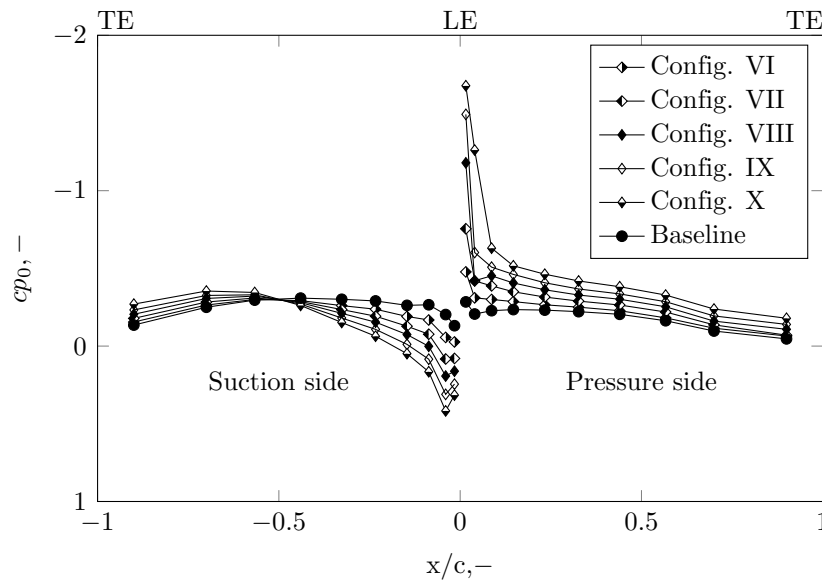


Figure 6.19: Steady pressure coefficient chordwise distribution on the cascade central blade for baseline and mistuned configurations.

Unsteady aerodynamics As in the experimental cluster I, the final unsteady pressure data are depicted in terms of real and imaginary parts of the pressure difference coefficient Δcp . The unsteady pressure data is referenced

to the blade pitching motion. In figure 6.20, the real and imaginary parts of the unsteady pressure are plotted against the normalized chord, for each of the investigated IBPAs. In the front region, the magnitudes of the real and imaginary part of Δcp exhibit peak values before decaying towards the rear part of the blade. This is due to the fact that the airfoil has a higher curvature in the leading edge region than in the blade aft part. As a consequence, the accelerations and decelerations on the two blade sides are higher in magnitude on the fore part of the blade. For the investigated cases the pressure gradient increases from configuration V to X, see again figure 6.19. This flow behaviour leads to high pressure differences in the leading edge regions, observable in the subfigures of figure 6.20, where real and imaginary parts attain maximum values. In these figures, the influence of the variation of the stagger angle alteration is clearly noticeable. This effect can be observed by looking at the very left sides of the plots in figure 6.20. The maximum values for stagger angle variation of $\Delta\gamma < -2$ are obtained at the second point from the left. Further, it is noteworthy to recall, that when computing Δcp from two unsteady signals of two opposite facing pressure taps on pressure and suction side, the value is maximal when the two pressure signals are out of phase and decreases when the phase angle between the two signals is reduced, see again figure 6.9.

In figure 6.20 the major influence of the IBPA on the chordwise pressure distribution is visible as well. Due to the traveling wave, each blade experiences a continuous change in incidence and couples aerodynamically with the blades in the cascade altering the chordwise unsteady pressure distribution significantly for each individual IBPA. As pointed out previously, the passage area changes with the IBPA. When the airfoils oscillate at a constant IBPA, the blade walls act as diffuser or nozzle, changing the axial pressure gradient relative to the steady set-up. Thus, the pressure and suction side of the airfoils experience different passage cross sections. The enlargement of the passage area reaches a maximum when neighbouring blades oscillate out of phase and a minimum for $\sigma = 0$ degrees. Hence, the magnitudes of the real and imaginary part of the pressure response are increasing from $\sigma = 0$ degrees to $\sigma = 180$ degrees and then decreasing from $\sigma = -135$ degrees to $\sigma = -45$ degrees for all investigated configurations. Differently from the real part, the imaginary part of Δcp changes in sign according to the IBPA. In particular, for $\sigma = 45$ degrees and $\sigma = 90$ degrees, the imaginary part of Δcp becomes positive for the investigated cases.

On the other hand, the imaginary part of Δcp remains negative in the same blade area, for all the other cases. This change in sign of the imaginary parts is due to the fact that the pressure response phase switches sign from negative to positive. The sudden phase change at the blade front part suggests that this results from a combination of several effects. Large pressure gradients

occur at the leading edge area due to the airfoil curvature, intensified with increasing or decreasing stagger angle variation. Together with the pressure wave traveling across the cascade, considerable changes in the local phasing take place. This has also been noted by Keerthi et al. [61], who had a fixed stagger angle in their experimental studies with pitching airfoils in a cascade. They stated that "when the pressure gradient is large, a small displacement of the bulk fluid can result in a large variation of local phasing". In addition, the flow experiences inertia and damping effects because of the blade motion, affecting the pressure response phase along the chord [90]. This behaviour has been studied in the context of pitching airfoils configurations, where these unsteady phenomena have been reported to be dominant as well at the leading and trailing edge area, see e.g. Motta et al. [91]. Thus, the phase variations at the leading edge are an interplay of : i) steady mean high pressure gradients; ii) pressure wave at the blade frequency traveling across the cascade; iii) unsteady aerodynamics phenomena at the blade frequency, as a result of the imposed sinusoidal motion.

Also, compared to the experimental study of cluster I, a Fourier transform analysis was conducted, to investigate if any significant higher harmonics are present. The results of the first two pressure taps of case VII are shown in figure 6.21 and the remaining ones in figure A.2. The first harmonic of the pressure signal is the blade frequency. A distinct peak at the second pressure tap from the leading edge at $f = 18$ Hz is observed which is similar to the data of configurations II and IV featuring the same stagger angle modifications.

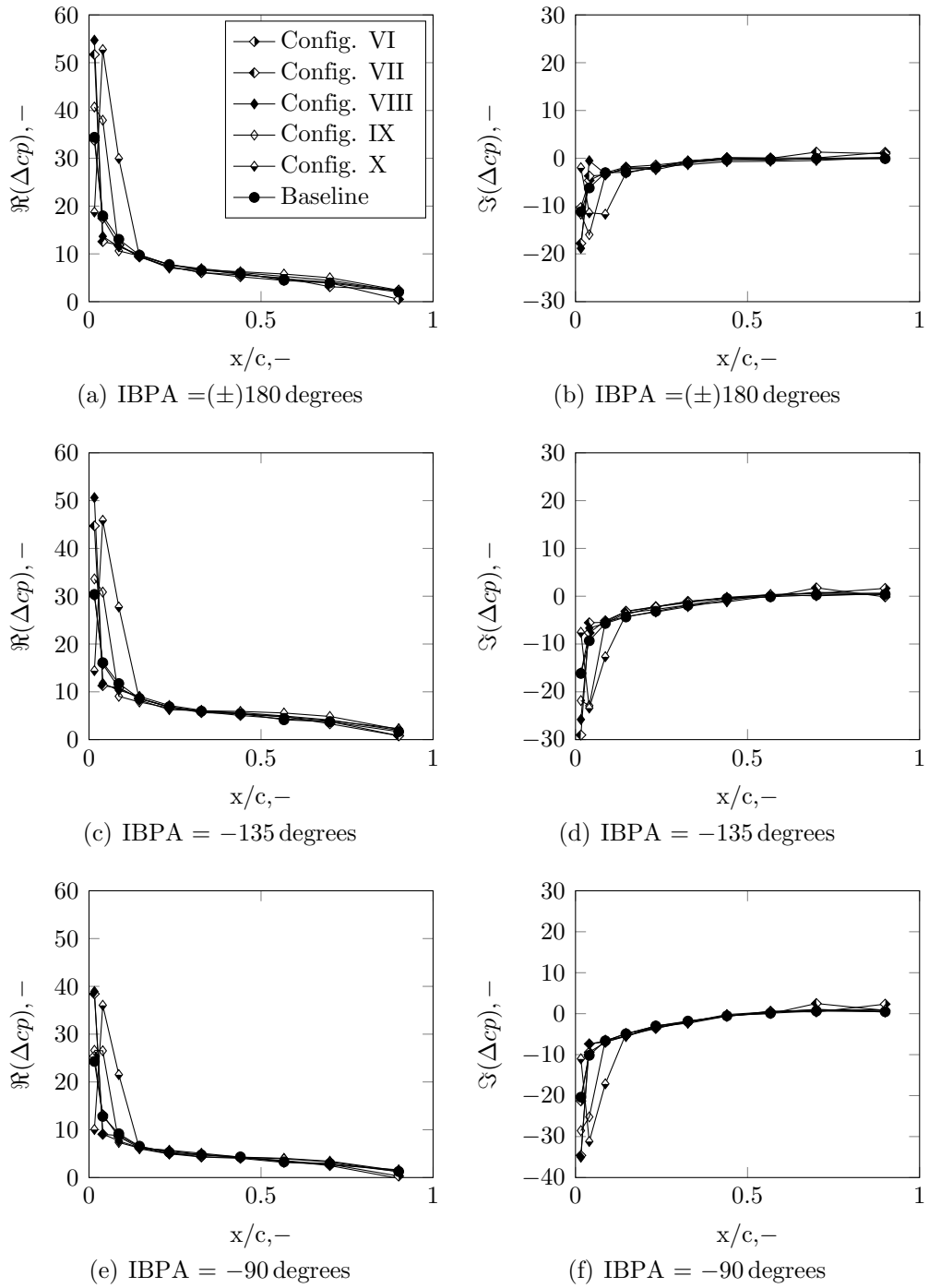


Figure 6.20: Variation of real and imaginary parts of unsteady pressure difference coefficient for an oscillation amplitude of $\hat{\alpha} = 0.5$ degrees at a reduced frequency of $k = 0.244$ (continued on the next page).

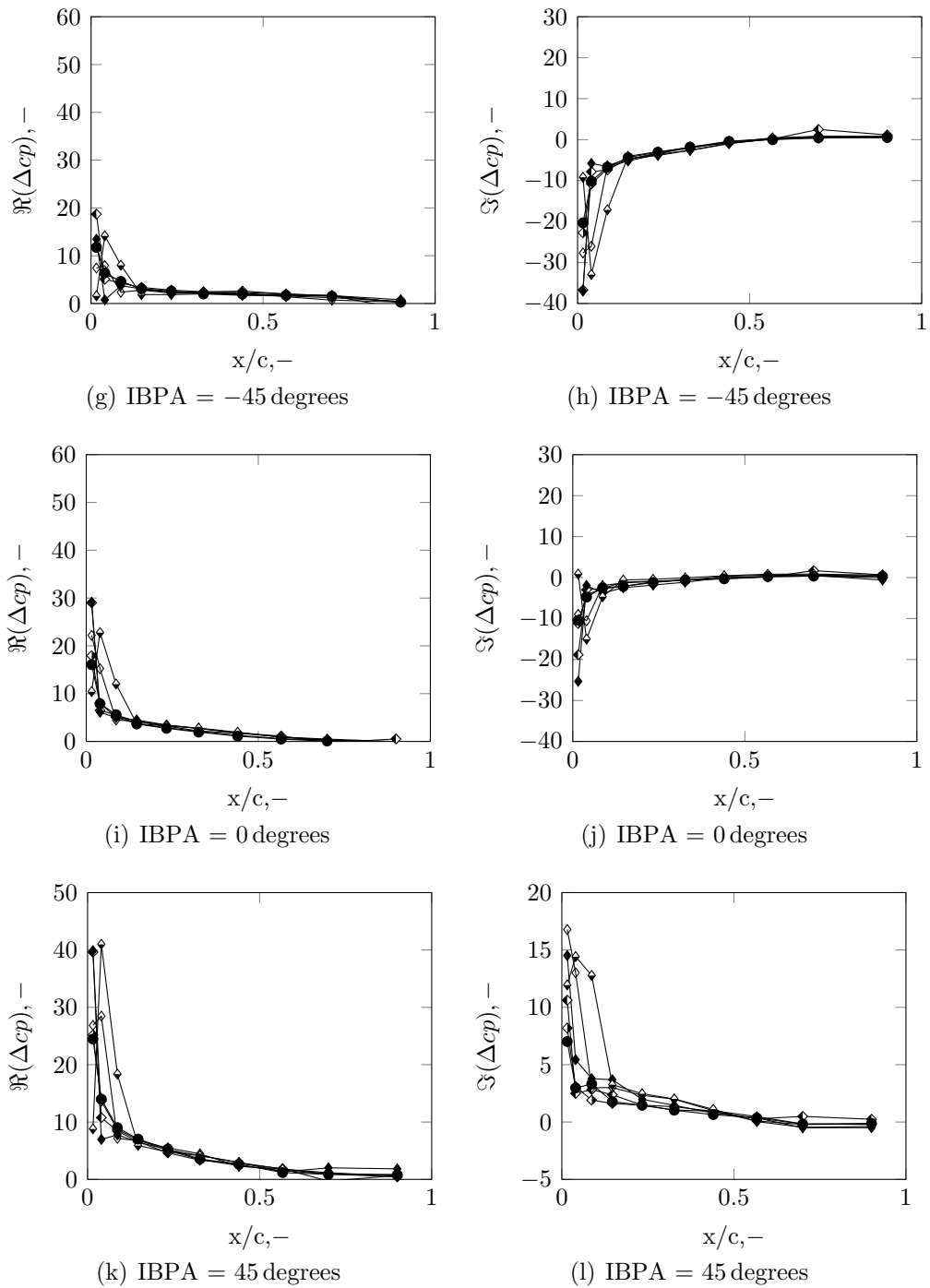


Figure 6.20: Variation of real and imaginary parts of unsteady pressure difference coefficient for an oscillation amplitude of $\hat{\alpha} = 0.5$ degrees at a reduced frequency of $k = 0.244$ (continued from the previous page).

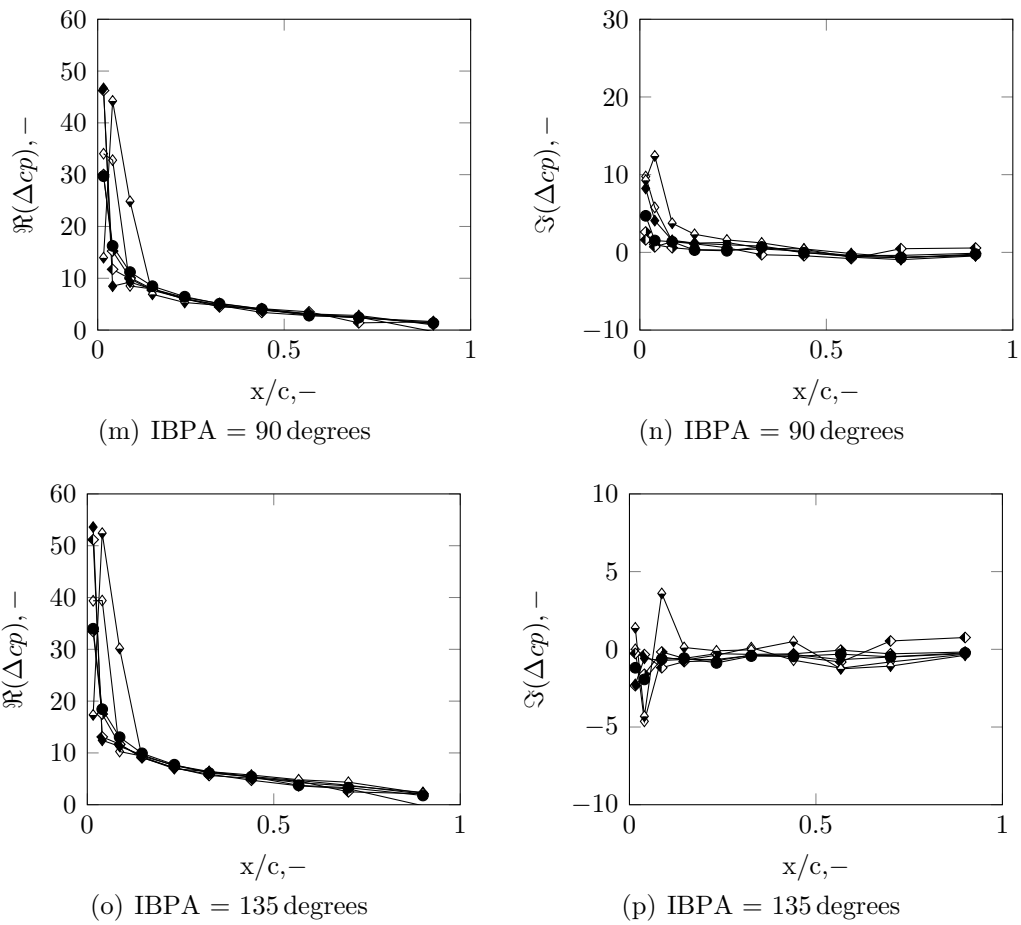


Figure 6.20: Variation of real and imaginary parts of unsteady pressure difference coefficient for an oscillation amplitude of $\hat{\alpha} = 0.5$ degrees at a reduced frequency of $k = 0.244$ (continued from the previous page).

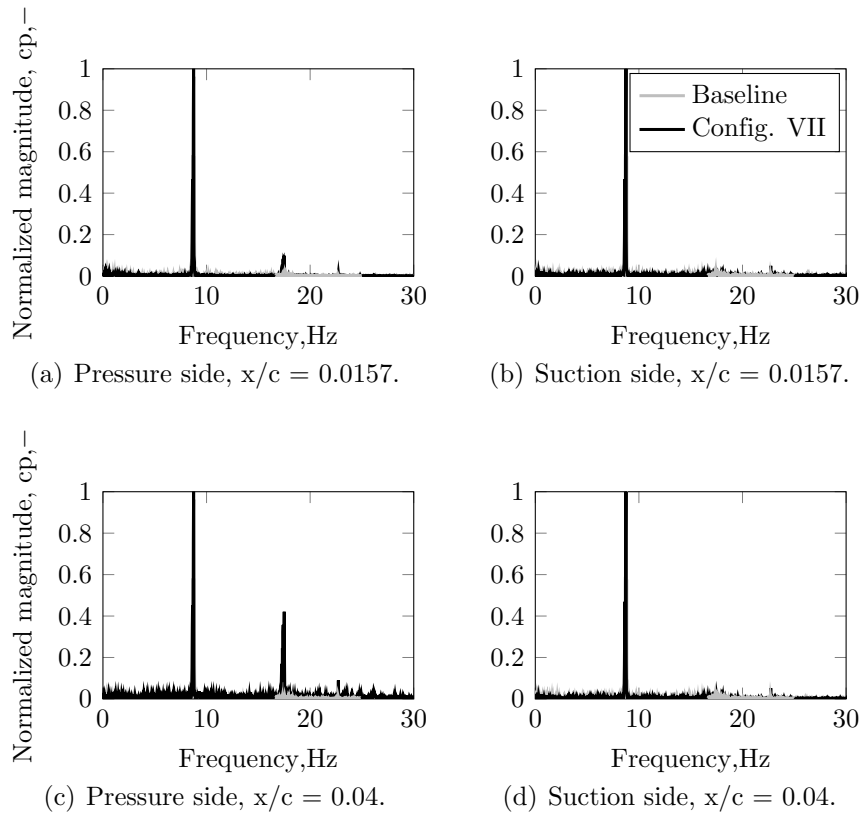


Figure 6.21: Normalized Fourier transform magnitudes of surface-pressure at IBPA = 135 degrees for different pressure tap locations.

Stability assessment

The aerodynamic damping of the five investigated cases is presented in figure 6.22 and displayed against the IBPA. The depicted data for $\sigma = \pm 180$ degrees correspond to one measurement. The aerodynamic damping is computed based on equation 5.15. A simplistic analysis, based on the leading edge Δcp as explained in section 6.3, can also be applied here. That suggests that the cascade is unstable for $\sigma = 45$ degrees and $\sigma = 90$ degrees featuring positive imaginary parts of Δcp at the blade front part for the presented cases, as noticed in the damping curve in figure 6.22. For the test cases with a stagger angle variation of $\Delta\gamma = -2$ degrees, the system becomes unstable for positive IBPAs, here $\sigma = 45, 90$ degrees and 135 degrees, whereas the remaining IBPAs are stable. The lowest damping is observed for $\sigma = 45$ degrees. The greatest changes are notable for the experiments with a stagger angle variation of $\Delta\gamma = -4$ degrees and $\Delta\gamma = -5$ degrees. By thinking at the damping curves as sinusoidal signals, it can be asserted that those at $\Delta\gamma = -4$ degrees and $\Delta\gamma = -5$ degrees show higher magnitudes and mean values are shifted upwards, compared to the remaining cases. The peak values result from the magnitudes of the unsteady moment coefficient, that are much bigger for the test case with alteration of $\Delta\gamma = -4$ degrees and $\Delta\gamma = -5$ degrees than for the other test cases. This finding is consistent with the results obtained in terms of real and imaginary part of Δcp .

In addition to the damping curve in figure 6.22, the phase angle between unsteady moment coefficient and blade displacement is illustrated in figure 6.23, and the relative change in amplitude of the unsteady moment coefficient compared to the baseline case in figure 6.24. For negative interblade phase angles, configuration X experiences the largest relative change in phase, i.e. -17% for IBPA $\sigma = -90$ degrees. For the remaining negative interblade phase angles and cases, the differences relative to the baseline configuration are smaller. For positive interblade phase angles, significant changes for configurations X are clearly visible. Namely, due to the increase in phase, the system becomes more unstable.

Smaller changes in amplitude of the unsteady moment coefficient are visible for configurations VI to VIII, compared to IX and X, with relative variations of up to 15% , see again figure 6.24. Most of the changes in amplitude of the unsteady moment coefficient are observed for the cases featuring the highest stagger angle variations, namely case IX and X. For these cases, the relative change is between 24% to 35% for case IX, and 70% to 83% for case X. By revisiting the damping curve in figure 6.22, the lowest damping occurs at IBPA $\sigma = 45$ degrees for case X, the phase changes relatively by 88% and the

amplitude of the unsteady moment coefficient by 83%. In comparison, for IBPA $\sigma = -45$ degrees, the phasing changes by -11% and the amplitude of $C_{m(c/2)}$ by 70% . In general, the change in phase is smaller than in amplitude for the presented cases for negative interblade phase angle and they stay stable compared to the baseline case.

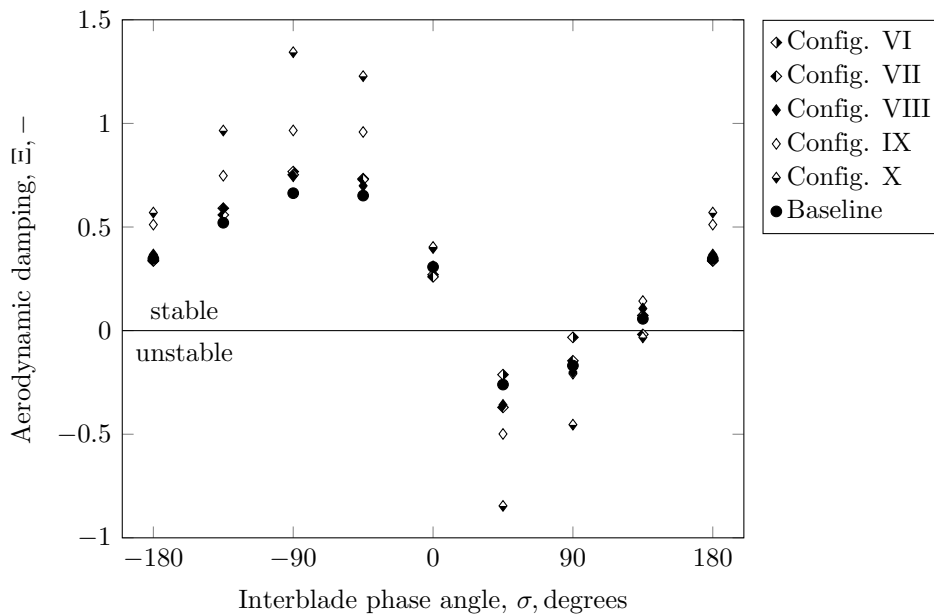


Figure 6.22: Aerodynamic damping for an oscillation amplitude of $\hat{\alpha} = 0.5$ degrees at a reduced frequency of $k = 0.244$.

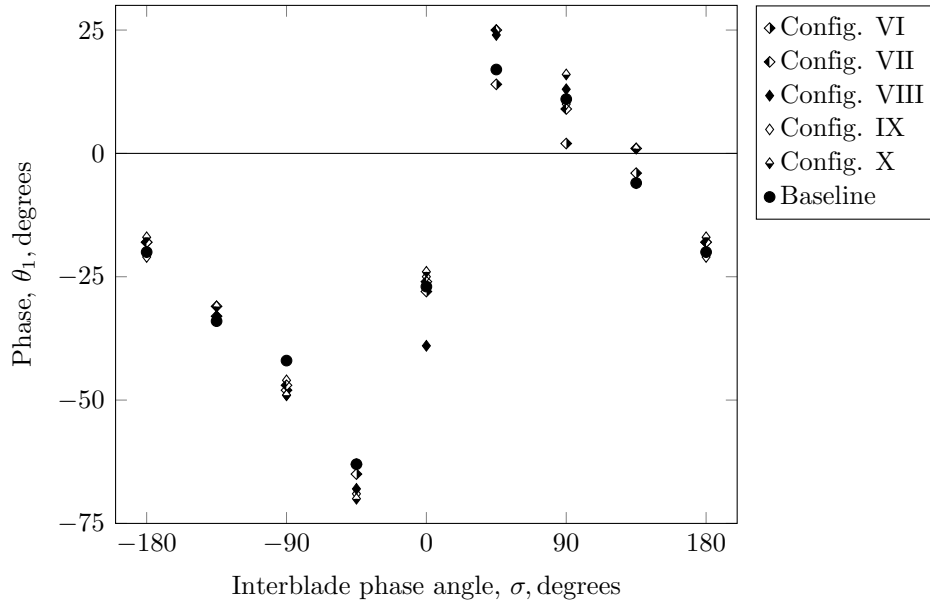


Figure 6.23: Phase angle between blade motion and unsteady moment coefficient, $C_{m1(c/2)}$, for an oscillation amplitude of $\hat{\alpha} = 0.5$ degrees at a reduced frequency of $k = 0.244$.

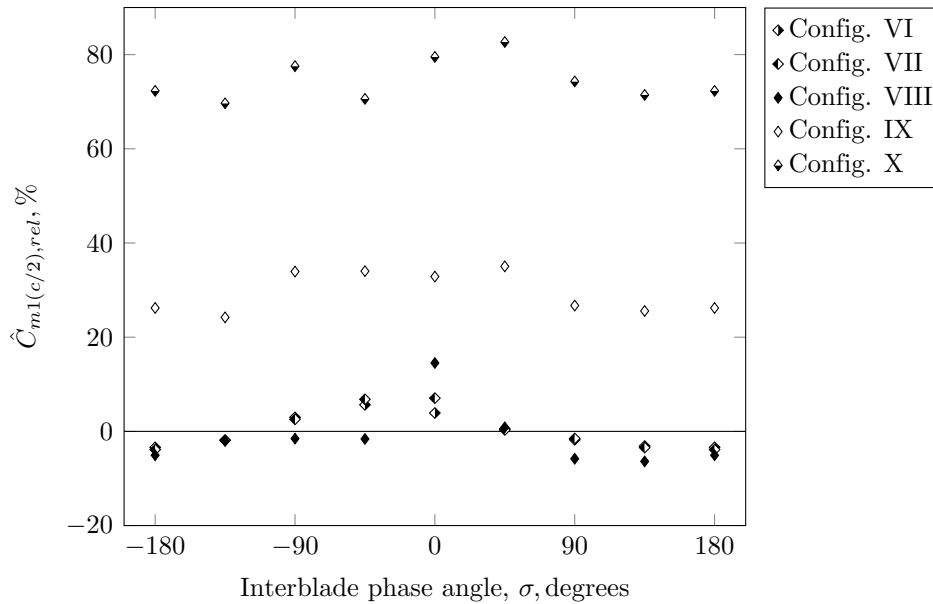


Figure 6.24: Relative change in amplitude of unsteady moment coefficient, $\hat{C}_{m1(c/2),rel}$, for an oscillation amplitude of $\hat{\alpha} = 0.5$ degrees at a reduced frequency of $k = 0.244$.

6.4.3 Comparison of one-blade, alternating, random and homogeneous pattern

This section aims to provide a comprehensive comparison between the studied mistuning patterns that were used in cluster I and II. This is shown exemplary for the configurations featuring a negative change in stagger angle variation of $\Delta\gamma = -2$ degrees. In figure 6.25, the real and imaginary parts are plotted versus the normalized x-coordinate for configuration II, IV and VII; recalling that configuration I is associated with the one-blade and configuration IV with the alternating mis-staggering pattern whereas for configuration VII a stagger angle variation for all blades in the cascade was introduced.

IBPA $\sigma = \pm 180$ degrees and $\sigma = 0$ degrees were chosen as they are associated with the minimum and maximum changes in unsteady pressure magnitudes compared to the remaining IBPA. IBPAs $\sigma = 45, 90$ and 0 degrees are featured as they are unstable. From the plots, it is noticeable that the unsteady aerodynamic response of the different cases exhibits a good agreement, indicating same stability characteristics. This is confirmed by revisiting the damping curve in figure 6.16 and 6.22, respectively. It can be reported that independently from the applied pattern, the unsteady pressure distributions of Δcp are very similar in terms of magnitude and phase for the three cases within same IBPAs. Apart from the major influence of the IBPA as illustrated and discussed in the previous section, the aerodynamic response at the leading edge is influenced additionally by the change of the axial pressure gradient introduced by the manipulation of the steady flow field through the stagger angle alteration.

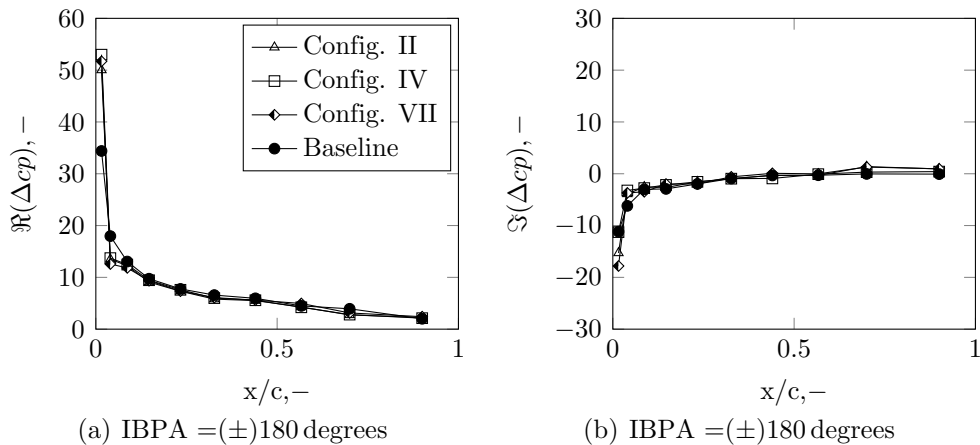


Figure 6.25: Variation of real and imaginary parts for an oscillation amplitude of $\hat{\alpha} = 0.5$ degrees at a reduced frequency of $k = 0.244$ for different mistuning patterns (continued on the previous page).

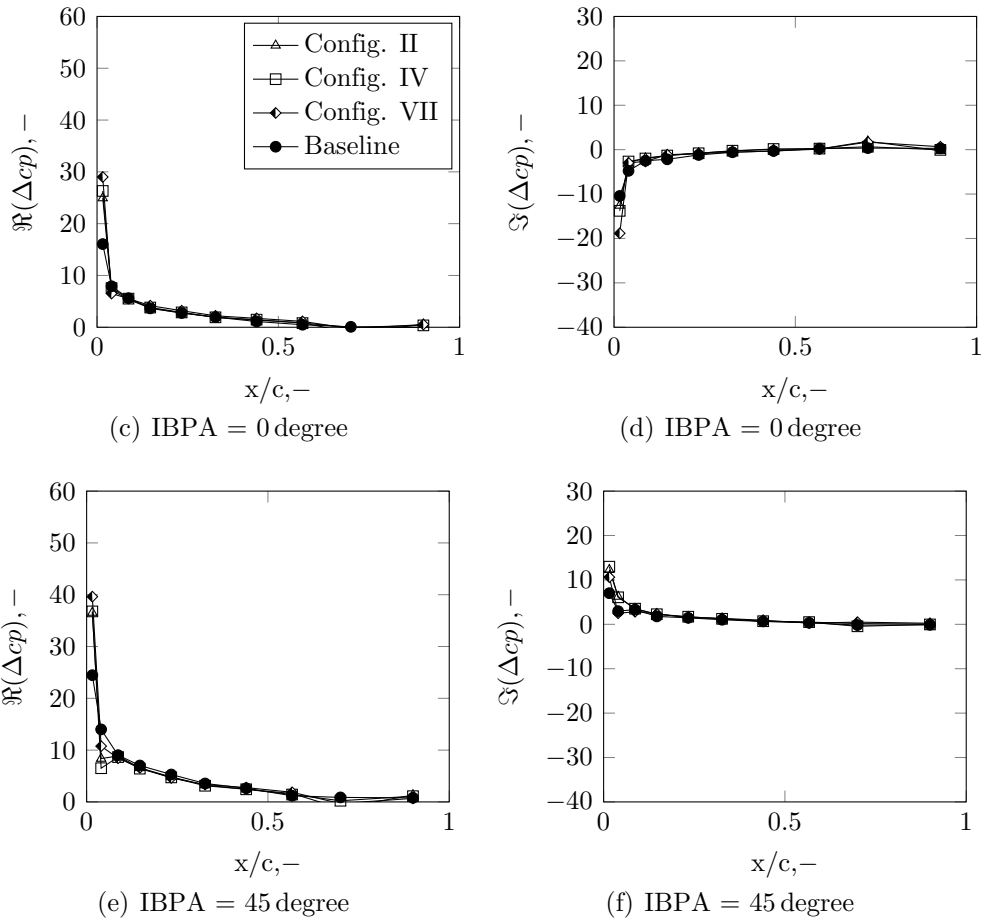
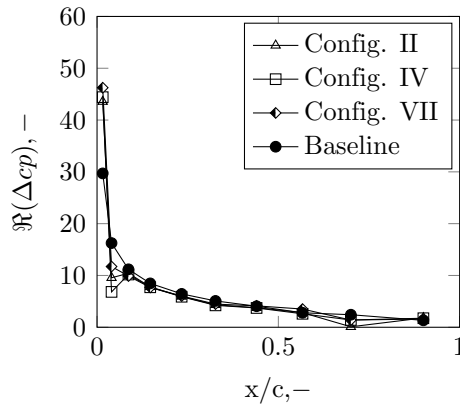
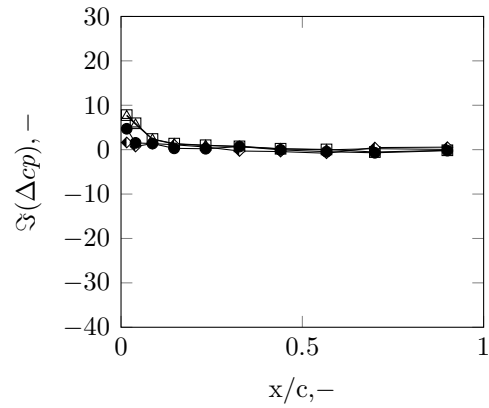


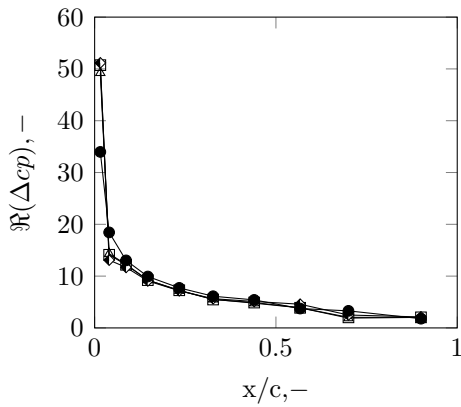
Figure 6.25: Variation of real and imaginary parts for an oscillation amplitude of $\hat{\alpha} = 0.5$ degrees at a reduced frequency of $k = 0.244$ for different mistuning patterns (continued from the previous page).



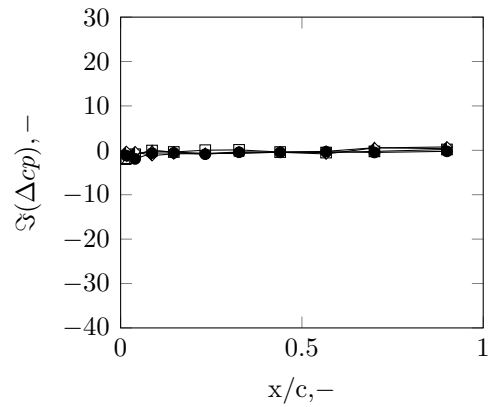
(g) IBPA = 90 degree



(h) IBPA = 90 degree



(i) IBPA = 135 degree



(j) IBPA = 135 degree

Figure 6.25: Variation of real and imaginary parts for an oscillation amplitude of $\hat{\alpha} = 0.5$ degrees at a reduced frequency of $k = 0.244$ for different mistuning patterns (continued from the previous page).

Chapter 7

Summary and Conclusion

This thesis investigated experimentally the influence of aerodynamic mistuning on flutter stability in a linear oscillating compressor cascade. It was aiming to contribute to an improved understanding of the cascade aerodynamics in the case of aerodynamic mistuning.

A test facility was set up and commissioned at Technische Universität Berlin in order to carry out the presented experiments. It consists of a wind tunnel and a measurement section incorporating a linear oscillating compressor cascade. The cascade is composed of eleven blades, nine of which are elastically suspended. The suspension is connected to a drive system, allowing the blades to oscillate sinusoidally in plunge or pitch. The facility is equipped with steady and unsteady measurement devices to monitor wind tunnel parameters and to acquire the aerodynamic response.

The experimental study is structured in three parts. First, the base flow has been investigated to provide a background to the work. The inlet flow was measured by using a hot wire anemometer for four different Mach and Reynolds numbers. The turbulence intensity was found to be low for the presented profiles, reaching a maximum value of 0.27% for the nethermost Mach number. Inlet velocity profiles were assessed for the same flow regimes. The profiles are fairly homogeneous but show a small bump which is associated with the velocity outlet profile of the radial blower. Steady pressure coefficients for the three central cascade blades were presented and shown to exhibit a good agreement. Second, the unsteady performance of the oscillating cascade was validated with data from literature. The parameters that were applied for the validation, such as reduced frequency, oscillation frequency and amplitude were chosen to be consistent with literature. A very good agreement with the experimental data was achieved, in the sense that all stable and unstable IBPA are in accordance with the reference. The third part of the experimental investigation deals with the analysis of the aerody-

dynamic response due to the aerodynamically mistuned oscillating cascade. The aerodynamic mistuning is realized by blade-to-blade stagger angle variations and consists of two clusters. In cluster I, the stagger angle of individual blades is altered and in cluster II, all blades in the cascade feature a stagger angle variation. Interblade phase angles ranging from $\sigma = -180$ degrees to $\sigma = +180$ degrees, with incremental steps of 45 degrees were studied for all configurations. The measurements were carried out at one reduced frequency and at a constant oscillation amplitude.

Cluster I features configurations in which the stagger angle of the cascade central blade is increased or decreased by $\Delta\gamma = \pm 2$ degrees; additionally, the same stagger angle is applied with an alternating pattern (i.e. every second blade) to the whole cascade. Also, a random pattern that applies alteration in the range of $\Delta\gamma = \pm 2$ degrees and $\Delta\gamma = \pm 1$ degree has been studied. From the computation of the aerodynamic damping, it can be noticed that the cascade is stable for the baseline case and the configurations with a positive stagger angle variation for all IBPAs, beside $\sigma = 45$ degrees and $\sigma = 90$ degrees. For the configuration with negative mis-staggering, IBPA $\sigma = 135$ degrees shifts from positive to negative damping, indicating an unstable system. This results from a phase shift from negative to positive of the pressure signal in the leading edge region, reflected by the positive imaginary part of the unsteady pressure different coefficient.

The characteristic of the damping curve for the random mistuning pattern does not change considerably compared to the baseline cases. Indeed, neither the phase, nor the magnitude of the unsteady pressure difference coefficient are altered remarkably.

In cluster II, all blades were mis-staggered to study if stability changes as for the cases in cluster I, in which individual blades were mistuned. Especially, negative stagger variations in cluster I, are found to be an interesting study case, since stability was changed. The stagger angle was varied from $\Delta\gamma = -1$ degree to $\Delta\gamma = -5$ degrees. The effect of the mistuning on the aerodynamics on the oscillating compressor cascade is that one single IBPA, namely $\sigma = 135$ degrees, the aerodynamic damping becomes negative for the cases VII and X compared to the baseline case. For the cases IX and X, featuring the most changes in stagger angle, the movement of the stagnation point affects significantly the unsteady blade pressure distribution at the blade front region. The unsteady moment coefficients increase significantly and differ among the investigated IBPAs by 11% for case IX and 13% for case X. Whereas, the changes in phasing are significantly higher for positive IBPAs. Indeed for case X, one IBPA shifts to negative damping compared to the baseline case.

For the tested configurations in cluster I and II, following conclusions can be drawn:

- the most unsteady pressure activity develops at the blade front region and a simplified stability assessment is possible by considering the sign of the imaginary part of the unsteady pressure coefficient in this region;
- the interblade phase angle affects significantly the unsteady blade pressure distribution and is not overruled by the manipulation of the steady flow field due the stagger angle variations;
- aerodynamic mistuning has a stabilizing or destabilizing influence on the cascade's aeroelastic stability, depending highly on the mistuning characteristic;
- for positive stagger angle variations, the damping curve is maintained in the sense that all unstable IBPA angles remain unstable;
- for small negative stagger angle changes (configuration II and IV), decreasing the area of the flow passage between the measurement blade (pressure side) and its neighboring blade, the system becomes more unstable;
- for large negative stagger angle variations, $\Delta\gamma = -4, 5$ degrees, the aerodynamic damping characteristic is only marginally affected in terms of stable or unstable IBPAs. However, the amplitude of the S-shaped damping curve rises, being a compound effect of a change in phase and unsteady moment coefficient.

Based on the current results, especially negative stagger angle variations can influence aeroelastic stability. In off-design operations, in which unwanted negative incidence might occur, not only aerodynamic efficiency is decreased. Aeroelastic stability will be degraded as well and has to be evaluated carefully. For IBPAs with very low positive aerodynamic damping, a safety margin depending on, e.g. manufacturer and assembly tolerances, altering the flow passage, should be applied. Future investigations should include mistuning in combinations with different reduced frequencies, blade geometries and oscillation amplitudes.

Bibliography

- [1] Y. El-Aini, R. DeLanauville, A. Stoner, and V. Capece. High cycle fatigue of turbomachinery components - Industry perspective. In *33rd Joint Propulsion Conference and Exhibit*, Reston, Virginia, jul 1997.
- [2] E. McLaughlin, B. Todd, and J. Jones. *NTSB: Engine in deadly Southwest jet incident missing a fan blade*. <https://edition.cnn.com/2018/04/17/us/philadelphia-southwest-flight-emergency-landing/index.html>, Accessed 2018-04-20.
- [3] Y. C. Fung. *An Introduction to the Theory of Aeroelasticity*. Dover Publication, Inc., 1993.
- [4] A. R. Collar. The Expanding Domain of Aeroelasticity. *Journal of the Royal Aeronautical Society*, 50(428):613--636, aug 1946.
- [5] H. Hennings. *Flutter investigations on a Finite Linear 2d Compressor Cascade in a Wind Tunnel in incompressible Flow*. Phd thesis, RWTH Aachen, 1997.
- [6] M. May. *Linearized Flutter Investigations of Mistuned Turbomachinery Blading*. Phd thesis, Technische Universität Berlin, Germany, 2012.
- [7] W. Sachs. *On Flutter Behaviour of a 2-D Compressor Cascade in Incompressible Flow*. Phd thesis, RWTH Aachen, 1991.
- [8] R. Bisplinghoff, H. Ashley, and R. Halfman. *Aeroelasticity*. Dover Publication, Inc., Mineola, New York, 1996.
- [9] F. Rottmeier. *Experimental investigation of a vibrating axial turbine cascade in presence of upstream generated aerodynamic gusts*. Phd thesis, EPFL, Lausanne, Switzerland, 2003.
- [10] K. Y. Billah and R. H. Scanlan. Resonance, Tacoma Narrows bridge failure, and undergraduate physics textbooks. *American Journal of Physics*, 59(2):118--124, feb 1991.

-
- [11] E. Dowell, editor. *A Modern Course in Aeroelasticity*. Springer, 5th edition, 2015.
- [12] M. F. Platzer and F. O. Carta, editors. *AGARD Manual on Aeroelasticity in Axial-Flow Turbomachines - Volume 1, Unsteady Turbomachinery Aerodynamics*. Advisory Group for Aerospace Research and Development, AGARDograph No.298, 1987.
- [13] H. Stargardter. Subsonic/Transonic Stall Flutter Study. Technical report, Final Report, NASA CR-165256, PWA 5517-31, 1979.
- [14] P. Duquesne, Q. Rendu, S. Aubert, and P. Ferrand. Choke flutter instability sources tracking with linearized calculations. *International Journal of Numerical Methods for Heat & Fluid Flow*, jan 2019.
- [15] S. Fleeter. Aeroelasticity Research for Turbomachine Applications. *Journal of Aircraft*, 16(5):320--326, may 1979.
- [16] Willy J. G. Bräunling. *Flugzeugtriebwerke*. Springer Berlin Heidelberg, Berlin, Heidelberg, 2001.
- [17] J. S. Rao. *Turbomachine Blade Vibration*. New Age International (P) Limited, New Dehli, India, 1st edition, 1991.
- [18] A. V. Srinivasan. Flutter and Resonant Vibration Characteristics of Engine Blades. *Journal of Engineering for Gas Turbines and Power*, 119(4):742--775, 1997.
- [19] O. Bendiksen. Flutter of Mistuned Turbomachinery Rotors. *Journal of Engineering for Gas Turbines and Power*, 106(1):25 -- 33, 1984.
- [20] E. F. Crawley and K. C. Hall. Optimization and Mechanisms of Mistuning in Cascades. *Journal of Engineering for Gas Turbines and Power*, 107(2):418 -- 426, 1985.
- [21] J. Dugundji and D. J. Bundas. Flutter and forced response of mistuned rotors using standing wave analysis. *AIAA Journal*, 22(11):1652--1661, nov 1984.
- [22] D. J. Ewins. The effects of detuning upon the forced vibrations of bladed disks. *Journal of Sound and Vibration*, 9(1):65--79, jan 1969.
- [23] K. V. Kaza and R. Kielb. Flutter and Response of a Mistuned Cascade in Incompressible Flow. *AIAA Journal*, 20(8):1120--1127, aug 1982.
- [24] D. Hoyniak and S. Fleeter. Aerodynamic Detuning Analysis of an Unstalled Supersonic Turbofan Cascade. *Journal of Engineering for Gas Turbines and Power*, 108(1):60 -- 67, 1986.

-
- [25] I. Sladojevic, A. I. Sayma, and M. Imregun. Influence of Stagger Angle Variation on Aerodynamic Damping and Frequency Shifts. In *Proceedings of ASME Turbo Expo 2007: Power for Land, Sea and Air*, Montreal, Canada, May 14-17, 2007.
- [26] K. Ekici, R. Kielb, and K. C. Hall. Aerodynamic Asymmetry Analysis of Unsteady Flows in Turbomachinery. *Journal of Turbomachinery*, 132(1):011006 (11), 2010.
- [27] K. C. Ekici, R. Kielb, and K. C. Hall. The effect of aerodynamic asymmetries on turbomachinery flutter. *Journal of Fluids and Structures*, 36:1--17, jan 2013.
- [28] H. Triebstein. Unsteady Pressure on a Harmonically Oscillating Staggered Cascade in Incompressible and Compressible Flow. *Revue Française de Mécanique*, (numéro spécial):115--122, 1976.
- [29] F. O. Carta and A. O. St.Hilaire. Effect of Interblade Phase Angle and Incidence Angle on Cascade Pitching Stability. *Journal of Engineering for Power*, 102(2):391--396, 1980.
- [30] F. Lane. System Mode Shapes in the Flutter of Compressor Blade Rows. *Journal of the Aeronautical Sciences*, 23(1):54--66, jan 1956.
- [31] F. O. Carta. Coupled Blade-Disk-Shroud Flutter Instabilities in Turbojet Engine Rotors. *Journal of Engineering for Gas Turbines and Power*, 89(3):419--426, jul 1967.
- [32] F. O. Carta. Unsteady Aerodynamics and Gapwise Periodicity of Oscillating Cascaded Airfoils. *Journal of Engineering for Power*, 105(3):565--574, 1983.
- [33] F. O. Carta. An Experimental Investigation of Gapwise Periodicity and Unsteady Aerodynamic Response in an Oscillating Cascade. Technical report, NASA Contractor Report 3513, United Technologies Research Center, East Hartford, Connecticut, USA, 1982.
- [34] M. Mayorca. *Numerical methods for turbomachinery aeromechanical predictions*. Phd thesis, Royal Institute of Technology (KTH), Sweden, 2011.
- [35] A.V. Srinivasan, D. G. Cutts, and S. Sridhar. Turbojet Engine Blade Damping. Technical report, NAS3-21708 contract report, 1981.
- [36] J. J. Kielb and R. S. Abhari. Experimental Study of Aerodynamic and Structural Damping in a Full-Scale Rotating Turbine. *Journal of Engineering for Gas Turbines and Power*, 125(1):102--112, jan 2003.

-
- [37] A. Meldahl. Self-induced flutter of wings with one degree of freedom. *Brown Boveri Review*, 33(12):386–393, 1946.
- [38] N. Cumpsty. *Compressor aerodynamics*. Krieger Publishing Company, Malabar, Florida, 2004.
- [39] D. Vogt. *Experimental Investigation of Three-Dimensional Mechanisms in Low-Pressure Turbine Flutter*. Phd thesis, Royal Institute of Technology (KTH), Sweden, 2005.
- [40] S. R. Manwaring, D. C. Rabe, C. B. Lorence, and A. R. Wadia. Structures and Dynamics Committee Best Paper of 1996 Award: Inlet Distortion Generated Forced Response of a Low-Aspect-Ratio Transonic Fan. *Journal of Turbomachinery*, 119(4):665–676, oct 1997.
- [41] E. Crawley. Aeroelastic Formulations for Turbomachines Propellers. In M.F. Platzer and F.O. Carta, editors, *AGARD Manual on Aeroelasticity in Axial-Flow Turbomachines - Volume 2, Structural Dynamics and Aeroelasticity*, chapter 19. Advisory Group for Aerospace Research and Development, AGARDograph No.298, 1988.
- [42] D. H. Buffum and S. Fleeter. Wind Tunnel Wall Effects in a Linear Oscillating Cascade. *Journal of Turbomachinery*, 115(1):147–156, 1993.
- [43] A. Bölcs and T. H. Fransson. Aeroelasticity in Turbomachines - Comparison of theoretical and experimental results. *Communication du Laboratoire de Thermique Appliquée et de Turbomachines de l'Ecole Polytechnique Fédérale de Lausanne*, 13, 1986.
- [44] E. Széchényi. Fan Blade Flutter: Single Blade Instability or Blade to Blade Coupling? In *Proceedings of ASME 1985 : International Gas Turbine Conference and Exhibit. Volume 1: Aircraft Engine; Marine; Turbomachinery; Microturbines and Small Turbomachinery*, Houston, Texas, USA, March 18–21, 1985.
- [45] Y. Hanamura, H. Tanaka, and K. Yamaguchi. A Simplified Method to Measure Unsteady Forces Acting on the Vibrating Blades in Cascade. *Bulletin of JSME*, 23(180):880–887, 1980.
- [46] D. H. Buffum and S. Fleeter. Oscillating cascade aerodynamics by an experimental influence coefficient technique. *Journal of Propulsion and Power*, 6(5):612–620, sep 1990.
- [47] S. Fleeter, A. S. Novick, R. E. Riffel, and J. E. Caruthers. An Experimental Determination of the Unsteady Aerodynamics in a Controlled Oscillating Cascade. *Journal of Engineering for Power*, 99(1):88–96, 1977.

-
- [48] F. O. Carta and A. O. St.Hilaire. Experimentally Determined Stability Parameters of a Subsonic Cascade Oscillating Near Stall. *Journal of Engineering for Power*, 100(1):111 -- 120, 1978.
- [49] J. Verdon and J. Caspar. Subsonic Flow Past an Oscillating Cascade with Finite Mean Flow Deflection. *AIAA Journal*, 18(5):540--548, may 1980.
- [50] A. Bölcs. A Test Facility for the Investigation of Steady and Unsteady Transonic Flows in Annular Cascades. In *Proceedings of ASME 1983 : International Gas Turbine Conference and Exhibit*, Phoenix, Arizona, USA, March 27–31, 1983.
- [51] A. Bölcs and D. Schläfli. Flutter Phenomena in a Transonic Turbine Cascade. In *Unsteady Aerodynamics of Turbomachines and Propellers*, pages 411-- 425, Cambridge, UK, September 24–27, 1984.
- [52] J. Belz and H. Hennings. Experimental Flutter Investigations of an Annular Compressor Cascade: Influence of Reduced Frequency on Stability. In K. C. Hall, R. Kielb, and J. P. Thomas, editors, *Unsteady Aerodynamics, Aeroacoustics and Aeroelasticity of Turbomachines*, pages 77--91. Springer, 2006.
- [53] A. Vega, R. Corral, A. Zanker, and P. Ott. Experimental and Numerical Assessment of the Aeroelastic Stability of Blade Pair Packages. In *Proceedings of ASME Turbo Expo 2014: Turbine Technical Conference and Exposition*, Düsseldorf, Germany, June 16-20, 2014.
- [54] D. H. Buffum, V. R. Capece, A. J. King, and Y. M. EL-Aini. Oscillating Cascade Aerodynamics at Large Mean Incidence. *Journal of Turbomachinery*, 120(1):122--130, 1998.
- [55] C. A. Poensgen and H. E. Gallus. Experimental Investigation of the Unsteady Pressure Field on a Vibrating Blade in Steady and Unsteady Flow. In H. M. Atassi, editor, *Unsteady Aerodynamics, Aeroacoustics, and Aeroelasticity of Turbomachines and Propellers*. Springer, New York, NY, 1993.
- [56] D. L. Bell and L. He. Three Dimensional Unsteady Pressure Measurements for an Oscillating Turbine Blade. In *Proceedings of ASME 1997 International Gas Turbine and Aeroengine Congress and Exhibition*, Orlando, Florida, June 2-5, 1997.
- [57] D. L. Bell and L. He. Three-Dimensional Unsteady Flow for an Oscillating Turbine Blade and the Influence of Tip Leakage. *Journal of Turbomachinery*, 122(1):93--101, 2000.

-
- [58] K. K. Frey and S. Fleeter. Oscillating Airfoil Aerodynamics of a Rotating Compressor Blade Row. *Journal of Propulsion and Power*, 17(2):232--239, 2001.
- [59] D. Vogt and T. H. Fransson. A New Turbine Cascade for Aeromechanical Testing. In *The 16th Symposium on Measuring Techniques in Transonic and Supersonic Flow in Cascades and Turbomachines*, pages 1--8, Cambridge, UK, September, 23-24, 2002.
- [60] N. Glodic, D. Vogt, and T. H. Fransson. Experimental and Numerical Investigation of Mistuned Aerodynamic Influence Coefficients in an Oscillating LPT Cascade. In *Proceedings of ASME Turbo Expo 2011*, Vancouver, British Columbia, Canada, June 6-10, 2011.
- [61] M. C. Keerthi, S. Shubham, and A. Kushari. Aerodynamic Influence of Oscillating Adjacent Airfoils in a Linear Compressor Cascade. *AIAA Journal*, 55(12):4113--4126, dec 2017.
- [62] M. C. Keerthi and A. Kushari. Experimental Study of Aerodynamic Damping of an Annular Compressor Cascade With Large Mean Incidences. *Journal of Turbomachinery*, 141(6):061002 (17), 2019.
- [63] C. E. Seeley, C. Wakelam, X. Zhang, D. Hofer, and W. Ren. Investigations of Flutter and Aerodynamic Damping of a Turbine Blade: Experimental Characterization. *Journal of Turbomachinery*, 139(8):081011 (7), 2017.
- [64] V. Slama, A. Macalka, J. Ira, P. Eret, V. Tsymbalyuk, and B. Rudas. Experimental and CFD Investigation of Aerodynamic Forces and Moments in a Linear Turbine Blade Cascade. In *Proceedings of ASME International Mechanical Engineering Congress and Exposition*, Pittsburgh, PA, US, November 9-15, 2018.
- [65] T. H. Fransson and J. M. Verdon. Updated Report on Standard Configurations for Unsteady Flow Through Vibrating Axial-Flow Turbomachine Cascades. Technical report, KTH Stockholm, UTRC, 1991.
- [66] M. F. Platzer and F.O. Carta, editors. *AGARD Manual on Aeroelasticity in Axial-Flow Turbomachines - Volume 2, Structural Dynamics and Aeroelasticity*. Advisory Group for Aerospace Research and Development, AGARDograph No.298, 1988.
- [67] R. L. Maltby. Flow Visualization in Wind Tunnels using Indicators. Technical report, AGARDograph 70, Royal Aircraft Establishment, Bedford, England, 1962.

-
- [68] H. H. Bruun. *Hot-wire Anemometry: Principles and Signal Analysis*. Oxford University Press, New York, 1995.
- [69] W. Nitsche and A. Brunn. *Strömungsmesstechnik*. Springer Verlag, Berlin, Heidelberg, Germany, 2006.
- [70] C. G. Lomas. *Fundamentals of Hot Wire Anemometry*. Cambridge University Press, Cambridge, UK, 2011.
- [71] S. Keil. *Technology and Practical Use of Strain Gages: With Particular Consideration*. Wilhelm Ernst & Sohn, Berlin, Germany, 2017.
- [72] William M. Murray and William R. Miller. *The Bonded Electrical Resistance Strain Gage: An Introduction*. Oxford University Press, New York, USA, 1992.
- [73] R. L. Hannah and S. E. Reed, editors. *Strain Gage Users' Handbook*. Springer Netherlands, 1992.
- [74] C. Klein, W. Sachs, U. Henne, and J. Borbye. Determination of Transfer Function of Pressure-Sensitive Paint. In *48th AIAA Aerospace Sciences Meeting Including the New Horizons Forum and Aerospace Exposition, Aerospace Sciences Meetings*, Orlando, Florida, USA, January 4 - 7, 2010.
- [75] M. G. Bulmer. *Principles of Statistics*. Dover Publication, Inc., Edinburgh, UK, 1979.
- [76] R. Barlow. *Statistics: A Guide to the Use of Statistical Methods in the Physical Sciences*. John Wiley & Sons Ltd., Chichester, UK, 1989.
- [77] S. B. Pope. *Turbulent Flows*. Cambridge University Press, Cambridge, 2000.
- [78] T. Veerarajan. *Probability, Statistics And Random Processes*. Tata McGraw-Hill Publishing Company Limited, New Dehli, India, 2002.
- [79] C. Bailly and G. Comte-Bellot. *Turbulence*. Experimental Fluid Mechanics. Springer International Publishing Switzerland, 2015.
- [80] F. O. Carta and C. F. Niebanck. Prediction of Rotor Instability at High Forward Speeds, Volume III, Stall Flutter. Technical report, USA AVLABS Technical Report 68-180, U.S. Army Aviation Materiel Laboratories, Fort Eustis, Virginia, USA, 1969.

-
- [81] M. Gonzalez Hernandez, A. Moreno Lopez, A. Jarzabek, J. Perales Perales, Y. Wu, and S. Xiaoxiao. Design Methodology for a Quick and Low-Cost Wind Tunnel. In *Wind Tunnel Designs and Their Diverse Engineering Applications*. InTech, mar 2013.
- [82] E. Arrington and J. Gonsalez. Flow Quality Improvements in the NASA Lewis Research Center 9- by 15-Foot Low Speed Wind Tunnel. In *31st AIAA/ASME/SAE/ASEE Joint Propulsion Conference and Exhibit*, San Diego, CA, July 10-12, 1995.
- [83] H. Rietschel and H. Esdorn, editors. *Raumklimatechnik*. Springer, Berlin, Heidelberg, 1994.
- [84] F. K. Owen and A. K. Owen. Measurement and assessment of wind tunnel flow quality. *Progress in Aerospace Sciences*, 44(5):315--348, jul 2008.
- [85] E. Malkiel and R. E. Mayle. Transition in a Separation Bubble. *Journal of Turbomachinery*, 118(4):752--759, oct 1996.
- [86] L. Malzacher, S. Geist, V. Motta, D. Peitsch, and H. Hennings. A Low-Speed Compressor Test Rig for Flutter Investigations. *Journal of Turbomachinery*, 141(5), may 2019.
- [87] T. Lee and Y. Y. Su. Surface Pressures Developed on an Airfoil Undergoing Heaving and Pitching Motion. *Journal of Fluids Engineering*, 137(5):(051105) 1--11, may 2015.
- [88] V. Motta and G. Quaranta. Linear Reduced-Order Model for Unsteady Aerodynamics of an L-Shaped Gurney Flap. *Journal of Aircraft*, 52(6):1887--1904, nov 2015.
- [89] R. Huang and C. Lin. Vortex shedding and shear-layer instability of wing at low-Reynolds numbers. *AIAA Journal*, 33(8):1398--1403, aug 1995.
- [90] J. G. Leishman. *Principles of Helicopter Aerodynamics*. Cambridge University Press, New York, USA.
- [91] V. Motta, A. Guardone, and G. Quaranta. Influence of airfoil thickness on unsteady aerodynamic loads on pitching airfoils. *Journal of Fluid Mechanics*, 774:460--487, jul 2015.
- [92] DEWETRON GmbH. *DAQP Isolated Universal Input Module, Manufacturer Data Sheet*. <https://www.dewetron.com>, Date accessed: 2019-07-28.

-
- [93] DEWETRON GmbH. *DEWE-ORION A/D Boards, Manufacturer Data Sheet*. <https://www.dewetron.com>, Date accessed: 2019-07-28.
- [94] Joint Committee for Guides in Metrology. JCGM 100:2008 - Evaluation of measurement data - Guide to the expression of uncertainty in measurement. Technical report, BIPM. GUM 1995 with minor corrections., 2008.
- [95] ELECTRO - MATION GmbH. *Pitot tubes Type L, Manufacturer Data Sheet*. <http://www.electro-mation.de/staurohre.html>, Date accessed: 2019-07-28.
- [96] halstrup-walcher GmbH. *KAL 84 Manufacturer Data Sheet*. <https://www.halstrup-walcher.de/de/produkte/alle-produkte/KAL-84.php>, Date accessed: 2019-07-28.
- [97] J. R. Taylor. *An introduction to error analysis: The study of uncertainties in physical measurements*. University Science Books (US), 2 edition, 1997.
- [98] Jerrit Dähnert. *Aktive Beeinflussung der laminaren Ablösung mithilfe pneumatischer Wirbelgeneratoren*. Phd thesis, Technische Universität Berlin, 2012.
- [99] TSI Inc. *TSI Thermal Anemometry Catalog*. <https://www.tsi.com>, Date accessed: 2019-07-28.
- [100] National Instruments. *National Instruments: NI 6229 Device Specifications, Manufacturer Data Sheet*. <http://www.ni.com/pdf/manuals/375204c.pdf>, Date accessed: 2019-07-28.
- [101] Hottinger Baldwin Messtechnik GmbH. *Strain gauges and accessories, Manufacturer Datasheet*. <https://www.hbm.com>, Date accessed: 2019-07-28.
- [102] National Instruments. *National Instruments: Measuring Strain with Strain Gages, White paper*. <https://www.ni.com>, Date accessed: 2019-07-28, 2016.
- [103] Deutsches Institut für Normung. DIN EN 60751: Industrial platinum resistance thermometer sensors, 2009.
- [104] Honeywell International Inc. Honeywell Sensing and Control: Pressure Transducer Accuracy in Application. Technical report, Technical Note, Honeywell, 2004.

- [105] Meggitt (Orange County) Inc. *8510B -1,-2,-5 Piezoresistive pressure transducer, Manufacturer Data Sheet*. <https://endevco.com/>, Date accessed: 2019-07-28.
- [106] Setra Systems Inc. *Setra Model 264 pressure transducer, Manufacturer Data Sheet*. <https://www.setra.com>, Date accessed: 2019-07-28.
- [107] Setra Systems Inc. *Setra Model 270 pressure transducer, Manufacturer Data Sheet*. <https://www.setra.com>, Date Accessed: 2019-07-28.

List of Figures

1.1	Collar’s aeroelastic triangle, adapted from Ref. [8].	3
1.2	Campbell diagram, adapted from Ref. [9].	3
1.3	Axial compressor stability map illustrating main flutter types and their regions of occurrence, adapted from Ref. [12].	5
2.1	Modal displacement for a bladed disc with N=8 with nodal diameter 2. The grey filled circles indicate the blade positions.	8
4.1	Wind tunnel with a linear oscillating compressor cascade for aeroelastic investigation at the Chair for Aero Engines at TU Berlin.	23
4.2	Outline of the measurement section.	25
4.3	Cascade geometrical parameters.	25
4.4	Elastic blade suspension with blade. 1 Support frame; 2 Support ring; 3 Mounting plate; 4 Plunging plate; 5 Balancing mass; 6 Rotary disk; 7 Strain gauges; 8 Lemo connector; 9 Motor support; 10 Stepper motor; 11 Crank shaft.	27
4.5	Degrees of freedom of the blade suspension (adapted from Ref.[5]).	27
4.6	Pictures of the blade suspensions in the free flutter configuration (without measurement equipment).	28
4.7	Strain gauge signal of cascade central suspension; blade oscillates at 9 Hz in pitch in quiescent air.	28
4.8	Constant Temperature Circuit Diagram, adapted from Ref. [69].	31
4.9	Foil strain gauge, adapted from Ref. [71].	32
4.10	Wheatstone bridge circuit, adapted from Ref. [73].	33
4.11	Pressure tap distribution on the blade surface.	34
4.12	Profile geometry.	34
4.13	Characteristic calibration curves of a tube system in a measurement blade for the first pressure tap location counting from the leading edge on the suction side.	35
4.14	Hot wire measurement chain.	37
4.15	Blade surface pressure and strain gauge measurement chain.	38

6.1	Measurement grid, for hot wire measurements, in the inlet of the test section.	47
6.2	Normalized velocity profiles at three different y-locations for several Reynolds (Re) numbers in the inlet of the test section.	49
6.3	Turbulence intensity at three different y-locations for several Reynolds (Re) numbers in the inlet of the test section.	50
6.4	Oil flow visualization for different Reynolds numbers at a mean angle of attack of $\alpha_0 = 2$ degrees.	52
6.5	Steady pressure coefficient chordwise distribution at a mean angle of $\alpha_0 = 2$ degrees.	52
6.6	Variation of Real and Imaginary parts of unsteady pressure difference coefficient for a mean angle of attack of $\alpha_0 = 2$ degrees and an oscillation amplitude of $\hat{\alpha} = 0.5$ degrees at a reduced frequency of $k = 0.144$ (continued on the next page).	54
6.6	Variation of Real and Imaginary parts of unsteady pressure difference coefficient for a mean angle of attack of $\alpha_0 = 2$ degrees and an oscillation amplitude of $\hat{\alpha} = 0.5$ degrees at a reduced frequency of $k = 0.144$ (continued from the previous page).	55
6.7	Change in flow passage area for an interblade phase angle of $\sigma = 180$ degrees - only the five central blades of the cascade are illustrated. Black blades illustrate the baseline configuration, grey ones, the blades oscillating out of phase.	56
6.8	Variation of Real and Imaginary parts of unsteady pressure difference coefficient for a mean angle of attack of $\alpha_0 = 2$ degrees and an oscillation amplitude of $\hat{\alpha} = 0.5$ degrees at a reduced frequency of $k = 0.144$	57
6.9	Ensemble phase averaged unsteady pressure coefficient on pressure and suction side, cp , and its difference, Δcp , for different chordwise position; at a mean angle of attack of $\alpha_0 = 2$ degrees, an oscillation amplitude of $\hat{\alpha} = 0.5$ degrees and an IBPA of $\sigma = 0$ degrees at a reduced frequency of $k = 0.144$ (continued on the next page).	58
6.9	Ensemble phase averaged unsteady pressure coefficient on pressure and suction side, cp , and its difference, Δcp , for different chordwise positions; at a mean angle of attack of $\alpha_0 = 2$ degrees, an oscillation amplitude of $\hat{\alpha} = 0.5$ degrees and an IBPA of $\sigma = 90$ degrees at a reduced frequency of $k = 0.144$ (continued from the previous page).	59

6.9	Ensemble phase averaged unsteady pressure coefficient on pressure and suction side, cp , and its difference, Δcp , for different chordwise positions; at a mean angle of attack of $\alpha_0 = 2$ degrees and an oscillation amplitude of $\hat{\alpha} = 0.5$ degrees and an IBPA of $\sigma = 180$ degrees at a reduced frequency of $k = 0.144$ (continued from the previous page).	60
6.10	Aerodynamic damping at a mean angle of attack of $\alpha_0 = 2$ degrees and an oscillation amplitude of $\hat{\alpha} = 0.5$ degrees at a reduced frequency of $k = 0.144$	62
6.11	Phase angle between unsteady moment coefficient, $C_{m1(c/2)}$, and blade displacement at a mean angle of attack of $\alpha_0 = 2$ degrees and an oscillation amplitude of $\hat{\alpha} = 0.5$ degrees at a reduced frequency of $k = 0.144$	62
6.12	Unsteady moment coefficient, $C_{m(c/2)}$, computed from ensemble phase averaged pressure data, at a mean angle of attack of $\alpha_0 = 2$ degrees for different IBPAs and an oscillation amplitude of $\hat{\alpha} = 0.5$ degrees at a reduced frequency of $k = 0.144$	63
6.13	Cluster I - steady pressure coefficient chordwise distribution on the cascade central blade for baseline and mistuned configurations.	67
6.14	Variation of real and imaginary parts of unsteady pressure difference coefficient for an oscillation amplitude of $\hat{\alpha} = 0.5$ degrees at a reduced frequency of $k = 0.244$ (continued on the next page).	70
6.14	Variation of real and imaginary parts of unsteady pressure difference coefficient for an oscillation amplitude of $\hat{\alpha} = 0.5$ degrees at a reduced frequency of $k = 0.244$ (continued from the previous page).	71
6.14	Variation of real and imaginary parts of unsteady pressure difference coefficient for an oscillation amplitude of $\hat{\alpha} = 0.5$ degrees at a reduced frequency of $k = 0.244$ (continued from the previous page).	72
6.15	Normalized Fourier transform magnitudes of surface-pressure at IBPA = 135 degrees at a reduced frequency of $k = 0.244$	73
6.16	Aerodynamic damping for an oscillation amplitude of $\hat{\alpha} = 0.5$ degrees at a reduced frequency of $k = 0.244$	75
6.17	Phase angle between unsteady moment coefficient, $C_{m1(c/2)}$, and blade displacement for an oscillation amplitude of $\hat{\alpha} = 0.5$ degrees at a reduced frequency of $k = 0.244$	77
6.18	Relative change in amplitude of unsteady moment coefficient, $\hat{C}_{m1(c/2),rel}$, for an oscillation amplitude of $\hat{\alpha} = 0.5$ degrees at a reduced frequency of $k = 0.244$	77

6.19	Steady pressure coefficient chordwise distribution on the cascade central blade for baseline and mistuned configurations.	78
6.20	Variation of real and imaginary parts of unsteady pressure difference coefficient for an oscillation amplitude of $\hat{\alpha} = 0.5$ degrees at a reduced frequency of $k = 0.244$ (continued on the next page).	81
6.20	Variation of real and imaginary parts of unsteady pressure difference coefficient for an oscillation amplitude of $\hat{\alpha} = 0.5$ degrees at a reduced frequency of $k = 0.244$ (continued from the previous page).	82
6.20	Variation of real and imaginary parts of unsteady pressure difference coefficient for an oscillation amplitude of $\hat{\alpha} = 0.5$ degrees at a reduced frequency of $k = 0.244$ (continued from the previous page).	83
6.21	Normalized Fourier transform magnitudes of surface-pressure at IBPA = 135 degrees for different pressure tap locations.	84
6.22	Aerodynamic damping for an oscillation amplitude of $\hat{\alpha} = 0.5$ degrees at a reduced frequency of $k = 0.244$	86
6.23	Phase angle between blade motion and unsteady moment coefficient, $C_{m1(c/2)}$, for an oscillation amplitude of $\hat{\alpha} = 0.5$ degrees at a reduced frequency of $k = 0.244$	87
6.24	Relative change in amplitude of unsteady moment coefficient, $\hat{C}_{m1(c/2),rel}$, for an oscillation amplitude of $\hat{\alpha} = 0.5$ degrees at a reduced frequency of $k = 0.244$	87
6.25	Variation of real and imaginary parts for an oscillation amplitude of $\hat{\alpha} = 0.5$ degrees at a reduced frequency of $k = 0.244$ for different mistuning patterns (continued on the previous page).	88
6.25	Variation of real and imaginary parts for an oscillation amplitude of $\hat{\alpha} = 0.5$ degrees at a reduced frequency of $k = 0.244$ for different mistuning patterns (continued from the previous page).	89
6.25	Variation of real and imaginary parts for an oscillation amplitude of $\hat{\alpha} = 0.5$ degrees at a reduced frequency of $k = 0.244$ for different mistuning patterns (continued from the previous page).	90
A.1	Experimental investigation part I - Normalized Fourier transform magnitudes of surface-pressure at IBPA = 135 degrees for different pressure tap locations (continued on the next page).A-2	

A.1	Experimental investigation part I - Normalized Fourier transform magnitudes of surface-pressure at IBPA = 135 degrees for different pressure tap locations (continued from the previous page).	A-3
A.1	Experimental investigation part I - Normalized Fourier transform magnitudes of surface-pressure at IBPA = 135 degrees for different pressure tap locations (continued from the previous page).	A-4
A.2	Experimental investigation part II - Normalized Fourier transform magnitudes of surface-pressure at IBPA = 135 degrees for different pressure tap locations (continued from the previous page).	A-5
A.2	Experimental investigation part II - Normalized Fourier transform magnitudes of surface-pressure at IBPA = 135 degrees for different pressure tap locations (continued from the previous page).	A-6
A.2	Experimental investigation part II - Normalized Fourier transform magnitudes of surface-pressure at IBPA = 135 degrees for different pressure tap locations (continued from the previous page).	A-7
B.1	Schematic of a pitot-static-tube, showing interior probe structure as well as stagnation pressure p_t , static pressure p and dynamic pressure q .	B-4
B.2	Computer-added design scheme of the modified calibration device; (1) mounting support; (2) blade suspension; (3) Lemo connector to data acquisition system; (4) micrometer screws; (5) center of rotation for calibration of the torsional springs.	B-9
B.3	Schematic sketch of calibration device for plunge mode	B-10
B.4	Illustration of the trigonometric relationships used in calibrating the strain gauge.	B-10
B.5	Illustration of the geometric relations for calibrating the strain gauge's pitch mode	B-12

List of Tables

1.1	Parameter list that influence the flutter mechanism.	6
4.1	Geometrical parameters of the wind tunnel.	24
4.2	Cascade parameters.	24
4.3	Pressure tap locations.	34
6.1	Test matrix (cluster I and II) for a blade in sinusoidal motion with an oscillation amplitude of $\hat{\alpha} = 0.5$ and a reduced frequency of $k = 0.244$	45
6.2	Measured turbulence intensity levels at the different Mach and associated Reynolds numbers.	47
6.3	Comparison of cascade parameters.	53
B.1	Accuracy of data acquisition and conversion devices, from [92], [93]	B-4
B.2	Influence parameters and sensitivity coefficients for calibration of strain gauges' plunge mode	B-11
B.3	Additional uncertainty influences for pitch displacement calibration	B-12
B.4	Relative uncertainties influencing DMS measurements.	B-13
B.5	Relative uncertainties for unsteady pressure measurements.	B-15
B.6	Relative errors for Setra 264 sensor.	B-16
B.7	Relative errors for Setra 270 sensor.	B-16

Appendix A

Frequency plots

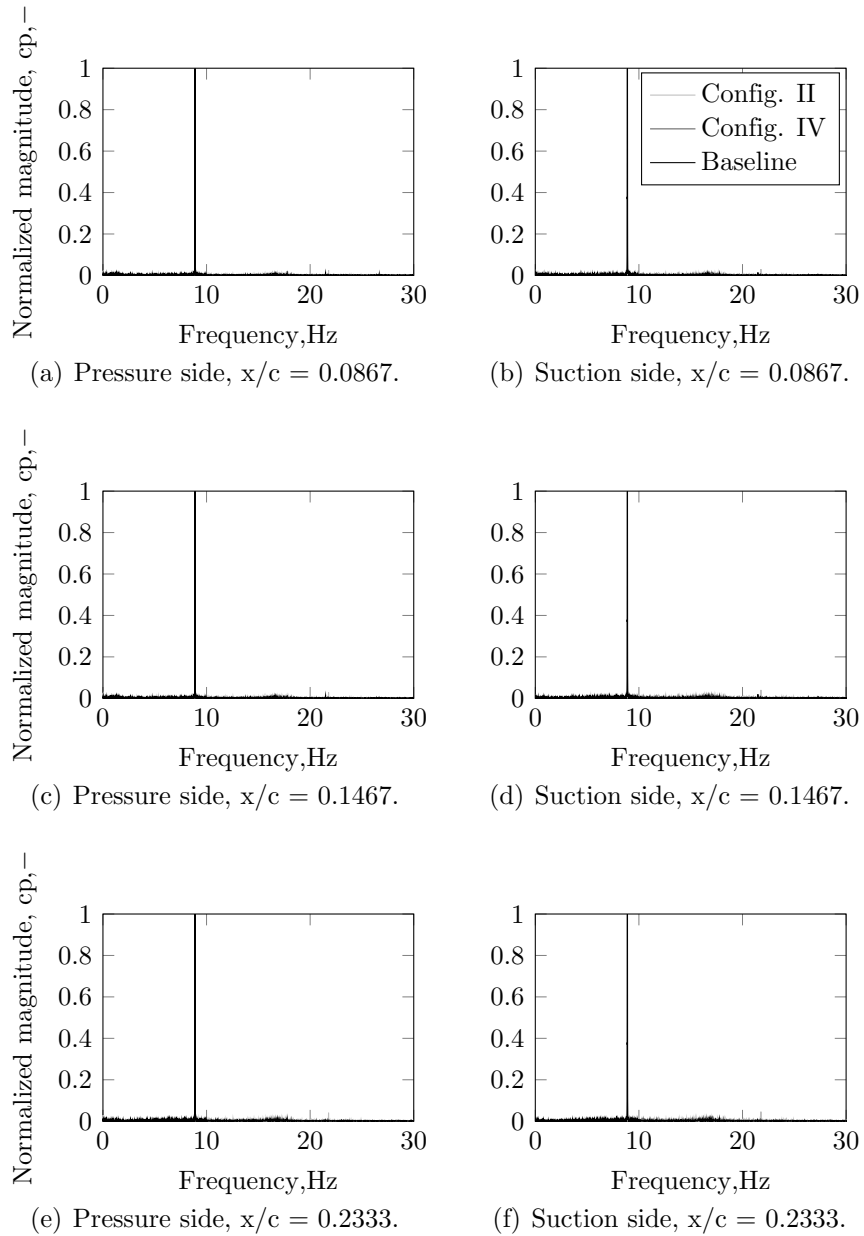


Figure A.1: Experimental investigation part I - Normalized Fourier transform magnitudes of surface-pressure at IBPA = 135 degrees for different pressure tap locations (continued on the next page).

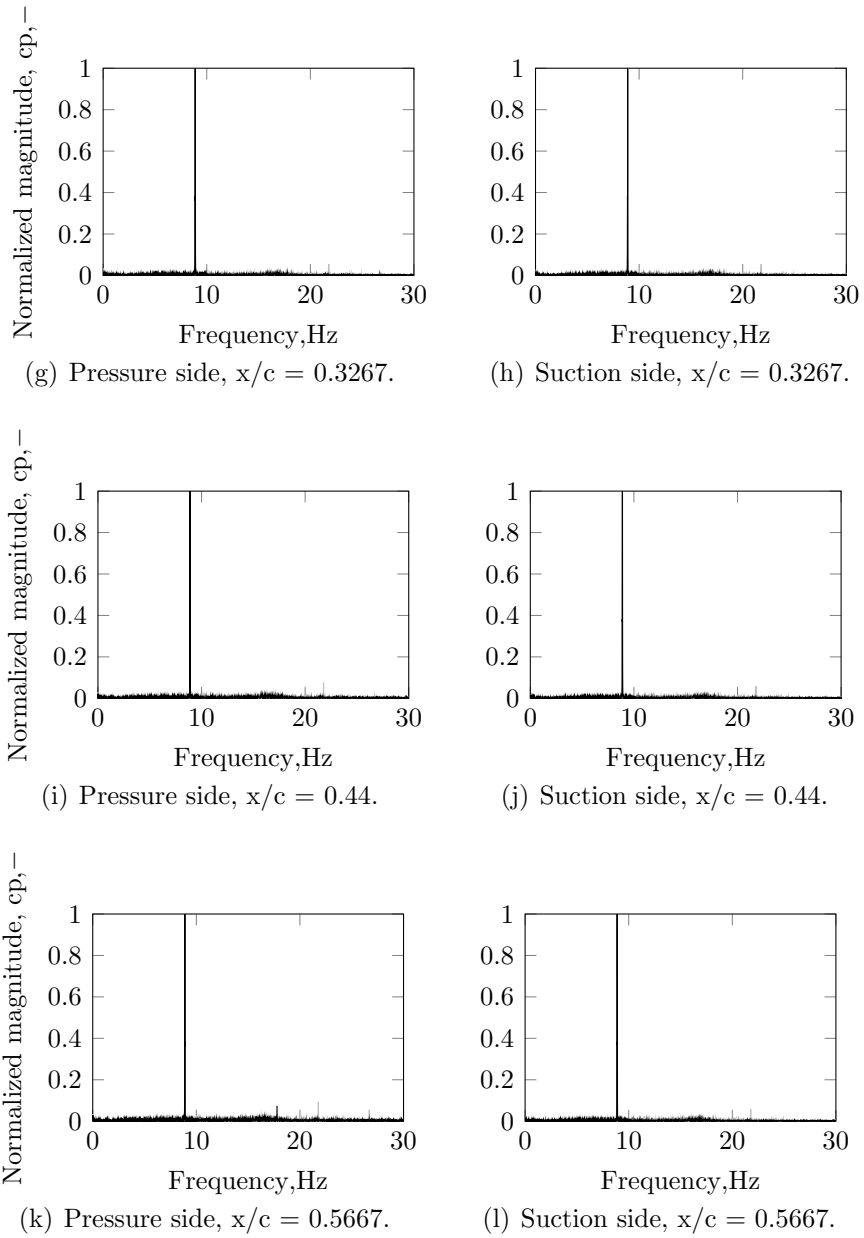


Figure A.1: Experimental investigation part I - Normalized Fourier transform magnitudes of surface-pressure at IBPA = 135 degrees for different pressure tap locations (continued from the previous page).

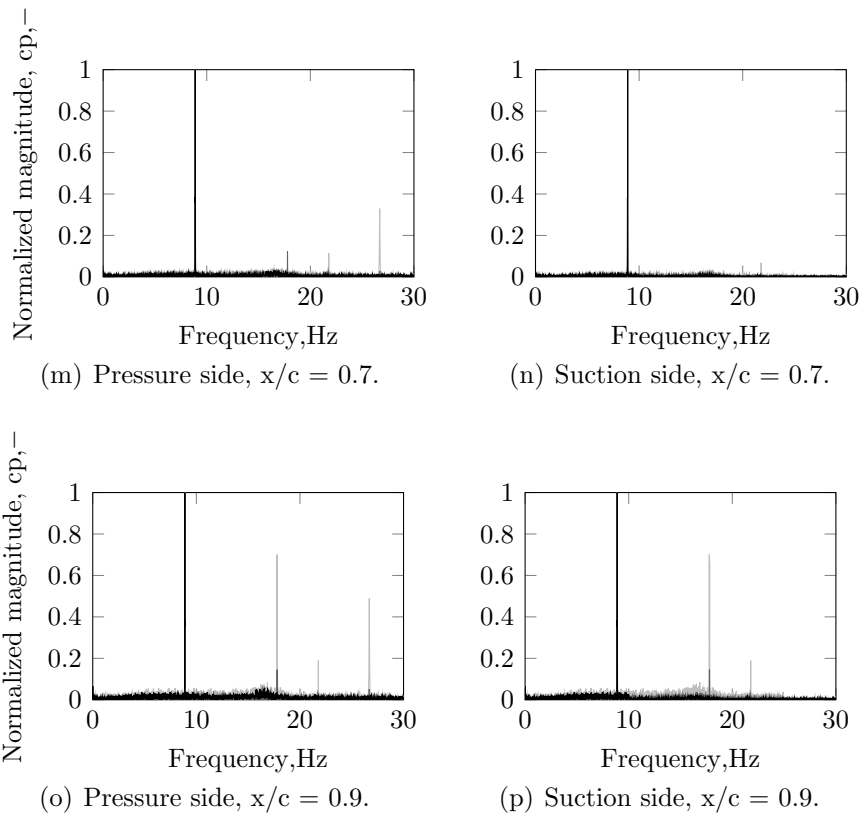


Figure A.1: Experimental investigation part I - Normalized Fourier transform magnitudes of surface-pressure at IBPA = 135 degrees for different pressure tap locations (continued from the previous page).

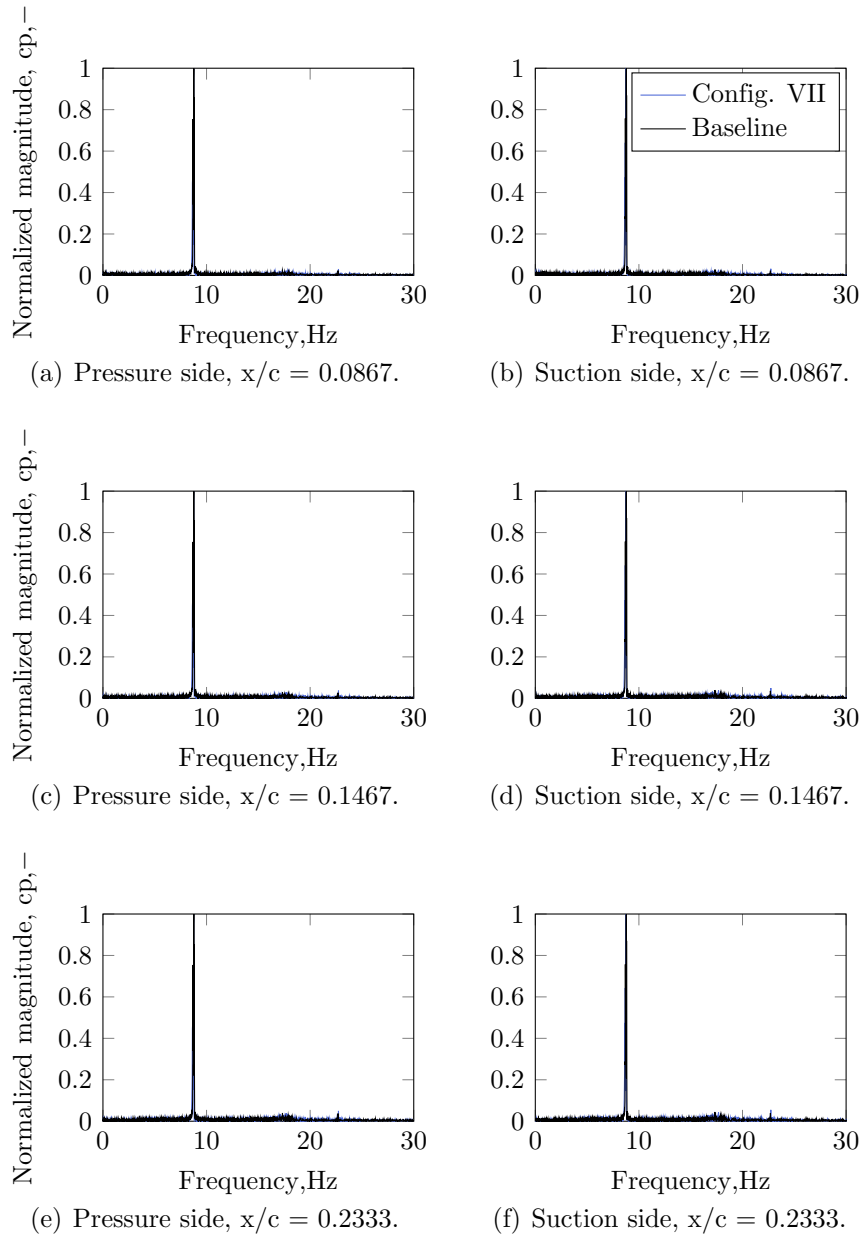


Figure A.2: Experimental investigation part II - Normalized Fourier transform magnitudes of surface-pressure at IBPA = 135 degrees for different pressure tap locations (continued from the previous page).

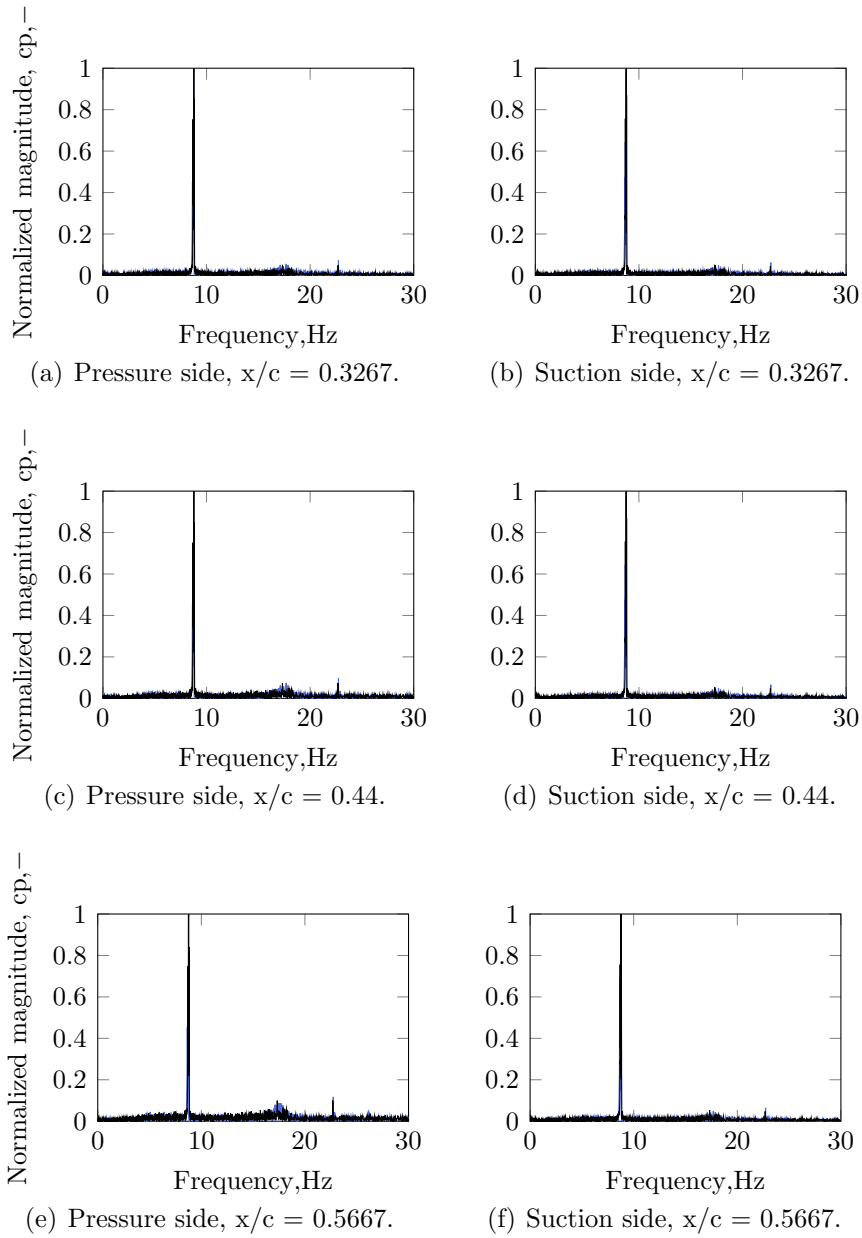


Figure A.2: Experimental investigation part II - Normalized Fourier transform magnitudes of surface-pressure at IBPA = 135 degrees for different pressure tap locations (continued from the previous page).

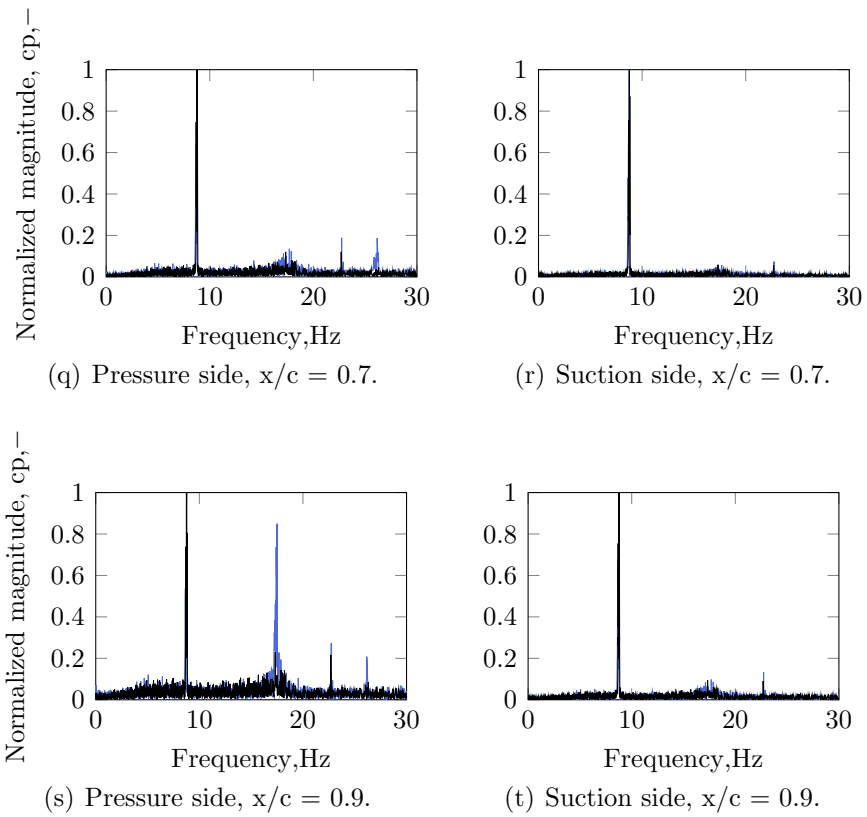


Figure A.2: Experimental investigation part II - Normalized Fourier transform magnitudes of surface-pressure at IBPA = 135 degrees for different pressure tap locations (continued from the previous page).

Appendix B

Measurement Uncertainty

B.1 Methodology

Depending on the physical quantity under consideration and the technology used to measure it, uncertainty is introduced into the results from different sources and via various pathways. The following text will give a brief explanation of the nature of measurement uncertainty for the measurement technology considered in each chapter, accompanied by calculations concerning the specific equipment used on the aeroelastic test rig.

Where possible, a full type A uncertainty analysis was performed, calculating statistical parameters such as standard deviations and confidence intervals based on repeated empirical observations: In such a *Type A evaluation*, the best estimate for the expected value of a randomly varying quantity is calculated as the arithmetic mean of n observations, which can then be used to calculate the experimental standard deviation and variance [94]. In many cases, however, manufacturer information regarding errors and uncertainty had to be relied on to determine total uncertainty along the measurement chain. This method is known as a *Type B evaluation*, in which the variance of a quantity is not established by repeated observations. Rather, using scientific judgement based on all available information is employed to arrive at a satisfactory estimate of uncertainty. Such information may include data from previous measurements, calibration certificates or general knowledge regarding the behaviour of instruments and materials [94].

B.2 Total Uncertainty

Scientific measurements are generally affected by various influences that decrease their accuracy. Examples may include deviations in the ambient conditions, the non-linearity of a sensor response curve or the resolution of a device used for converting an analogue signal into a digital one. Thus, to

achieve a satisfactory level of confidence about the range in which the true value of a measured quantity might fall, the various sources of uncertainty must be combined into a single value representing the total uncertainty. This is usually done by statistical methods:

Having obtained the standard uncertainties σ_i associated with all relevant influence parameters, i.e. the uncertainty of a result expressed as a standard deviation, one may compute a *combined standard uncertainty* to arrive at an estimate for the range in which the output value can be expected to lie. Such a computation will correspond to a typical confidence interval at the level of one standard deviation, meaning the real or true value of the measurand has a probability of 68 % of falling into the specified interval.

In many cases, it can be useful to apply a *coverage factor* K to these values in order to expand the confidence interval. For quantities that are assumed to obey a normal distribution, one might typically choose a coverage factor of 2 or 3, corresponding to confidence intervals of 95 % and 99.7% respectively. In some cases, it is more reasonable to assume that a quantity obeys a uniform distribution, i.e. all values within the relevant interval are equally likely to occur.

The total *expanded combined standard uncertainty* is then computed from standard uncertainties and coverage factors as a Root Square Sum, giving a final estimate of the uncertainty that can be expected for the respective measured quantity [94]:

$$\sigma_{\Sigma} = K \cdot \sqrt{\sum_{i=1}^N \left[\frac{1}{K_i} \cdot \sigma_i \right]^2}. \quad (\text{B.1})$$

If individual and overall coverage factors are disregarded, i.e. a confidence interval of one standard deviation is considered sufficient, this expression simplifies to the combined standard uncertainty:

$$\sigma_{\Sigma} = \sqrt{\sum_{i=1}^N \sigma_i^2}. \quad (\text{B.2})$$

Along a measurement chain, the quantities of interest are often functions of other measurands. In this case, so called *sensitivity coefficients* must be taken into account. These are the partial derivatives of the function for the final measurand with respect to the different influence quantities, and thus describe how the output estimate varies with changes in the values of the input estimates:

$$\sigma_{\Sigma} = \sqrt{\sum_{i=1}^N \left[\left(\frac{\partial f}{\partial x_i} \right)^2 \sigma_i^2 \right]}, \quad (\text{B.3})$$

where f is the functional relationship of the final measurand to the various input quantities. An example of this would be a velocity measurement using a Pitot probe, where one actually measures a dynamic pressure q , and the velocity is then given as a function of dynamic pressure and air density. In many cases however, this relationship cannot be specified by such a precise mathematical function and must be determined experimentally or approximated. Often, this involves assuming a linear dependency, in which cases the expression again simplifies to the basic Root Square Sum formula (B.2) .

B.3 Accuracy of Signal Conditioning and A/D-Conversion

All measurement data collected at the aeroelastic test rig is stored and processed digitally on a computer. However, because the measurement devices in use here usually transmit their output as analogue voltage signals, there is a need to first condition and filter these signals before they can be converted into digital signals and then transferred to the computer. This is achieved with the use of a modular data acquisition system (*DEWE-50-PCI-32*) which combines both signal conditioning (Typ: DAQST-STG input module) and A/D-conversion (Typ: ORION-1624-200) modules into a single device.

Both signal conditioning and A/D-conversion are not perfectly accurate processes, and thus will introduce some error into the acquired signals. This error is the result of various influences like system noise, temperature drift or imperfections in the electronic components. While system noise is inherent to the devices' function and thus is given as absolute value in the specifications, deviations in non-linearity, gain and offset of the system's characteristic are subject to change depending on many variables. As such, they are usually calculated as a percentage of current reading or input voltage range.

Because of this, no generally applicable estimate for the error associated with the data acquisition and analog-digital conversion devices can be given here. Instead, their influence along each measurement chain must be calculated in accordance with the respective voltage ranges and readings.

Table B.1 summarises these specifications, enabling the inaccuracy associated with the data acquisition (DAQ) to be calculated. Note that the ORION-1624 converter has a 24-bit resolution and thus the quantization error is relatively small compared to other influences. Consequently, it is summarised into the reading-dependent gain error by the manufacturer.

Other common error sources in data acquisition boards include temperature drift and offset of the characteristic. However, the devices described

Device	Gain Error	Non-Linearity Error	System noise
DAQP-STG (Input module)	± 0.05 % of reading	± 0.02 % of range	$\pm 10 \mu\text{Volt}$
ORION-1624-200 (ADC)	± 0.058 % of reading	± 0.005 % of range	-

Table B.1: Accuracy of data acquisition and conversion devices, from [92], [93]

above are specified for an operating range of 0 - 50 degrees Celsius, which is generally not exceeded at the aeroelastic test rig, while the offset error can be effectively neutralized via measurement of a short-circuited channel and frequent zeroing.

B.4 Prandtl Tube

The pitot-static tube or "Prandtl Tube" is one of the most commonly used technologies in flow measurement, see figure B.1. Based on the familiar principles of Bernoulli, this device measures both static and total pressure of an airstream. By connecting the probe to a suitable differential pressure sensor, it is then possible to obtain the dynamic pressure q and so compute the freestream velocity.

Uncertainty with regard to Prandtl probe measurements is introduced at various points in the measurement chain, beginning at the probe tip itself, which must be turned exactly into the flow to guarantee accurate measurement of the stagnation pressure. For a flow angle of $\pm 10^\circ$, which should easily be achievable even by manual installation, the manufacturer specifies a probe accuracy that is better than $\pm 1\%$ [95].

Then there is the differential pressure sensor that is used to record the

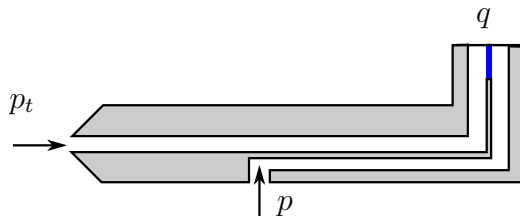


Figure B.1: Schematic of a pitot-static-tube, showing interior probe structure as well as stagnation pressure p_t , static pressure p and dynamic pressure q .

dynamic pressure, which of course is also associated with a certain amount of uncertainty. For the pressure ranges that are relevant here, the manufacturer of the KAL-84 calibration and differential measuring system gives an accuracy of $\pm 0.2\%$ [96].

After the differential measuring system, the next step in the measurement chain for the Prandtl probe is the conditioning and digitization of the dynamic pressure signal via the Dewetron system described in the previous section. With the differential sensor's output range of 0...1 Volt and an assumed reading of 0.3 Volt, the relative errors according to table (B.1) are obtained as 0.12 % for the DAQ input module and 0.07 % for the ADC module. Thus, the relative uncertainty for the dynamic pressure q as measured by the probe can be calculated from equation (B.2) as

$$\sigma_q = \pm 1.03 \%. \quad (\text{B.4})$$

However, in fluid dynamics one is generally not interested in the dynamic pressure q , but rather the flow velocity U . This is related to dynamic pressure and ambient conditions by the expression

$$U = \sqrt{2q \cdot \frac{R_{spec} \cdot T_{t,amb}}{p_{t,amb}}}, \quad (\text{B.5})$$

which is derived from the well-known Bernoulli equation and assumes air to be an ideal gas with gas constant R_{spec} . Hence, the relation of dynamic pressure and velocity is explicitly known, and it is possible to calculate the uncertainty of U using sensitivity coefficients according to equation (B.3). Assuming ambient conditions to be $T_{t,amb} = 293\text{K}$ and $p_{t,amb} = 1.013 \cdot 10^5 \text{ Pa}$ and the values for relative uncertainty given in the sections on the Setra 270 pressure sensor and the Pt100 thermometer, the uncertainty for measuring freestream velocity via Prandtl probe is given as

$$\sigma_U = \sqrt{\left(\frac{\partial U}{\partial q} \cdot \sigma_q\right)^2 + \left(\frac{\partial U}{\partial T_{t,amb}} \cdot \sigma_{Pt100}\right)^2 + \left(\frac{\partial U}{\partial p_{t,amb}} \cdot \sigma_{Setra-270}\right)^2} \quad (\text{B.6})$$

With a typical freestream velocity of $U = 30 \text{ m/s}$ inducing a dynamic pressure of

$$q = \frac{1}{2} \frac{p_{t,amb}}{R T_{t,amb}} \cdot U^2, \quad (\text{B.7})$$

equation (B.6) gives an absolute error of $\pm 0.32 \text{ m/s}$, or in relative terms:

$$\sigma_{\Sigma, Prandtl} = \pm 1.07 \%. \quad (\text{B.8})$$

From this, it is clear that a major contribution to measurement error lies in the orientation of the probe tip with respect to the incoming airstream, and greater accuracy might be attained by careful alignment of the probe.

B.5 Hot Wire Anemometry

Errors are introduced into hot wire anemometry in a few ways: Anemometers are usually calibrated using some other device for measuring flow velocity, for example a pressure probe. Any inaccuracy in that device's output will of course carry over to the hot wire's results. Due to its measuring principle, hot wire anemometry is also quite sensitive to flow properties that can influence the wire's heat balance, like flow temperature or pressure [69]. Finally, the uncertainty inherent to the anemometer itself as well as the I/O-device used to convert the analog to a digital signal must be accounted for.

B.5.1 Calibration

In hot wire anemometry, what is ultimately of interest is the relationship of the anemometer's bridge voltage V_B to the freestream velocity U . To obtain the function $U = f(V_B)$ with any certainty, the system must be calibrated against other measuring instruments, which will introduce additional uncertainty dependent on the components of the measuring chain used for calibration. In the present case, the anemometer was calibrated by placing it in the measuring section of the test rig, together with the Prandtl probe described in the previous section. Probe velocity readings and anemometer bridge voltage were then recorded simultaneously to establish the dependency of voltage on velocity.

Since the anemometer is calibrated with the probe reading as a reference in this way, the accuracy of the Prandtl probe must be taken into account as an influence parameter when estimating measurement uncertainty for hot wire observations:

$$\sigma_{cal,HW} = \pm 1.07\% \quad (\text{B.9})$$

B.5.2 Curve Fitting

The calibration process described above should generally result in a clearly defined calibration function, establishing a precise relationship between bridge voltage and freestream velocity. The actual output however will be a series of data points, from which the calibration function can be approximated by non-linear regression. Here, a least squares method using a third order polynomial was used, the quality of which can be expressed using the adjusted coefficient of determination R_{adj}^2 [97]. In the case of the calibration curve under consideration here, this error was estimated to be

$$\sigma_{lin} = R_{adj}^2 = \pm 0.5\%. \quad (\text{B.10})$$

Note that the value given here is an estimate specific to the third-order fitting procedure used in calibrating the hot wire anemometer as described in

Ref. [98]. For pressure transducers, this error is more accurately given as a 'non-linearity'-value typically found in data sheets or calibration certificates.

B.5.3 Ambient Temperature

Since hot-wire anemometry is a temperature-based method, a major factor contributing to measurement uncertainty is the ambient temperature at which measurements are carried out. When this differs from the temperature at which the anemometer was calibrated, the temperature ratio and thus the heat transfer between wire and fluid is altered. Thus, at higher temperatures the anemometer will report a velocity that is too low, while at lower temperatures the reverse effect occurs. This effect can be described by an equation in the form of

$$V_B = V_{B,raw} \cdot \sqrt{\frac{T_w - T_{t,cal}}{T_w - T_{t,amb}}} \quad (\text{B.11})$$

In which V_B is the bridge signal, T_w is the wire temperature, $T_{t,cal}$ the ambient temperature at which calibration was performed and $T_{t,amb}$ the ambient temperature at time of measurement. Apart from the direct effect that a varying ambient temperature has on heat conduction, there is another, indirect effect: Since the quantity measured by the anemometer is in fact the stream density ρU and the density of a fluid is directly related to its temperature, a variation in ambient temperature introduces additional uncertainty via its influence on density. According to [68], this uncertainty can be calculated by the simple relation

$$\sigma_{\rho,T} = \frac{\Delta T_{t,amb}}{273 \text{ K}} \quad (\text{B.12})$$

Due to its sensitive nature, a hot wire anemometer should be calibrated frequently, and large deviations in temperature compared to calibration conditions are generally not to be expected. However, to arrive at a conservative estimate for accuracy, it seems prudent to include an estimate for a deviation of $\Delta T_{t,amb} = 2 \text{ Kelvin}$, thus obtaining the error associated with ambient temperature fluctuations as

$$\sigma_{\rho,T} = \pm 0.7\% \quad (\text{B.13})$$

B.5.4 Ambient Pressure and Humidity

The density of a fluid (and thus the stream function ρU) is influenced not only by temperature, but also by variations in ambient pressure. The uncertainty introduced by an ambient pressure that deviates from the conditions at calibration is obtained from the following ratio:

$$\sigma_{\rho,p} = \frac{\Delta p_{t,amb}}{\Delta p_{t,amb} + p_{t,amb}} \quad (\text{B.14})$$

A much smaller factor in the overall uncertainty is the contribution of humidity variation, which is usually quantified in terms of water vapour pressure. Assuming standard atmospheric conditions, there will be a differential of $\partial U/\partial p_{wv} \approx 0.01 c$ for each kPa of change in water vapour (wv) pressure:

$$\sigma_{wv} = \frac{1}{U} \cdot \frac{\partial U}{\partial p_{wv}} \cdot \Delta p_{wv} \quad (\text{B.15})$$

Assuming a deviation of 1 kPa for both ambient pressure and water vapour pressure, the associated errors are estimated as:

$$\sigma_{\rho,p} = \pm 0.98 \% \quad (\text{B.16})$$

$$\sigma_{wv} = \pm 0.01 \% \quad (\text{B.17})$$

B.5.5 Anemometer Accuracy and Signal Conversion

The TSI-IFA 300 anemometer in use at the aeroelastic test rig is an integrated measurement system that includes a signal conditioning unit. As with any signal conditioning component, this unit contributes some uncertainty due to offset and gain errors. According to the manufacturer, the relative measurement uncertainty of the anemometer is [99]:

$$\sigma_{sys} = \pm 0.3 \% \quad (\text{B.18})$$

In order to process and store the anemometer's data on a computer, it is digitized by means of a NI PCI-6229 device. The accuracy of this analogue-to-digital-conversion is a function of input range and reading, as well as other factors. For the configuration at the aeroelastic test rig, there is a gain error of 160 ppm, an offset error of 156 ppm, and the noise is estimated at $36.6 \mu\text{V}$ [100].

For a full scale reading of 5 V, the absolute accuracy is thus estimated at $1616 \mu\text{V}$, and the relative accuracy at

$$\sigma_{HW,A/D} = \pm 0.03 \% \quad (\text{B.19})$$

B.5.6 Combined Accuracy

Having established all relevant influence parameters that introduce inaccuracies into the hot wire anemometer's measuring chain, the combined standard uncertainty of this system can now be estimated according to equation (B.2):

$$\sigma_{\Sigma,HW} = \pm 1.73 \% \quad (\text{B.20})$$

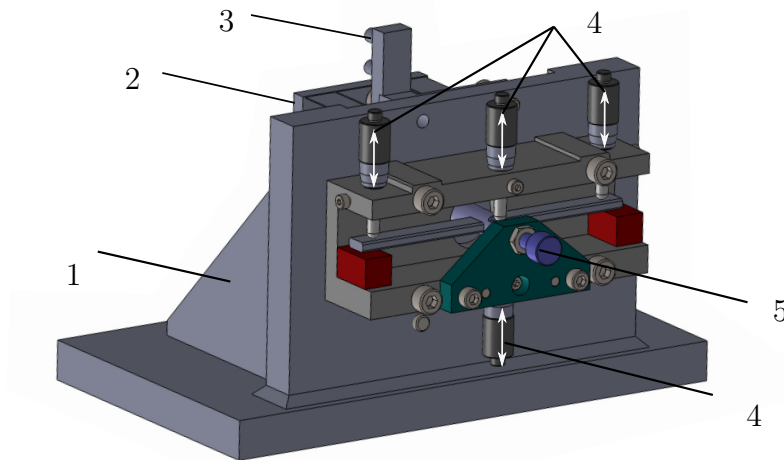


Figure B.2: Computer-aided design scheme of the modified calibration device; (1) mounting support; (2) blade suspension; (3) Lemo connector to data acquisition system; (4) micrometer screws; (5) center of rotation for calibration of the torsional springs.

B.6 Strain Gauge

For the strain gauge calibration, a device was designed that enables the application of a defined deformation so that the relationship of displacement u and voltage output V can be established in the form of a function $V = f(u)$, see figure B.2. The device consists of a support for the blade mounting, milling parts holding four micrometer - two for each degree of freedom - and an arm that can be displaced by the screws. The blade mounting allows two degrees of freedom, namely pitching and plunging. In this work only blades oscillating in pitching motion have been investigated. However the calibration for both degrees of freedom are presented in the following section for completeness.

B.6.1 Calibration - Plunging mode

An illustration of the method of calibration for measuring the blades' plunging motion can be found in figure B.3: By turning the precision screw (1), a defined displacement u is applied at the blade edge (2), resulting in a deformation of the bending spring (3) with its applied strain gauge (4). Assuming that the deformation of the blade edge is negligible due to its relatively high stiffness, the displacement u can be said to equal the vertical displacement of the bending spring. The spring will thus lengthen by an amount Δl that is a function of the applied displacement u , which will affect the resistance of the strain gauge and so the voltage measured. More precisely, the change in

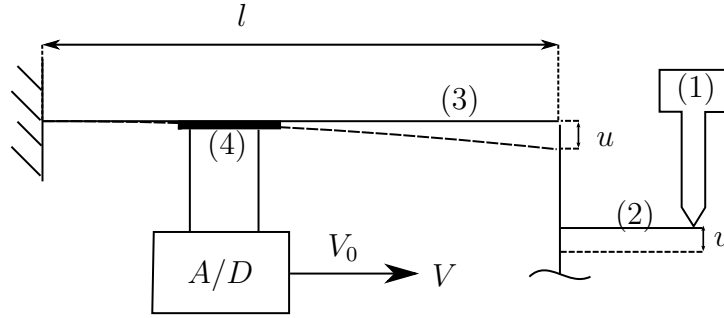


Figure B.3: Schematic sketch of calibration device for plunge mode

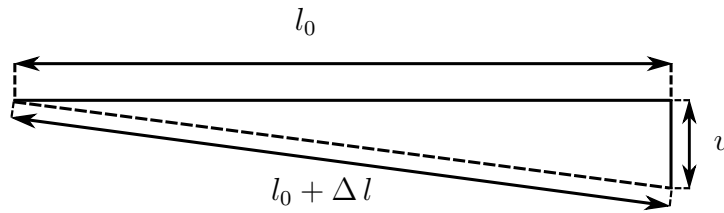


Figure B.4: Illustration of the trigonometric relationships used in calibrating the strain gauge.

resistance can be expressed as

$$\frac{\Delta R}{R_0} = F \cdot \frac{\Delta l}{l_0} = F \cdot \varepsilon, \quad (\text{B.21})$$

where F is a calibration factor that is generally provided by a strain gauge's manufacturer. Applying some trigonometric relationships to the sketch in figure B.4, it is clear that the strain can be given as

$$\varepsilon = \frac{\sqrt{l_0^2 + u^2}}{l_0} - 1 \quad (\text{B.22})$$

and by relating voltage and pressure linearly through

$$V = V_0 \cdot \frac{\Delta R}{R_0} \quad (\text{B.23})$$

the function relating voltage and displacement is obtained as

$$V = V_0 \cdot F \cdot \left(\frac{\sqrt{l_0^2 + u^2}}{l_0} - 1 \right) \quad (\text{B.24})$$

Using this function and its partial derivatives, the influence of various parameters on the measurements carried out by strain gauge can be calculated.

input quantity x_i	Value and uncertainty	$\partial U/\partial x_i$
Voltage, $x_i = V_0$	2.5 ± 0.0289 Voltage	$F \cdot \left(\frac{\sqrt{l_0^2 + u^2}}{l_0} - 1 \right)$
Calibration factor, $x_i = F$	2 ± 0.02	$V_0 \cdot \left(\frac{\sqrt{l_0^2 + u^2}}{l_0} - 1 \right)$
length measurement, $x_i = l_0$	65.1 ± 0.01635 mm	$-F \cdot V_0 \cdot \frac{u^2}{l_0^2 \cdot \sqrt{l_0^2 + u^2}}$
Displacement, $x_i = u$	3 ± 0.01 mm	$F \cdot V_0 \cdot \frac{u}{l_0^2 \cdot \sqrt{l_0^2 + u^2}}$

Table B.2: Influence parameters and sensitivity coefficients for calibration of strain gauges' plunge mode

The main parameters that are relevant for recording the plunging mode of the cascade are bridge voltage and the inherent calibration factor F that relates the gauge's strain and resistance. The length of the bending spring on which the gauge is affixed and the nominal displacement that is applied via precision screw must also be considered.

From the values and partial derivatives collected in the table above, an estimate for the uncertainty associated with calibrating the strain gauges for plunge mode can be computed from (B.3) as

$$\sigma_{cali, Plunge} = \pm 1.67 \% \tag{B.25}$$

B.6.2 Pitching Mode

The calibration process for the pitch displacement is quite similar to the one described above for the plunging mode, but some modifications have to be introduced. The device sketched in figure B.2 is only capable of applying a linear displacement, but for experiments dealing with a blade pitching motion an angular displacement β is required. This is achieved by modifying the device so that two precision screws are placed at some distance from the blades axis, rotating the lever arm around half chord. As illustrated in figure B.5, this angle is obtained by basic geometric operations as a function of the displacement u applied at the outer adjustment screws and the distance between the screws and the suspension axis d :

$$\beta = \arcsin(u/d) \tag{B.26}$$

Since the pitch displacement calibration is performed using the same device with a few modifications, most influence parameters and uncertainties carry over from the 'plunge' case. There is some additional uncertainty as a result of measuring the distance d , which will again require a combined Type A/B

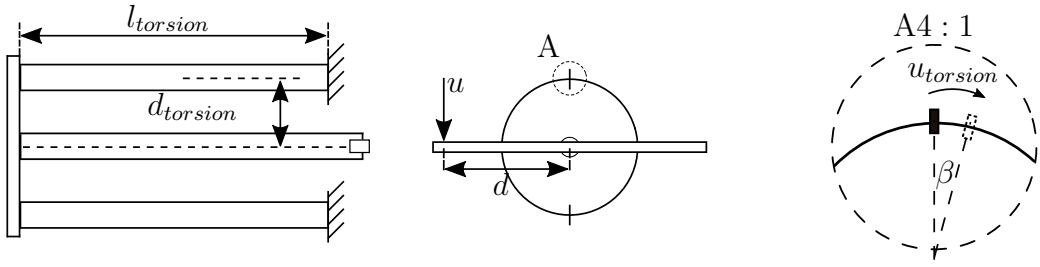


Figure B.5: Illustration of the geometric relations for calibrating the strain gauge's pitch mode

input quantity x_i	Value and uncertainty	$\partial u_{torsion}/\partial x_i$
Lever arm, $x_i = d$	66.1 ± 0.01635 mm	$-\frac{d_{torsion} \cdot u}{h^2 \cdot \sqrt{1 - (u/h)^2}}$
Distance spring - axis of rotation, $x_i = d_{torsion}$	6.51 ± 0.00164 mm	$\arcsin(u/h)$
Displacement, $x_i = u$	3 ± 0.01 mm	$\frac{d_{torsion} \cdot u}{h \cdot \sqrt{1 - (u/h)^2}}$

Table B.3: Additional uncertainty influences for pitch displacement calibration

analysis.

As figure B.5 also shows, the displacement of the torsion spring $u_{torsion}$ cannot be set directly, but has to be calculated from the angle of twist and the lever arm d :

$$u_{torsion} = d_{torsion} \cdot \beta = d_{torsion} \cdot \arcsin(u/d) \quad (\text{B.27})$$

The uncertainty in determining the torsional displacement $u_{torsion}$ is thus determined from equation (B.3) as $\sigma_{ut} = 9.8867 \cdot 10^{-4}$ mm or about 0.03 percent in relative terms. All other influence parameters remain the same as in the plunge case, and so the error in this case can be obtained from a simple calculation of error propagation according to equation (B.2):

$$\sigma_{cali, Pitch} = \pm 1.67\% \quad (\text{B.28})$$

The additional uncertainty from measuring the torsional displacement is thus seen to be mostly irrelevant to the calibration accuracy, changing the combined uncertainty only in the 6th decimal place, while the main influence parameters of excitation voltage and gauge factor remain the same.

Error source	Calibration	Hysteresis	DAQ	ADC
Relative Error	$\pm 1.67 \%$	$\pm 0.05 \%$	$\pm 0.27 \%$	$\pm 0.063 \%$

Table B.4: Relative uncertainties influencing DMS measurements.

B.6.3 Strain Gauge - other influences

Having estimated the possible error introduced into strain gauge measurements through calibration, one still has to account for various other influences along the measurement chain. These include the gauge's hysteresis as well as the data acquisition and digitization.

While the first two of these quantities can be taken directly from manufacturer specifications[101], the estimation of signal conditioning and conversion error requires some consideration. The gauges are configured in a full bridge, with a sensitivity of around 2mV/V [102] and an excitation voltage of 2.5 V . A full scale reading is therefore computed as

$$2.5\text{ V} \cdot 2\text{ mV/V} = 5\text{ mV}. \quad (\text{B.29})$$

Thus, the relative accuracy for the strain gauges utilized at the aeroelastic test rig is estimated from equation (B.2) as

$$\sigma_{\Sigma, DMS} = \pm 1.69 \%. \quad (\text{B.30})$$

B.7 Pt100-Thermometer

At the aeroelastic test rig, temperature in the settling chamber is recorded by a Pt100-Thermometer. Such devices utilise the temperature dependency of the electrical resistance of metals like platinum to deliver precise temperature measurements. The exact relationship between resistance and temperature in these devices is specified in a widely accepted industry standard that also defines various accuracy categories. The device in use here is a class A resistance thermometer, which exhibits a limit variation of $\pm(0.15 + 0.002 \cdot t)$ degrees Celsius, where t is the absolute Value of the temperature being recorded [103].

Temperatures in the tunnel's settling chamber have reached up to 40 degrees Celsius, while a more typical value might be more on the order of 25 degrees. Since the deviation is a linear function of temperature, using the higher value should therefore yield a conservative estimate. The absolute variation according to DIN EN 60751 is then given as

$$\pm(0.15 + 0.002 \cdot 40)^{\circ}\text{C} = 0.23^{\circ}\text{C}, \quad (\text{B.31})$$

so a conservative estimate for the relative uncertainty associated with Pt-100 measurements at the aeroelastic test rig is obtained as

$$\sigma_{\Sigma, Pt100} = \pm \frac{0.23}{40} = \pm 0.58 \%. \quad (\text{B.32})$$

B.8 Pressure Sensors Endevco 8510-B-1

One of the main flow features under investigation at the aeroelastic test rig is the pressure distribution around an oscillating airfoil forming part of a cascade. To enable the measurement of this highly unsteady phenomenon, the central three blades of the cascade feature a total of 20 pressure taps per blade, spaced exponentially along a line that forms an angle of 15 degrees with the blade chord. Each of these is connected via flexible tubing of a specified length to its respective transducer, thus making it possible to obtain precise pressure information along both the pressure and suction surface of the blade.

When conducting a measurement with a pressure transducer, three main sources of uncertainty that are inherent to the device's functional principles must be taken into account: The first of these is the linearity or curve-fitting error. This occurs due to the discrepancy between the line that is fitted to the sensor's calibration points and the device's true response curve, which must not necessarily be linear. The other two error sources for pressure transducers are called non-repeatability or repeatability error and pressure hysteresis. These define the sensor's ability to reproduce its output when it is cycled through its operating range, and due to their similar nature are often lumped together in specifications [104].

According to manufacturer information, a typical value for the linearity error of the transducers connected to the blade pressure taps is around $\pm 1\%$, while the repeatability and hysteresis errors can be expected to be $\pm 0.2\%$ each, see table B.5. From this, the manufacturer gives an estimate for the combined maximum error of $\pm 1.5\%$ [105]. This, however is an estimate for the worst case error. Since it is unlikely that all errors will be in the same direction, there should be at least some cancellation, and a more probable figure can be obtained via the familiar root-square-sum formula (B.2).

As most other measurement signals at the aeroelastic test rig, the output of the endevco sensors is fed through a digital data acquisition system, which accounts for some additional uncertainty. An estimate for the error of feeding a full scale reading of 300 mV into this device is given in the table above, together with the error sources inherent to the sensor. From these

Error Source	Non-linearity	Hysteresis	Repeatability	DAQ	ADC
Relative Error	$\pm 1\%$	$\pm 0.2\%$	$\pm 0.2\%$	$\pm 0.07\%$	$\pm 0.06\%$

Table B.5: Relative uncertainties for unsteady pressure measurements.

values, the total relative uncertainty is obtained as

$$\sigma_{\Sigma,endecco} = \pm 1.04\% \quad (\text{B.33})$$

Finally, it must be taken into account that the endecco transducers are calibrated against various other devices depending on the pressure range of interest. While the endecco 8510B -1 features a range of 0-1 psig, i.e. approximately 0-6895 Pa, at the aeroelastic test rig it is usually calibrated for pressure ranges of 0-25 or 0-100 Pa against the Setra-264 device, while for the 0-1000 Pa range the KAL-84 pressure calibrator is used. It is therefore necessary to state two different values for the uncertainty of measurements performed using the endecco transducers.

Incorporating the error introduced by calibration is done via the usual Root-Square-Sum formula for error propagation, according to which we obtain a value of

$$\sigma_{\Sigma,endecco/SETRA} = \pm 1.45\% \quad (\text{B.34})$$

when calibrating against the Setra-264 transducer. A calibration against the KAL will deliver a slightly higher precision of

$$\sigma_{\Sigma,endecco/KAL} = \pm 1.06\%, \quad (\text{B.35})$$

which is needed due to much wider calibration range of 1 kPa.

B.9 Setra 264

The aeroelastic test rig is equipped with a Setra Model 264 that is used to measure freestream static pressure. This very low differential pressure transducer is available in a variety of versions that differ with respect to their performance and accuracy. For the model 264 - F that is installed here, the manufacturer claims a non-linearity of $\pm 0.22\%$ of the full-scale reading and an hysteresis of $\pm 0.1\%$ [106].

However, since these values depend on a calibration provided by the manufacturer and certified to a high standard of precision that tends to degenerate over time, it seems more prudent to work with the values for a standard model 264-C:

Error Source	Non-linearity	Hysteresis	Repeatability	ADC
Relative Error	$\pm 0.96 \%$	$\pm 0.1 \%$	$\pm 0.26 \%$	0.065 %

Table B.6: Relative errors for Setra 264 sensor.

Thus, according to (B.2), an estimate for the error associated with static pressure measurements in the freestream is given as

$$\sigma_{\Sigma, \text{Setra-264}} = \pm 1 \%. \quad (\text{B.36})$$

For the calculation a reading of 3.5 Volt and Output of 5 Volt are assumed. Additional high-precision calibrations were performed, with the model Setra 264, for the ranges of 0-25 and 0-100 Pa. These certificates guarantee a non-linearity error of $\pm 0.206\%$ for the 0-100 Pa range and $\pm 0.25\%$ for the range of 0-25 Pa [106]. Thus, $\sigma_{\Sigma, \text{Setra-264}}$ can be considered as a conservative estimation of the uncertainty.

B.10 Setra 270

The absolute pressure in the settling chamber was acquired with a Setra Model 270. A high degree of accuracy of $\pm 0.05 \%$ FS can be achieved [107]. The error sources for this device are the same as in any other pressure transducer, and are listed in the table B.7. A conservative estimate for the uncertainty of the Model 270's reading according to (B.2) can therefore be calculated as

$$\sigma_{\Sigma, \text{Setra-270}} = \pm 0.08 \%, \quad (\text{B.37})$$

assuming a reading of 4 Volt and a output range of 5 Volt.

Error Source	Non-linearity	Hysteresis	Repeatability	ADC
Relative Error	$\pm 0.05 \%$	$< 0.01 \%$	$< 0.01 \%$	0.064 %

Table B.7: Relative errors for Setra 270 sensor.